Shape Effects of Additives on Properties of Bilayer Membranes

Hatsuho Usuda

February 2020

Shape Effects of Additives on Properties
of Bilayer Membranes

Hatsuho Usuda

Doctoral Program in Nano-Science and Nano-Technology

Submitted to the Graduate School of

Pure and Applied Sciences

in Partial Fulfillment of the Requirements

for the Degree of Doctor of Philosophy in

Science

at the

University of Tsukuba

Contents

Chapter 1

General Introduction

1.1   Lipid Membrane Properties

A bilayer membrane is an assembly of amphiphiles that have nearly cylindrical shapes, such as phospholipids. There are only two molecules in the direction normal to the membrane surface, but, on the membrane surface, there are a large number of molecules aligned, as shown in Fig. 1.1. These characteristics bring to lipid membranes unique properties such as phase transitions within the surface and the high deformability and fluctuations in its normal direction. Although the bilayer membrane is very different from the usual two- or three-dimensional materials, it is quite ubiquitous since it is the main component of biological membranes. Further, bilayer-forming amphiphiles are ingredients of cosmetics, detergents, and a drug carrier that is utilized in drug delivery systems. Research on bilayer systems extends over various fields such as biology, engineering, and medical science. In any case, a bilayer membrane exists as a multicomponent system. It is interesting that bilayer membranes can include molecules with very different shapes and still form two dimensional "crystal," and membrane properties change depending on species and ratio of the included molecules. For this reason, the effects of additives on membrane properties have widely been investigated thus far.

Phase behavior is an important property that characterizes a bilayer membrane. Bilayers can exist as a gel or a liquid-crystalline phase at a given temperature. In the gel phase, the alkyl chains of phospholipids are in mostly "all *trans*" conformation and form a centered rectangular lattice, which is derived from the hexagonal (triangular) lattice by slight distortion. As the temperature rises, gel phase bilayers "melt" at a characteristic temperature to form the liquid-crystalline phase, which is fluidic laterally. The phase transition between the gel and liquid-crystalline phases is called the main transition, the temperature of which is denoted by T_m. In the liquid-crystalline phase, the proportion of the *gauche*-conformation is larger than that in the gel phase, and the in-plane short-range order is
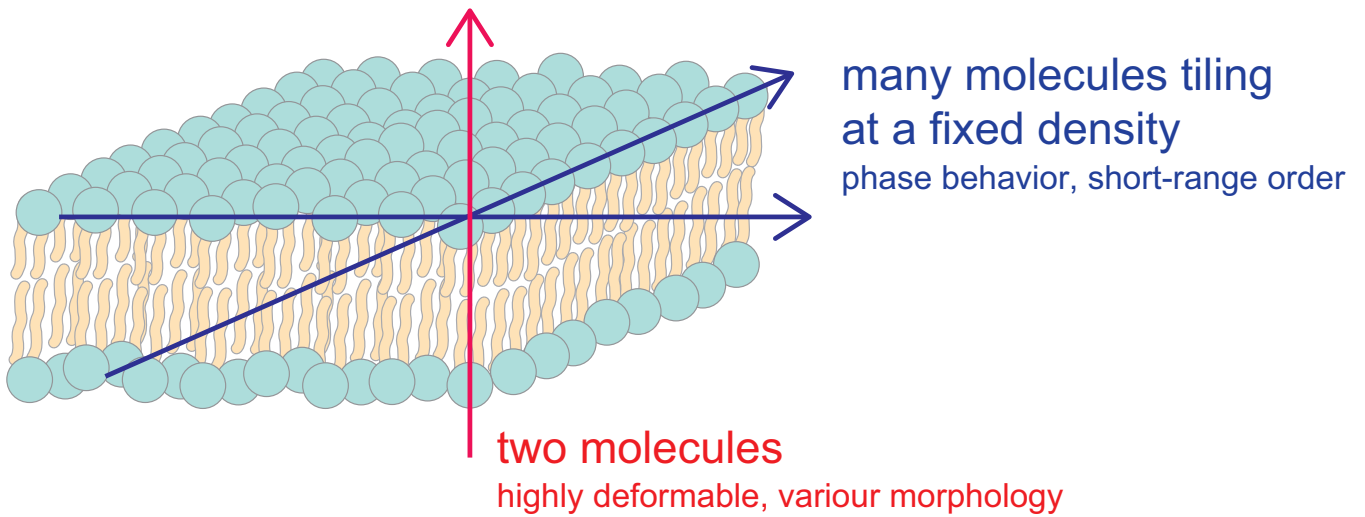
Fig. 1.1. Characteristics of a lipid bilayer membrane
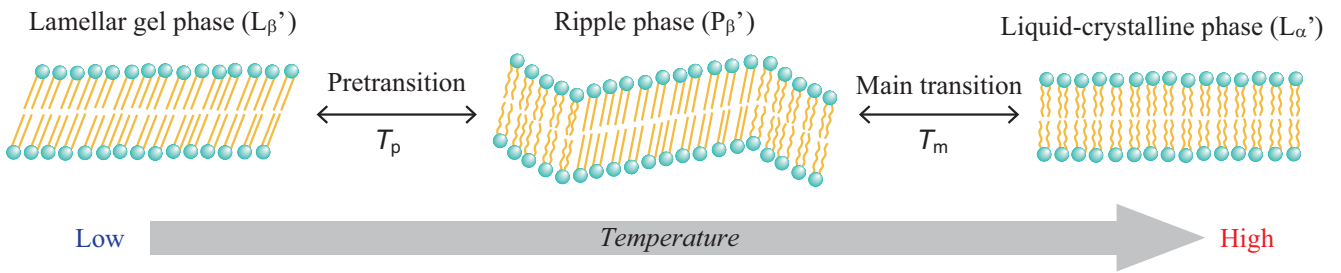
Fig. 1.2. Phase behavior of PC bilayers.
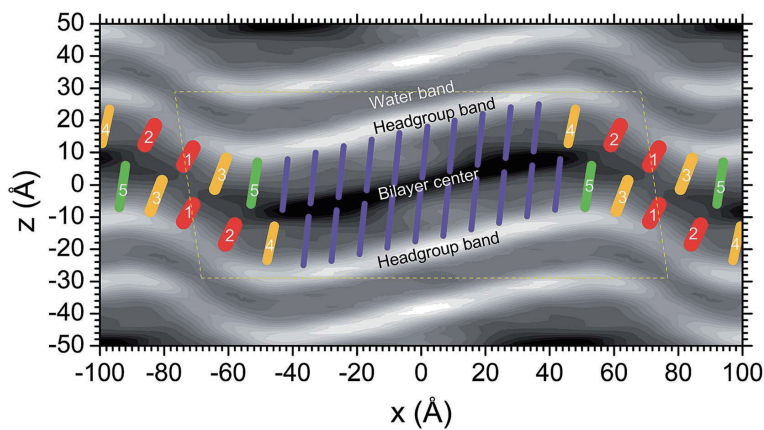
Fig. 1.3. Packing of chains superimposed on the gray scale relative electron density map. Purple: gel-like chains. Red: fluid-like chains. Orange and green: chains with intermediate lengths and packing. The dashed yellow lines show the unit cell [1].

mostly lost.

Phosphocholine (PC) is a typical phospholipid and widely used for membrane studies. PC bilayers undergo a pretransition between two gel phases, a lamellar-gel, and ripple phases. Its transition temperature is denoted by T_p (Fig. 1.2). In the ripple phase, the bilayers have a rippled structure that has two sides with different lengths, as shown in Fig. 1.3 [1].

Transition temperatures, T_m and T_p, of PC bilayers exhibit significant dependences on the length and saturation degree of lipid alkyl chain [2]. As the lipid chains become long, T_m and T_p become higher with larger transition enthalpy. For example, the introduction of unsaturation of *cis* type to the *sn*-2 chains of 18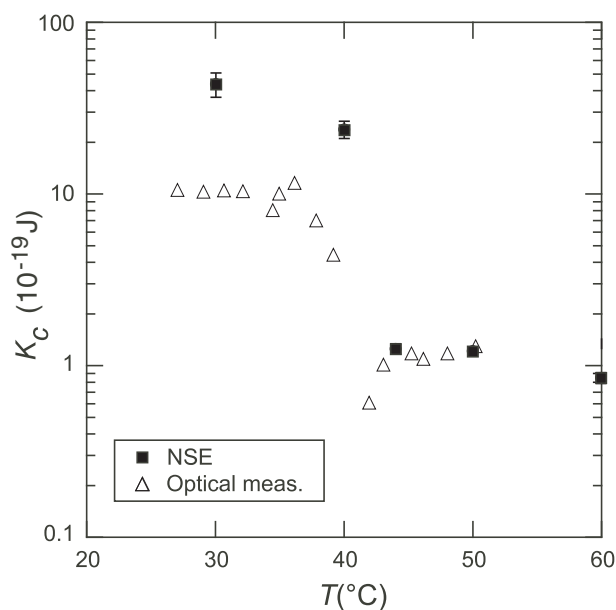-carbon PC lowers T_m by 50 °C. These dependencies have been interpreted in terms of molecular packing. The lipids with long chains are packed densely while short or unsaturated chains prefer loose packing, which results in changes in transition enthalpy ΔH, transition entropy ΔS and transition temperature.

Fig. 1.4. Temperature-dependence of κ of DPPC bilayers [3]. Square: κ obtained in NSE measurements. Triangle: κ obtained in optical measurements [4].

Another crucial property is the bending rigidity of the lipid membrane. A lipid membrane has tesselations of a plane with a fixed density while exhibiting high deformability in the direction normal to the membrane surface. This deformability gives a lipid membrane unique morphology and dynamics determined by the mechanical properties. When a flat bilayer is bent, bending energy is required to extend the outer monolayer and to compress the inner monolayer. If we consider phospholipid membranes as a liquid-crystalline membrane with vanishing thickness, we can apply liquid-crystalline physics on the phospholipid membranes. Helfrich has demonstrated that its area and curvatures [5]

characterize the mechanical state of a membrane. When a small piece of a membrane is bent, the bending elastic energy is expressed as [5],

$$F_c = \frac{\kappa}{2}(c_1 + c_2 - c_0)^2 + \bar{\kappa}c_1c_2 \tag{1.1}$$

where c_1 and c_2 are the principal curvatures and c_0 is the spontaneous curvature of the membrane. κ and $\bar{k}_c$ are the cylindrical and saddle-splay bending modulus, respectively. $\bar{\kappa}$ depends on topological changes of the bilayer. However, the bilayer topology does not change during experiments such as scattering and microscopy observation. Also, $\bar{\kappa}$ is defined as 0 in a surface within the bilayer if the bilayer is fluid and has no long-range interactions [6, 7]. This definition means that the second term of Eq. 1.1 is negligible in certain cases. κ is much larger in the liquid-crystalline phase than in the gel phase, as shown in Fig. 1.4 [3, 4]. Also, it exhibits anomalous behavior around T_m, which is 41 °C in the case of DPPC bilayers. c_0 is assumed to be zero since a vesicle is much larger than constituting phospholipid molecules, and the bilayer is symmetrical in its two sides. Membrane stretching also requires energy. The stretching elastic energy per unit area is expressed as,

$$F_s = \frac{k_s}{2}\left(\frac{\Delta S}{S_0}\right)^2 (\Delta S = S - S_0) \tag{1.2}$$

$$\sigma = S_0 \frac{\partial F_s}{\partial S} = k_s \left(\frac{\Delta S}{S_0}\right) \tag{1.3}$$

where σ is the membrane tension, S_0 is the equilibrium area of the membrane, which is the area at $\sigma = 0$, S is the deformed area of the same membrane, and k_s is the stretching elastic modulus.

Internal membrane dissipation is not included in the early membrane dynamics theory, but its contribution has been pointed out. Inter-monolayer coupling is a kind of internal membrane dissipation. When the two monolayers in a bilayer are fully coupled, the bending energy is required more than that required in the case of decoupled monolayers [8–11]. Membrane viscosity is also taken into account to understand membrane dynamics [12].

These membrane mechanical properties dictate the mesoscale collective dynamics such as bending and thickness fluctuations. The bending fluctuations are undulations, where the curvature of the bilayer continuously changes [5–7]. In the case of a giant unilamellar vesicle, the bending fluctuations are visible using optical microscopy in the liquid-crystalline phase [13]. The thickness fluctuations are an increase and a decrease in thickness around the average thickness [14–17]. Their amplitudes are on the nanometer scale, and their relaxation times are longer than 100 ns. The characteristic time and length scales are determined by thermal energy and solvent viscosity in addition to the membrane
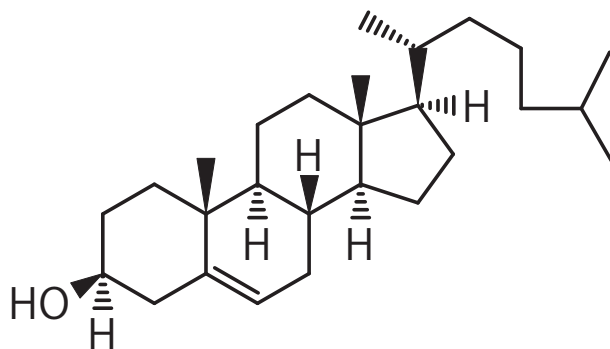
Fig. 1.5. Chemical structure of cholesterol.

mechanical properties. The collective dynamics are crucial for understanding the correlation between microscopic and macroscopic scales. The shape of constituting molecules should be reflected in the collective motions of the bilayers.

1.2 Effects of Small Organic Molecules on Physicochemical Properties of Phospholipid Bilayers

The effects of some small organic molecules on the physicochemical properties of phospholipid bilayers have been investigated using binary or ternary bilayers thus far since phospholipids are the primary components of biological membranes [**?**, 18–27]. The effects of cholesterol (Fig. 1.5) have been intensively investigated on the assumption of crucial roles of cholesterol in lipid microdomains termed "lipid raft" [28]. Adding cholesterol into phospholipid bilayers causes significant changes in physicochemical properties in the gel and the liquid-crystalline phases in the opposed manners, which is called biphasic effects: cholesterol perturbs the structural order of the alkyl chains in the gel phase whereas it enhances the orders in the liquid-crystalline phase [21, 29–31]. That is, the degree of the molecular orders in these phases become similar. With increasing cholesterol content, T_{m} decreases as shown in Fig. 1.6 [18,19,23]. The bilayer in the gel phase becomes flexible due to the perturbation with increasing the cholesterol content. A transition to another phase (the liquid-ordered phase) happens in some cases [32].

The effects of cholesterol have been reported opposite to the cases for *n*-alkanes. Although *n*-alkanes do not exist in biological membranes, the effects of *n*-alkanes on lipid membranes have been studied for more than 30 years because of their anesthetic properties as well as their use in black lipid membranes [33–37]. In contrast to cholesterol, it has been revealed that long *n*-alkanes enhance the structural order in phospholipid membranes in the gel phase [25, 33]. That is, long *n*-alkanes widen

Fig. 1.6. Phase diagram of DPPC/cholesterol bilayers [18]. L_c: the crystal phase of the pure DPPC bilayer. L'_β: the gel phase of the pure DPPC bilayer. $L'_{o\beta}$: liuid-ordered phase of the DPPC/cholesterol bilayer, which is close to the gel phase. $L'_{o\alpha}$: liquid-oredered phase of the DPPC/cholesterol bilayer, which is like liquid-crystalline phase like. P'_β: the ripple phase of the pure DPPC bilayer. L_α: the liquid-crystalline phase of the pure DPPC bilayer.

the gap of the structural order between the two phases. T_m becomes higher when long n-alkanes are added to PC lipid bilayers as a result of the enhanced order in the gel phase [25]. With decreasing the chain length of n-alkanes, T_m becomes even lower than that of the pure lipid bilayer. However, this is not a discontinuous change in the incorporation effect of n-alkanes. The depression of T_m by short n-alkane addition is the result of continuous changes in enthalpy and entropy of the system depending on the chain length [25]. The contrary effects of cholesterol and n-alkanes suggest that the effect of the incorporation depends on the shape of incorporated molecules.

1.3 Molecular Shape Dependence of Physicochemical Properties

A bilayer membrane is one of soft matter, whose physicochemical properties of materials are significantly affected by the shape of a constituting molecule. Indeed, some correlations have been reported between molecular shape and material properties, although it is difficult to predict macroscopic properties from microscopic molecular structure. The molecular shape dependence of physicochemical properties is often observed in soft matter systems such as polymers, liquid crystals, and colloids.

In colloid forming systems, assemblies of amphiphiles such as surfactants and lipids are described by a molecular shape expressed as a packing parameter (CPP) of a constituting molecule as shown in Fig. 1.7 [38]. CPP is a dimensionless parameter defined as $v/a_0 l_c$ where v is the volume of hydrocarbons, a_0 is the optimal area of a hydrophilic group, and l_c is the critical chain length. When the CPP of a molecule is smaller than 1/3, molecules are expressed as cone-shaped and form spherical micelles. Indeed, micelle formation has been reported for various ionic surfac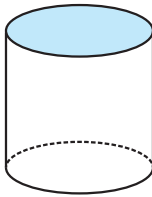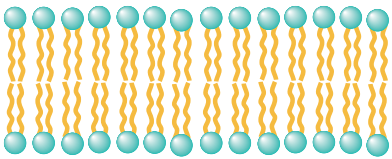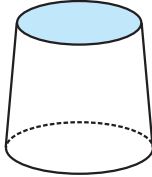tants that have a large hydrophilic group and a hydrocarbon chain. In the case of molecules with a somewhat smaller hydrophilic group such as lysolipids, CPP increases to be $1/3 \sim 1/2$, resulting in the truncated cone. Such molecules do not fit in spherical micelles and form cylindrical micelles. Amphiphiles with a large hydrophilic group and two hydrocarbons have CPP in the range of $1/2 < \text{CPP} < 1$, and form flexible bilayers or vesicles. If the molecules are cylindrical like phosphatidylethanolamine (PE) with $\text{CPP} \approx 1$, they form planar bilayers. Finally, when CPP is larger than 1, which means that a molecule has a very small hydrophilic group, inverted micelles result.

The emergence of a thermotropic liquid crystal is explained from molecular anisotropy represented by calamitic and discotic shapes. Due to the excluded volume effect of anisotropic molecules, a liquid-crystalline system has long-range orientational order and exhibits an intermediate state between crystal and liquid [39]. An additional property of a liquid crystal can be induced by changing

packing parameter $v/a_0 l_c$	packing shape	structure formed
<1/3	cone a_0 v l_c	spherical micelles
1/3~1/2	truncated cone	cylindrical micelles
1/2~1	truncated cone	flexible bilayers vesicles
~1	cylinder	palanar bilayers
>1	inverted truncated cone	inverted micelles
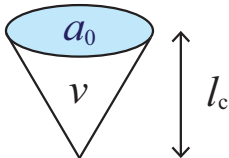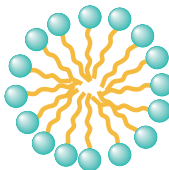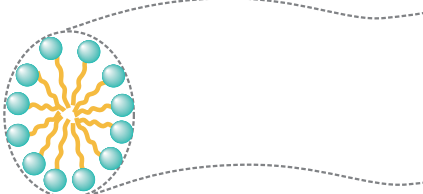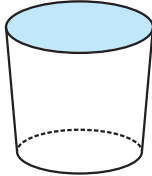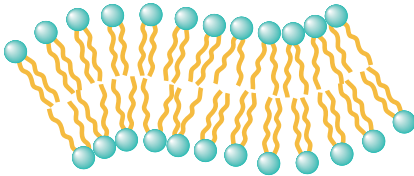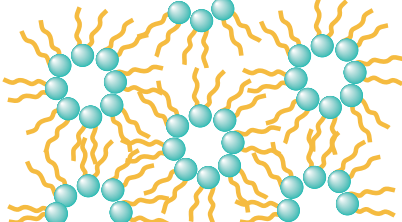
Fig. 1.7. Molecular shape and a packing parameter of small amphiphilic molecules and the structure formed [38].

the molecular shape of the components. For example, banana-shaped achiral molecules form ferro-electric smectic liquid crystals despite their C_{2v} symmetry [40]. Liquid-crystalline molecules usually have alkyl chains in addition to rigid aromatic cores. An alkyl chain in a molecule plays roles for liquid crystal formation as an entropy reservoir and an intramolecular solvent [41–43]. The alkyl chain length determines favorable phases. In the case of a homologous series, a short chain stabilizes a nematic phase, whereas a long chain often induces a smectic phase.

Physical properties of polymer melts also depend on the structure of molecules in the system. Commonly, polymer melts have higher viscosity when the lengths of molecules are longer. Also, when the polymerized chain is branched, the system exhibits higher viscosity. Diblock copolymers form characteristic phases depending on the volume fraction of the two blocks.

As mentioned above, the macroscopic physicochemical properties are affected by the shapes and structural features of the component molecules. Clarifying the correlations has been impressive as basic science and useful for molecular designs for industrial use. Polymers, liquid crystals, and amphiphile solutions are widely used in commercial products.

The physicochemical properties of the binary system are also expected to exhibit dependency on the shapes of constituting molecules. In the binary systems of 4-*n*-alkyl-4'-cyanobiphenyls (*n*CBs) having chains with different lengths, the phase behaviors are characterized by the average length of the chains of composing *n*CBs [44–46]. The phase behavior of the binary mixture becomes practically the same as that of *n*CB, where the chain length is the same as the average length of the system. It has been reported that the addition of *n*-alkanes induce apparent elongation of the alkyl chain in liquid crystalline molecules [47,48]. Furthermore, the odd-even effect was observed depending on the carbon number in the alkyl chain of minor *n*CB [46]. The results suggest that the minor component can change the physicochemical properties of the whole system, depending on their shapes.

1.4   Purpose of This Study

Although there is a large number of studies on additive effects in lipid bilayer systems, systematic understandings from the viewpoint of molecular shape are scarce, and most of the knowledge is on biological or pharmaceutical molecules since a lipid bilayer is a basic component of a biological membrane. The contrary effects of cholesterol and *n*-alkanes indicate that the effect of the incorporation strongly depends on the shape of incorporated molecules. It seems likely that a bulky molecule perturbs the molecular order more largely. Indeed, *cis*-stilbene perturbs the molecular order more significantly than the *trans*-isomer because of its bulkier structure, resulting in a decrease of T_m [49].

Also, hormones and cholesterol derivatives lower T_m [50, 51]. On the other hand, a linear alkyl chain enhances the molecular order, likely because it fits into a gap [52] in the hydrophobic region of the lipid bilayers and stabilizes the gel phase [25]. Since *n*-alcohols and *trans* fatty acid show the similar effects on the phase behavior [36, 53, 54], it is expected that a molecule mainly composed of a linear alkyl chain exerts a similar effect on the physical properties of the lipid bilayers. The contrasting effects of bulky shaped molecules and straight chainlike molecules, and similar effects observed among straight chainlike molecules imply that the incorporation effects strongly depend on the structural feature of the additives.

In this study, the author investigates the molecular shape dependence of incorporation effects on the properties of lipid membranes. Further exploration of molecular shape dependence of material properties will yield a systematic understanding of the correlation between microscopic and macroscopic scales. We employ additives whose shapes are chainlike and additives having both a core and a chain. Straight chainlike molecules can be regarded as similar additives because they incorporate into the hydrophobic region of a lipid bilayer, where alkyl chains align. The effects of molecules with a core and a chain were investigated using a series of liquid-crystalline molecules. The structural feature systematically changes among each series of organic molecules.

After describing experimental techniques in Chapter 2, we describe the effects of straight chainlike molecules in Chapter 3. When we discuss incorporation effects from the viewpoint of molecular shape dependence, the consideration of a chemical difference between additives is necessary since different chemical species may affect differently through chemical interactions such as hydrogen bonding. To estimate the influence due to chemical differences, we investigate the incorporation effects for several kinds of *n*-alkanes derivatives. Nine kinds of compounds with tetradecyl group and another terminal group are added to DPPC bilayers, separately, and microscopic structure and macroscopic phase behavior are investigated. These investigations establish the similar effects of *n*-tetradecane derivatives on the chain packing in the gel phase and the phase behavior of DPPC bilayers.

After clarifying that the *n*-tetradecane derivatives have similar effects on the chain packing in the gel phase and the phase behavior of DPPC bilayers, we choose *n*-alkane as a representative molecule of chainlike molecules. Effects of *n*-alkane on phase behaviors and chain packing in the gel phase of lipid membranes have been studied thus far, but effects on mechanical properties and membrane dynamics remain to be clarified. It is interesting to know incorporation effects on mesoscale dynamics to reveal how microscopic differences affect macroscopic properties. As mesoscale dynamics, we chose the bending and the thickness fluctuations.

Finally, molecules with a core and a chain were incorporated into DPPC bilayers, and their effects

on the microscopic structure and the phase behavior were investigated (Chapter 4). The author used nine additives which has a biphenyl core part and a straight alkyl chain with different length. If the physicochemical properties of the system changed according to the chain length, we would conclude that the effects of a compound are described based on constituting parts such as a bulky structure and a chain length.

Chapter 2

Methods

This chapter describes general principles and instrumental information of experimental techniques utilized in this study. Details such as the conditions of experiments will be explicitly given at relevant parts in the succeeding Chapters.

2.1 Differential Scanning Calorimetry (DSC)

DSC targets the heat flow due to the temperature difference. [55, 56] DSC is suitable to observe phase behavior of substances such as phospholipid membranes since a phase transition accompanies heat flow. In DSC measurement, a temperature difference is measured instead of heat flow since direct measurement of heat is difficult. There are two kinds of DSC, and, in this study, heat flux DSC was employed. A typical setup of heat flux DSC is schematically shown in Fig. 2.1. A sample and a reference pan have a common heater. A thermocouple measures the temperature difference between the reference and the sample sides. In a DSC measurement, the temperature is scanned at a programmed rate and the temperature difference is recorded with the temperature. Upon melting, peak-like signals are observed as shown in Fig. 2.2. At the melting point, the temperature of the sample remains constant until all the sample melt, resulting in a large temperature difference between the sample and the reference. After the completion of the melting, heat rapidly flows into the sample, and the signal returns to the constant level (baseline). The characteristic points around the peak are named as shown in Fig. 2.2.

In this study, DSC measurements were performed using a commercial apparatus (Q200, TA Instruments, New Castle, DE), which is of the heat-flux type. The temperature and the cell constant of the apparatus were calibrated using the melting point and the melting enthalpy of indium. About 5 μL of the suspensions were sealed in aluminum pans. The quantification of the enthalpy change upon
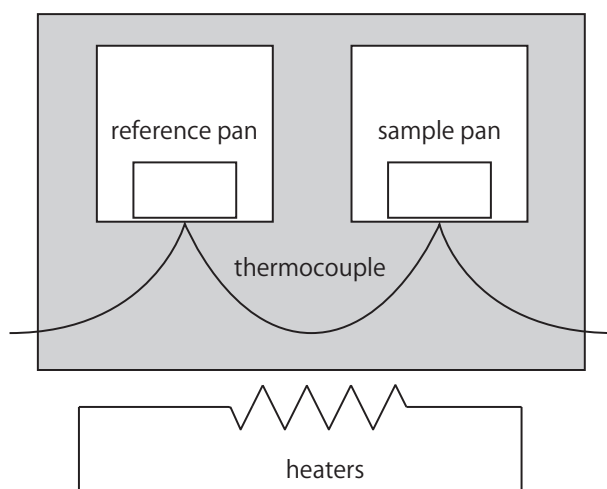
Fig. 2.1. A schematic diagram of heat flux DSC.
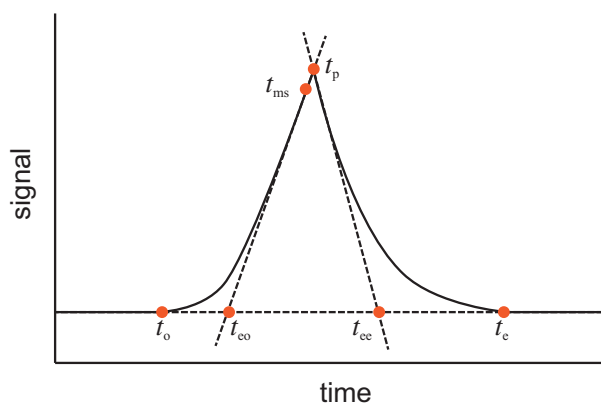
Fig. 2.2. A schematic diagram of DSC signal observed upon a first-order phase transition. t_o: onset time. t_{eo}: extrapolated onset time. t_p: peak time. t_{ms}: the time at which the maximum of slope is observed. t_{ee}: extrapolated ending time. t_e: ending time.
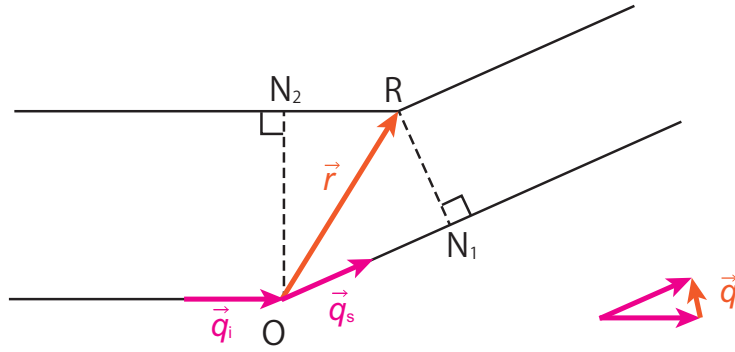
Fig. 2.3. Schematic diagram of a scattering experiments.

the transitions was hard because the amount of the dispersed compound (lipid) in a pan was unknown due to the poor uniformity of the suspension.

2.2 Optical Microscopy

Phase contrast microscopy is an optical microscopy technique that makes use of diffraction and interference of light. [57, 58] It enables observation of a phospholipid membrane that is transparent in the observation by the bright field microscopy due to much smaller thickness (ca. 5 nm) than the wavelength of visible light. In the phase contrast observation, phase changes occurred in samples are visualized. When light (wavelength λ) passes through and diffracted by sample, its phase is delayed by $1/4\lambda$ compared to the background light. In phase contrast microscopy, the background light is phase-shifted by $1/4\lambda$ by passing through a phase shift ring, which results in bright or dark interference of the background and diffracted lights. Using phase contrast microscopy, we can observe the contour of giant unilamellar vesicles in black and also their thermal fluctuation in real time.

2.3 Scattering

Scattering techniques are useful to obtain microscopic information of samples in reciprocal space. The observable length scales of scattering techniques are different depending on the scattering angle. This property is suitable for exploring the hierarchical structure of lipid vesicles.

The basic scattering scheme is shown in Fig. 2.3. Considering interference of waves scattered at O and R, when a incident and a scattered beam with wavevectors $\vec{q}_i$ and $\vec{q}_s$, respectively, their phase

difference is expressed as

$$\frac{2\pi}{\lambda}(ON_1 - N_2R) = \frac{2\pi}{\lambda}\left(\frac{\vec{q}_s}{|\vec{q}_s|}\cdot\vec{r} - -\frac{\vec{q}_i}{|\vec{q}_i|}\cdot\vec{r}\right) = \vec{r}\cdot(\vec{q}_s - \vec{q}_i) = \vec{q}\cdot\vec{r} \tag{2.1}$$

where $\vec{q}$ and λ are the scattering vector and wavelength, respectively. When the scattering amplitude density of the scatterer is $\rho(\vec{r})$, the square of its Fourier transform is the scattering intensity $I(\vec{q})$ from the substance.

$$I(\vec{q}) \propto \left|\int \rho(\vec{r})\exp[i\vec{q}\cdot\vec{r}]dV\right|^2 \tag{2.2}$$

$\rho(\vec{r})$ is electron density in X-ray experiments while scattering length density in neutron experiments. Assuming that the sample is perfect crystal, $\rho(\vec{r})$ is expressed using reciprocal lattice vector $\vec{G}$ as

$$\rho(\vec{r}) = \sum_{\vec{G}} \rho_{\vec{G}}\exp[-i\vec{G}\cdot\vec{r}] \tag{2.3}$$

Therefore, the Fourier transform of Eq. 2.2 is

$$\int \rho(\vec{r})\exp[i\vec{q}\cdot\vec{r}]dV = \sum_{\vec{G}} \rho_{\vec{G}}\exp[i(\vec{q}-\vec{G})\cdot\vec{r}] \tag{2.4}$$

This equation means that the requirement for diffraction is $\vec{q} = \vec{G}$. When the angle between $\vec{q}_i$ and $\vec{q}_s$ is θ, assuming that $\vec{q}_i \approx \vec{q}_s$, the magnitude of $\vec{q}$ is expressed as,

$$|\vec{q}| = q = 2q_i\sin\left(\frac{\theta}{2}\right) = \frac{4\pi}{\lambda}\sin\left(\frac{\theta}{2}\right) \tag{2.5}$$

In Bragg's law which is applicable to a perfectly ordered system, interference occurs under the condition of $2d\sin\left(\frac{\theta}{2}\right) = n\lambda$, where d is the spacing between the scattering planes in the real space and n is an integer. In this case, q is written as $q = 2\pi/d$, which demonstrates the inverse relationship between the length scales in the real space and q at which the scattering from those length scales are reflected. This means that small structures are reflected in diffractions with large q.

Scattering can be elastic or inelastic (quasielastic). The former is scattering without an exchange of energy between the beam and the scatterer. Small- and Wide-angle X-ray Scattering (SAXS and WAXS) and Small-angle Neutron Scattering (SANS) are classified into this category. They sense the static structure of a sample. On the other hand, in the inelastic experiments that allow the energy exchange, the dynamic structure factor $S(q, \omega)$ is obtained by tracking the exchange $\hbar\omega$, where $\hbar$ and ω are Dirac's constant and relaxation frequency, respectively. When the transferred energy is very
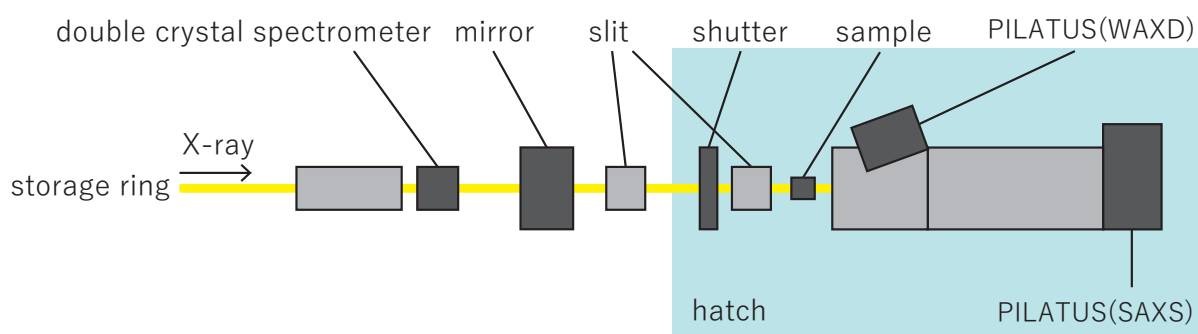
Fig. 2.4. SAXS and WAXS setup at BL10C and BL6C in Photon Factory, KEK.

small, we use the term quasielastic to characterize the process.

### 2.3.1 Elastic Scattering: Small- and Wide-angle X-ray Scattering (SAXS and WAXS) and Small-angle Neutron Scattering (SANS)

In scattering experiments, radiation sources should be selected to be suitable for the purpose since the scatterers are different depending on the radiation employed. X-rays and neutrons are the usual choices but scattered differently. X-rays are scattered by electrons, whereas neutrons by atomic nuclei. In X-ray experiments, light elements such as hydrogen (with a small number of electrons) are often missed when they are surrounded by heavy elements such as heavy metals. On the other hand, the scattering density is independent of the atomic number in the case of the scattering by a neutron. Protons can be sensitively observed. Further, we can modify the scattering density profile by substituting a part of protons to deuterium, which scatters neutrons differently because it is a different atomic nucleus. This method, known as the contrast variation, enables the detailed examination of structure. However, the neutron experiments have general demerits in comparison with X-ray: low resolution and long exposure time required due to weak incident beam strength.

In this study, SAXS and WAXS were employed to obtain bilayer thickness, face spacing of the bilayers in multilamellar vesicles, and lattice constants of lipid chains in the gel phase. SANS was conducted to explore the distribution of added molecules into bilayers by using deuterated additives and protiated lipids.

SAXS and WAXS experiments were conducted at BL10C and BL6A of Photon Factory (KEK, Japan) [59,60]. Electrons are accelerated in a high energy linac and bent by magnets in a storage ring, which yields the X-ray beam. The generated beam is guided to each hatch, as shown in Fig. 2.4. The incident X-ray wavelength can be changed depending on the desired q-range. The slits and mirrors are used to collimate and focus the beam. The direct beam is blocked by the beam stopper, which
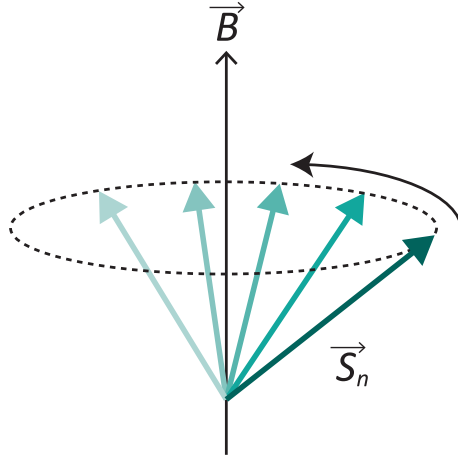
Fig. 2.5. Larmor precession of a neutron spin under the magnetic field.
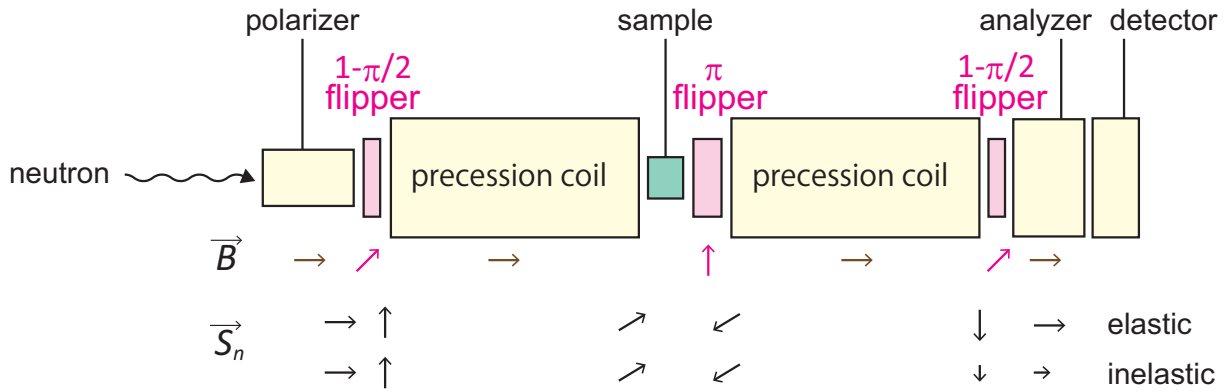
Fig. 2.6. NSE setup.

is also a photodiode. In this study, the detected intensity by the photodiode was used to normalize data. A silver behenate standard was used to calibrate sample-to-detector distances. A polyimide tube containing a sample was held in a hot stage (FP900, Mettler-Toledo Inc., Columbus, OH). The obtained two-dimensional profiles were reduced to one-dimensional profiles by circularly averaging with Nika [61], and the background correction was made by subtracting the profile of H_2O.

2.3.2 Quasielastic Scattering: Neutron Spin Echo (NSE)

NSE technique enables the direct measurement of the dynamic structure factor $S(q, \omega)$ by tracking the energy exchanges between the neutrons and the sample at a specific length scale q. [62] The time- and length-scales that NSE technique covers are suitable to observe membrane dynamics such as the bending and thickness fluctuations. [63] In NSE experiments, the spin that a neutron has plays a role in sensing the velocity difference due to energy exchange between the neutrons and the sample. A spin degree of freedom of 1/2 gives a neutron a magnetic moment. When the neutron spin is

perpendicular to the magnetic field, the spin starts to rotate around the magnetic field, as shown in Fig. 2.5. The motion is called Larmor precession. In the NSE setup (Fig. 2.6), the incident beam is polarized using a polarizer to select one state of neutron spins. The spins are then, flipped to the perpendicular orientation to the magnetic field by the first $\pi/2$-flipper. The neutrons undergo Larmor precession in the first precession coil at the precession frequency governed by the magnetic field. After passing through the sample, the precession angle is reversed by the π-flipper, and the neutrons enter the second precession coil. At the end of the second precession coil, the polarization of the spin is restored to its state before entering the first precession coil because of the same length and magnetic field of two precession coils. After the second precession coil, a $\pi/2$-flipper stops the precession of the neutrons, and then the partially polarized spins are introduced to the spin analyzer and reach the detector. The detected neutron intensity I_A is expressed as $I_A = (1 + \cos\phi/2)$, where ϕ is the angle between the neutron spin and the magnetic field. If the neutrons are scattered elastically, the initial polarization is recovered, which means $\phi = 0$ and $I_A = 1$. On the other hand, if the neutrons are quasi-elastically scattered, the change in the neutron velocity results in $\phi \neq 0$, which means that the spin polarization at the analyzer is rotated by ϕ from the initial polarization. In this case, I_A at the detector is decreased. The measured neutron intensity is written as

$$I \propto \int S(q,\omega)\cos(\omega t)d\omega \tag{2.6}$$

due to the cosine probability of the neutron spin direction is allowed to pass through the spin analyzer. Eq. 2.6 is a cosine Fourier transformation of $S(q,\omega)$ which is equivalent to $I(q,t)$. t is called fourier time and is defined as

$$t \equiv 2\pi\gamma_L \left(\frac{m_n}{\hbar}\right)^2 \lambda^3 J \tag{2.7}$$

where γ_L, m_n and J are Larmor constant, the mass of a neutron and the integrated magnetic field along the neutron pathway. In NSE experiments, the normalized intermediate scattering function $I(q,t)/I(q,0)$ is used to describe the time correlation function at each q. The change in q can be achieved by changing the angle between the first and the second precession coils.

Chapter 3

Effects of Straight Chainlike Molecules on Physicochemmical and Mechanical Properties of DPPC Bilayers

In this chapter, incorporation effects are investigated in cases for chainlike additives, whose molecular shapes are similar to that of the host. The host medium, DPPC bilayers have straight alkyl chains in the hydrophobic region. We chose n-alkanes and its derivatives as straight chainlike molecules and investigate their effects on structure, phase behavior, mechanical properties, and dynamics.

3.1 Effects of n-Tetradecane Derivatives on Structure and Phase Behavior of DPPC Bilayers

3.1.1 Introduction

A core-like molecule, cholesterol, and a flexible chain molecule, n-alkanes, have contrasting effects on T_m and molecular packing [18, 21–23, 25]. T_m becomes lower and the packing in the gel phase is loosened when a core-like molecule, cholesterol, is incorporated whereas T_m rises and the packing is tightened in the gel phase by incorporation of n-tetradecane. These results suggest that the structural features of incorporated molecules mostly determine their effects. That is, there is a possibility to systematically understand the incorporation effects, though the effects of the incorporated molecules have widely been discussed individually.

We hypothesized that the incorporation effects are the same when the incorporated molecules share structural similarity. To clarify whether this hypothesis is correct, we have investigated the

incorporation effects of *n*-tetradecane derivatives, each of which has a tetradecyl group and a terminal group. Although the effects on the hydrophilic region of bilayer would differ by size, hydrophilicity, or acid dissociation constant of the incorporated molecules, the property of the molecular packing and the phase behavior are expected to be similar if the steric hindrance of the incorporated molecules is similar. Note that molecules within biomembranes often have functional groups such as OH and COOH on their ends [64]. Although the cases for X = H, OH, COOH have been investigated thus far, general understanding has not been reached. The investigation of various terminal groups should contribute to understandings having broad applicability.

3.1.2   Materials & Methods

We investigated the effects of nine derivatives of *n*-tetradecane. They are designated as C14-X (X = H, Br, Cl, COOCH$_3$, SH, OH, COOH, PO$_3$H$_2$, NH$_2$) in the following. Tetradecane (C14-H) and 1-tetradecanol (C14-OH) were purchased from Wako Pure Chemical Industries, Ltd. (Osaka, Japan). 1-Bromotetradecane (C14-Br), 1-chlorotetradecane (C14-Cl), methyl myristate (C14-COOCH$_3$), 1-tetradecanethiol (C14-SH), myristic acid (C14-COOH), tetradecylphosphonic acid (C14-PO$_3$H$_2$) and 1-tetradecylamine (C14-NH$_2$) were obtained from Tokyo Chemical Industry Co., Ltd. (Tokyo, Japan). As a phospholipid, DPPC (Wako Pure Chemical Industries, Ltd. Osaka, Japan) was used. They have the purity > 98% and used in experiments without further purification.

To avoid evaporation of C14-X, some of which have low boiling points, we employed the following drying procedure. C14-X and DPPC were dissolved separately in organic solvent of chloroform and methanol (2:1 v/v) to give concentrations of 50 and 100 mM, respectively. The DPPC solution was first pipetted into glass tubes, and the solvents were evaporated. The resulting dry films were placed under vacuum for 12 h or longer. After adding each C14-X solution at the desired molar ratio (denoted in mol % in the DPPC/C14-X mixture) to the film, the solvents were evaporated. The samples were placed under vacuum for 30 min. The amount of the solvent for C14-X was small enough to dry in 30 min (confirmed through the weight change). Then, 60 μl of ultra-pure water (MilliQ, 18.2 MΩ cm) was added into each glass tube, yielding a concentration of 83 mM. The dispersions were sonicated for 3 h at 60 °C in an ultrasonic bath (US-101 from SND Co., Ltd (Nagano, Japan)).

Structural changes in the bilayer caused by incorporated C14-X were studied using X-ray diffraction experiments. WAXS experiments were carried out at BL6A in the Photon Factory, KEK [60]. PILATUS3 200K (DECTRIS Ltd., Baden, Switzerland) detector was employed. The X-ray beam was monochromatized to 1.5 Å using a Johann type crystal monochromator, with a Ge (111) asymmetrically cut crystal. All measurements were performed for the gel phase at 25 °C.

The phase behaviors of DPPC/C14-X bilayers were examined using DSC. In the measurements, cooling/heating cycles were repeated three times between 20 and 62 °C. The first cycle was at a scan rate of 2 °C min^{-1}, and the second and the third were at 5 °C min^{-1}. We confirmed that the curves of the second and the third cycles were comparable.

3.1.3 Results & Discussion

Figure 3.1 shows typical WAXS profiles. A diffraction peak observed around $q = 1.5$ Å was derived from the positional order of lipid alkyl chains within the bilayer in the gel phase. Similar WAXS profiles were obtained for all C14-X. The peak is asymmetric in the cases for the pure DPPC bilayer and the DPPC/C14-H bilayers at lower C14-H contents. This asymmetry is due to the centered rectangular lattice formed by tilted lipid alkyl chains. The centered rectangular lattice can be regarded as a distorted hexagonal lattice. With increasing C14-H content, the peak becomes symmetric, reflecting the establishment of the hexagonal lattice shown in Fig. 3.2. Therefore, the averaged lattice constant s defined by Marsh *et al* [65] was calculated from the peak position $q = 2\pi/s$ of the asymmetric peak treated as a single peak derived from the undistorted hexagonal lattice. The mean distance between the alkyl chains is given approximately by $2s/\sqrt{3}$. Figure 3.3 shows the content dependence of s for DPPC bilayers with C14-X. The s of the pure DPPC bilayer is in good agreement with the reported values [65, 66]. The s decreases with the decrease in the C14-X content for all cases. The decrease in s agrees with the reported behavior for C14-H [24, 25]. Figure 3.4 summarizes s of all systems. It is noted that the difference between the maximum and minimum s was 0.05 Å in a few experiments on nominally the same system. Figure 3.4 thus indicates that the effects of the addition are roughly the same for all C14-X.

The decrease shown in Fig. 3.4 indicates that the molecular packing was densified similarly by incorporated C14-X regardless of X. The change in the lateral packing of the chains indicates that all the C14-X used in this study arranged in parallel to the lipid alkyl chains, as shown in Fig. 3.5. In the pure DPPC bilayer, the alkyl chains are tilted to make the chain-chain lateral distance shorter against the large headgroup of DPPC and make the gap in the hydrophobic region narrower. It is assumed that linear alkyl chain-based molecules fill the gap in the hydrophobic region in contrast to a core-like molecule, cholesterol, which disorders the chain packing in the gel phase. Chemical species dependence of the incorporation manner is considered to be relatively weak, judging from the WAXS results. Effects of C14-X on the chain packing are similar to each other, although the terminal groups have varied in size, dipole moment, and acid dissociation constant. For example, the largest X, $COOCH_3$ is at least seven times larger than the smallest headgroup, H, and pH should change when

C14-PO$_3$H$_2$ and C14-NH$_2$ are added. In a previous study [25], the main transition temperature T_m is reported to be higher as s decreases. The change in packing in the hydrophobic region affects T_m. T_m is expected to rise by the incorporation of C14-X. Therefore, we investigate the phase behaviors of DPPC/C14-X bilayers using DSC.
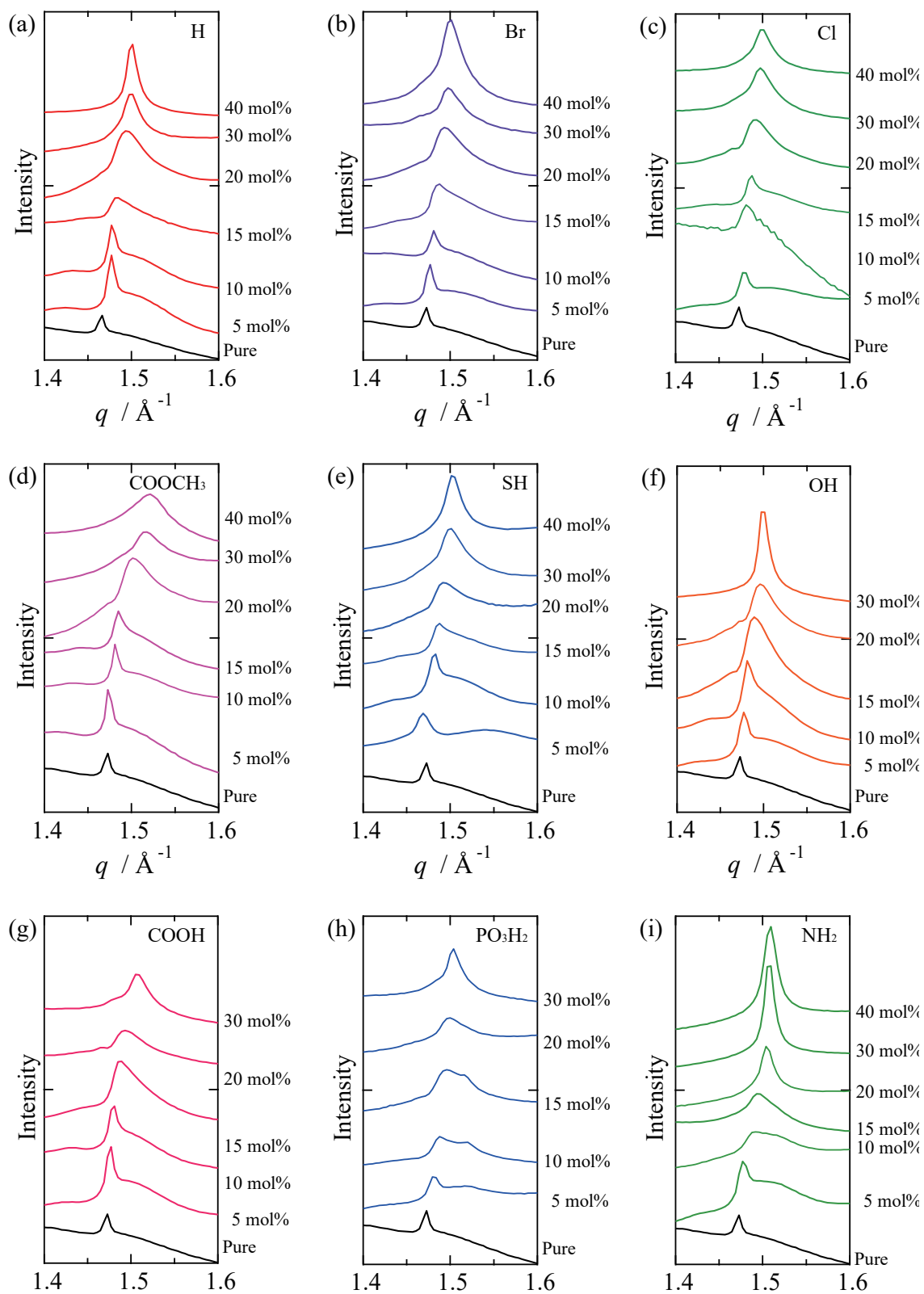
Fig. 3.1. WAXS profiles of pure DPPC (black line) and DPPC containing C14-X (colored lines) at 25 °C. X to C14-X ratio are shown in the figure.
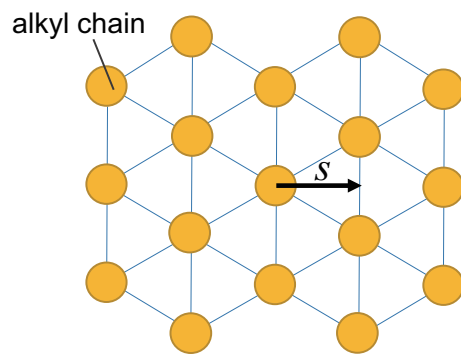
Fig. 3.2. Schematic diagram of a hexagonal lattice of alkyl chains in a lipid bilayer in the gel phase.
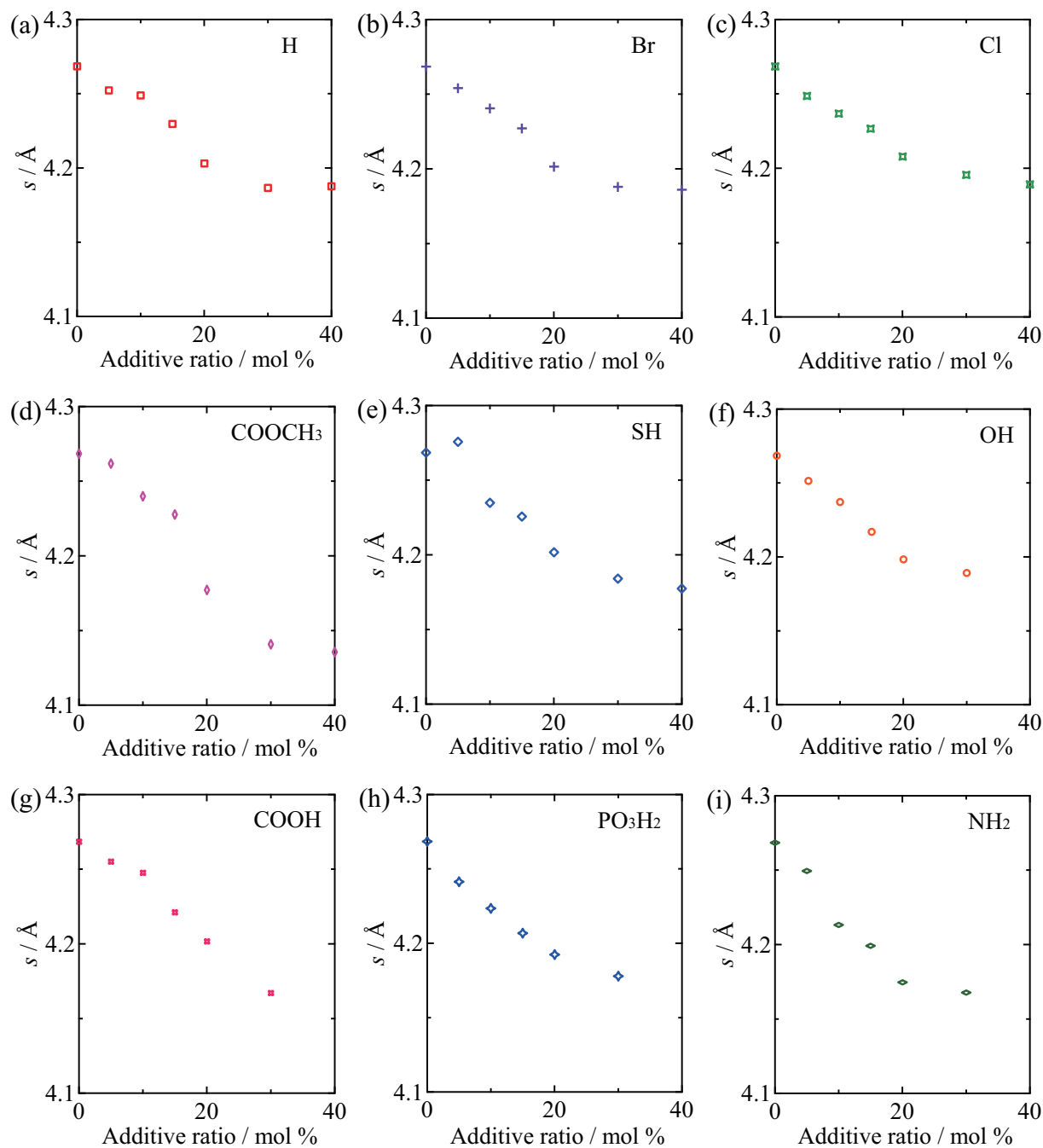
Fig. 3.3. The hexagonal lattice constant s of the alkyl chains in DPPC bilayers containing C14-X, obtained from the peak position of the WAXS profiles. X to C14-X ratio are shown in the figure.
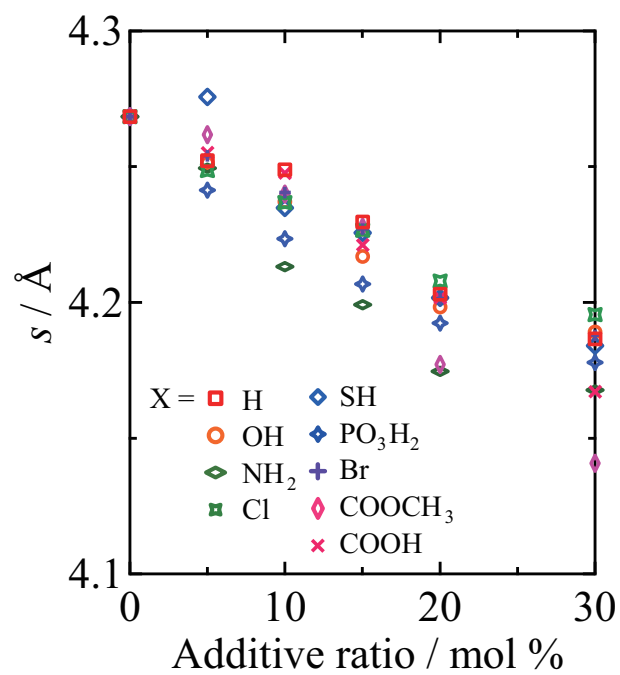
Fig. 3.4. *s* with various X.
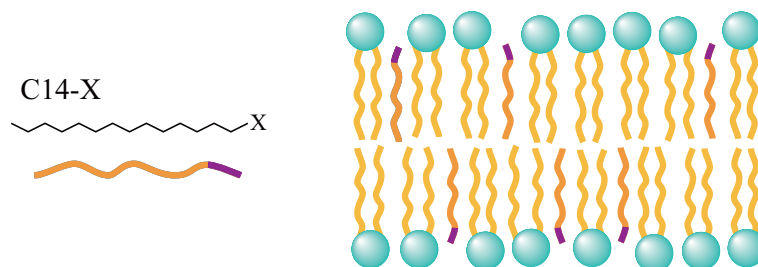
C14-X

Fig. 3.5. Incorporation manner of C14-X in a bilayer.

Figure 3.6 shows the DSC curves of the DPPC/C14-X bilayers. The thermal anomaly is due to the main transition between the gel phase and the liquid-crystalline phase. Pure DPPC bilayer undergoes the pretransition at a lower temperature than the main transition. However, the pretransition disappears in DPPC/C14-X systems even when the ratio is 10 mol %. These results are consistent with a reported phase diagram of DPPC-C14COOH [67]. Upon increasing the C14-X content, the anomaly of the main transition shifts to higher temperatures with broadening. The behavior agrees with the reported results and is contrasting compared to the effect of a core-like molecule, cholesterol. The elevation in T_m is observed in all the DPPC/C14-X in Fig. 3.6. Although the broadening of the thermal anomaly is plausibly a symptom of phase separation, it can be said that T_m, where Gibbs energies of two phases cross, shifts to a high temperature in all C14-X because T_m indeed lies between two end temperatures of phase separation.

The relevance of the observed decrease in s and the rise in T_m has been explained on a thermodynamic view point [25]. T_m is determined by the ratio of transition enthalpy and transition entropy, i.e. $T_m = \Delta H / \Delta S$. The influence of the entropy change on T_m is considered being small compared to the enthalpy change in the lipid bilayers in the previous study that investigated the effects of n-alkanes with different chain length [25]. In the study, the chain length dependence of the main transition temperature was sensitive over 50 times to the difference in enthalpic interaction between the added n-alkanes and host than that of entropy. Besides, all the derivatives are considered having large partition coefficients, $K = [\text{C14} - \text{X}]_{\text{membrane}}/[\text{C14} - \text{X}]_{\text{water}}$ since the coefficients of C14-COOH which is hydrophilic molecule is 50000 and more than 99.99 % of the C14-COOH molecules partition into bilayers [68]. Thus, the entropic contribution is small [69, 70]. Further, the concentrations of DPPC and tetradecane derivatives are generally high in the systems under investigation. Considering that the contribution of entropy S on T_m is small, the enthalpy H reduction in the gel phase seems larger than in the liquid-crystalline phase as the packing of the lipid chains is densified in the gel phase. As a result, ΔH, the difference in enthalpy between the two phases, increased and T_m rose.

Now we discuss the X dependence of phase behavior by comparing the DSC curves of DPPC/C14-X bilayer at a C14-X ratio of 30 %. Although T_m rises with all the C14-X, the apparent temperature range of thermal anomaly is different depending on X, as seen in Fig. 3.7. In the cases of X = H, COOCH$_3$, Cl, and Br, the anomaly is relatively sharp and the rises in T_m are relatively small. In contrast, the anomaly is broadened to a larger extent and the peak appears at higher temperatures for X = SH, COOH, NH$_2$, PO$_3$H$_2$, and OH. These terminal groups have hydrogen atom bound with electronegative atoms. Thus, the broadening may result from hydrogen-bonding between C14-X and DPPC molecules. Indeed, the hydrogen-bonding with lipid has been reported in the cases for X =

OH, and COOH [67, 71–73]. It was reported [67, 74] that the phosphate group and the two carbonyl groups in a lipid molecule accept the hydrogen bond.

The main event of the main transition has usually been considered as the melting of the alkyl chains. Indeed, extrapolation of the main transition temperatures of the saturated diacyl phosphatidyl-choline vs. the reciprocal of the chain length to the infinitely long chain gives 150 °C which is close to the melting temperature of polyethylene [75]. Besides, all the nonlamellar reflections observed in an X-ray measurement can be interpreted by assuming the chain lattice [76]. Although the packing of alkyl chains is similar for the samples we used, the phase behaviors exhibit X-dependence. Our results indicate that interaction in the hydrophilic region of phospholipids strongly affects the phase behavior of phospholipid bilayers. The headgroup dependence widely observed so far [77] is derived from the difference in the hydrophobic region caused by different interactions between headgroups.
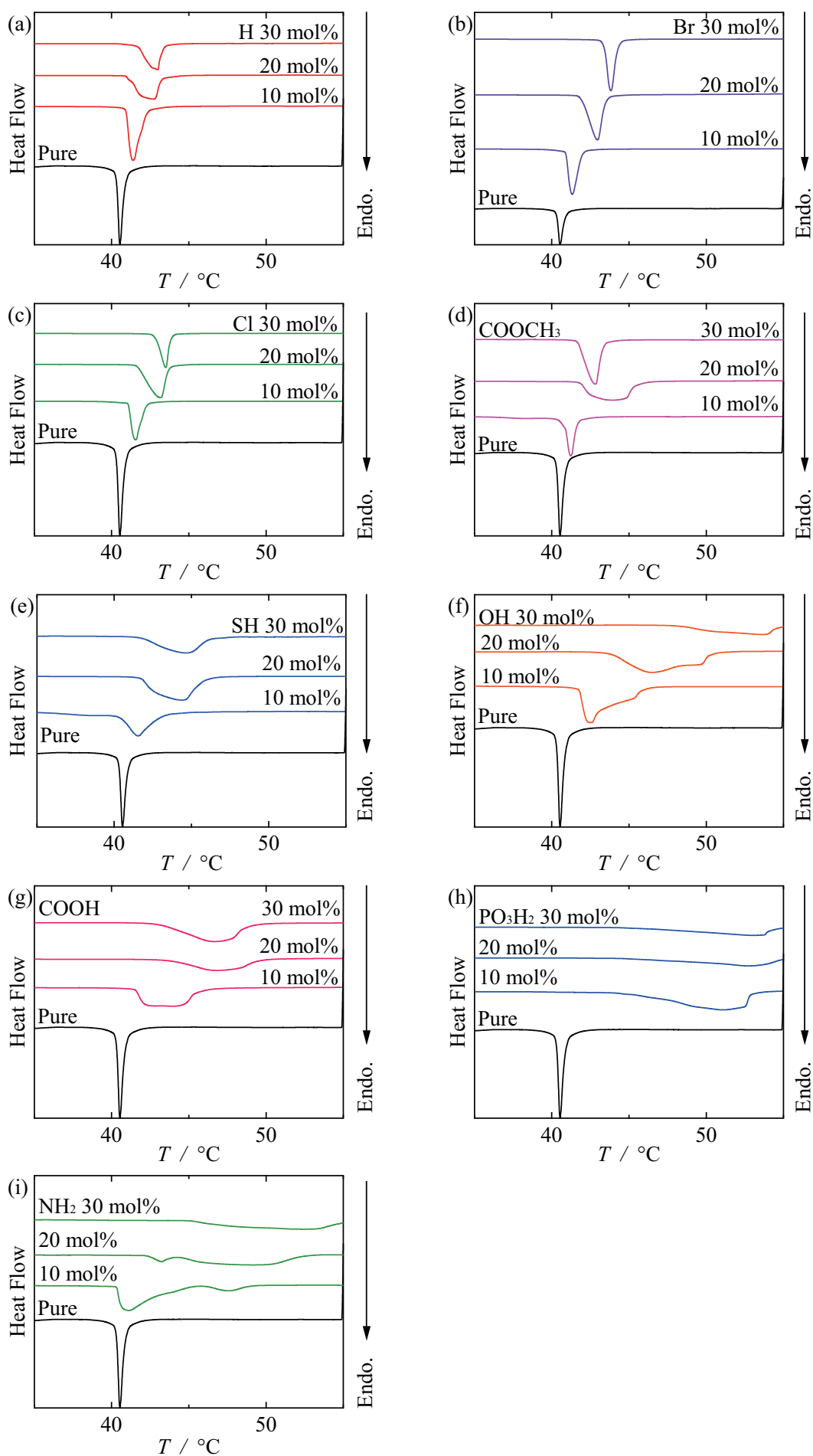
Fig. 3.6. DSC curves on heating of pure DPPC and of DPPC/C14-X bilayers containing various C14-X content as indicated.

31
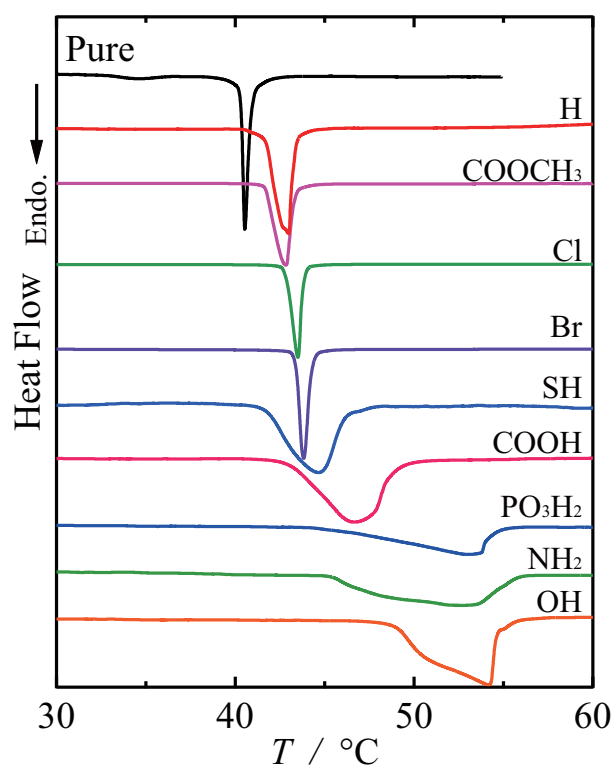
Fig. 3.7. DSC curves of pure DPPC and of DPPC containing 30 mol % of C14-X.

3.1.4 Conclusion

The trends of the densified chain packing and the rise in T_m are commonly observed for all the DPPC/C14-X system, although the chemical species dependence appears in the temperature range of the thermal anomaly. The common trends suggest straight chainlike molecules within lipid membranes have universal effects on molecular packing and phase behavior of DPPC bilayers even if their terminal groups are different. The results suggest that a *n*-alkane can be used as a representative of chainlike molecules.

3.2 Effect of *n*-Tetradecane on the Bending Elasticity of DPPC Bilayers

3.2.1 Introduction

The effects of *n*-alkanes on the structure and the phase behavior have been investigated thus far [25, 33, 78], whereas it is unknown how mechanical properties of the membrane are affected by the incorporation of *n*-alkanes. In the case of a core-like molecule, cholesterol, the bending modulus κ of DMPC bilayers increases in the liquid-crystalline phase [79, 80], indicating that the membrane becomes rigid by the incorporation of cholesterol. On the other hand, a simulational study revealed that κ decreases in the gel phase [81]. When a straight chainlike molecule, *n*-tetradecane (C14), is added to the DPPC bilayers, κ becomes ten times larger than that of the pure DPPC bilayer due to the close packing of alkyl chains of DPPC and C14 [24]. This influence is opposed to that of cholesterol as other membrane properties are affected by cholesterol and a *n*-alkane oppositely. Influences on κ are not known for the incorporation of a straight chainlike molecule in the liquid-crystalline phase. κ will decrease if the effect on κ is also opposed to that of cholesterol, whereas increase if the membrane rigidity is affected by the packing parameter since the effective packing parameter will be close to 1 by the incorporation.

In this section, the change in κ induced by the incorporation of straight chainlike molecules is described for the liquid-crystalline phase. Section 3.1 established the universal trends in the effects of straight chainlike molecules on the structure and the phase behavior of DPPC bilayers irrespective of the terminal groups of the added molecules. The result indicates that a *n*-alkane can be used as a representative of chainlike molecules. We thus use DPPC and C14 as a phospholipid, and a straight chainlike molecule, respectively, and vesicle fluctuation is analyzed to estimate κ using a phase-contrast microscope.

3.2.2 Theory

In microscopic observation of a phospholipid vesicle, we can record the thermal fluctuation of membranes. Since the membrane tension and the bending modulus determines the fluctuation amplitude and wavelength, the analysis of the fluctuation of the membranes yields these parameters. Indeed, the thermal fluctuation of a phospholipid vesicle has been studied theoretically and experimentally. In theoretical models, the volume and membrane area of the vesicle are assumed to conserve during the observation. [13] As described in Chapter 1, the stretching elastic energy per unit area is expressed

as,

$$F_{\rm s} = \frac{k_{\rm s}}{2}\left(\frac{\Delta S}{S_0}\right)^2 \quad (\Delta S = S - S_0) \tag{3.1}$$

$$\sigma = S_0\frac{\partial F_{\rm s}}{\partial S} = k_{\rm s}\left(\frac{\Delta S}{S_0}\right) \tag{3.2}$$

where σ is the membrane tension, S_0 is the equilibrium area of the membrane, which is the area at $\sigma = 0$, S is the deformed area of the same membrane, and $k_{\rm s}$ is the stretching elastic modulus. When a small piece of a membrane is bent, the bending elastic energy is expressed as [5],

$$F_{\rm c} = \frac{\kappa}{2}(c_1 + c_2 - c_0)^2 + \bar{\kappa}c_1c_2 \tag{3.3}$$

where c_1 and c_2 are the principal curvatures, and c_0 is the spontaneous curvature of the membrane. κ and $\bar{k}_{\rm c}$ are the cylindrical and saddle bending modulus respectively.
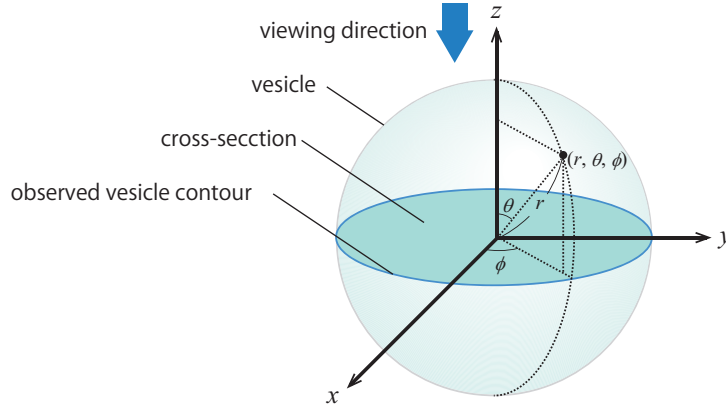
Fig. 3.8. Spherical polar coordinates (r, θ, ϕ), with origin in the center of the vesicle.

The vesicle membrane is considered as a two-dimensional surface. In spherical polar coordinates (r, θ, ϕ), with origin in the center of the vesicle, as shown in Fig. 3.8, a slightly deformed surface is expressed as.

$$r(\theta, \phi, t) = R[1 + u(\theta, \phi, t)]. \tag{3.4}$$

R is the radius of a sphere with the same volume as that of the vesicle, and $u(r, \theta, \phi)$ is a function representing the relative displacements of the vesicle membrane from the sphere surface. The thermal fluctuation of the membrane is much smaller than the size of the vesicle, $u(r, \theta, \phi) \ll 1$. The membrane fluctuations are thermal agitations around the equilibrium vesicle shape depending on time. The vesicle form $u(\theta, \phi, t)$ of a certain moment can be decomposed to the two contributions; a static component (θ, ϕ) and a dynamical component $\delta u(\theta, \phi, t)$. (θ, ϕ) is the time-averaged vesicle shape and the deviation from it is represented by $\delta u(\theta, \phi, t)$. The shape of a fluctuating vesicle is expressed

as,

$$u(\theta,\phi,t) = u_0(\theta,\phi) + \delta u(\theta,\phi,t) \tag{3.5}$$

$$\langle u(\theta,\phi,t) \rangle = u_0(\theta,\phi) \rightarrow \langle \delta u(\theta,\phi,t) \rangle = 0 \tag{3.6}$$

where the angle brackets denote time average. The above equation means that the time average of u and $_d eltau$ is equal to u_0 and 0, respectively. The vesicle shape in equilibrium is determined by minimizing the free Gibbs energy. The total energy of the membrane is,

$$F(u) = F_s(u) + F_c(u) - \Delta p V(u) \tag{3.7}$$

where F_s and F_c are the stretching and bending elastic energy, respectively, V is the vesicle volume and Δp is Lagrange multiplier that is, physically, the hydrostatic pressure difference between the outside and inside of the vesicle. When the function u_0 minimizes the $F(u)$, $\delta F(u)$ is zero for all small variation, δu, that is.

$$\delta F(u, \delta u) = 0 \tag{3.8}$$

Since u_0 minimizes the $F(u_0)$,

$$\delta^2 F(u, \delta u) \geq 0 \tag{3.9}$$

If we solve these equations,

$$\delta u(\theta,\phi,t) = \sum_{l=0}^{l_{max}} \sum_{m=-l}^{m=+l} U_l^m(t) Y_l^m(\theta,\phi) \tag{3.10}$$

$Y_l^m(\theta,\phi)$ is the spherical harmonics and, using Legendre polynomial, it is defined as [82].

$$Y_l^m(\theta,\phi) = (-1)^m \sqrt{\frac{2l+1}{4\pi}\frac{(l-m)!}{(l+m)!}} P_m^l(\cos\theta) e^{im\phi} \tag{3.11}$$

l and m are integers and $m = -l, -(l-1), \ldots, 0, \ldots, l-1$. The eigenvalues of $Y_l^m(\theta,\phi)$ are,

$$\lambda_l(\bar{\sigma},\bar{p}) = l^2(l+1)^2 - (2-\bar{\sigma})l(l+1) + 2(\bar{\sigma}-\bar{p})$$

$$\bar{p} = \frac{\Delta p R^3}{\kappa} + 2c_0 R, \quad \bar{\sigma} = \frac{\sigma R^2}{\kappa} + 2c_0 R + \frac{c_0^2 R^2}{2} \tag{3.12}$$

$\bar{p}$ and $\bar{\sigma}$ are the effective dimensionless pressure and tension, respectively. The mean-squared ampli-

tude of the spherical harmonics is expressed as,

$$\langle |U_l^m(t)|^2 \rangle = \frac{k_B T}{\kappa} \frac{1}{\lambda_l(\bar{\sigma}, \bar{p})}, \, l \geq 2$$

$$= \frac{k_B T}{\kappa} \frac{1}{(l-1)(l+2)[l(l+1)+\bar{\sigma}]+2(2\bar{\sigma}-\bar{p})} \qquad (3.13)$$

$$= \frac{k_B T}{\kappa} \frac{1}{(l-1)(l+2)[l(l+1)+\bar{\sigma}]}$$

Since we assume that the volume conservation, the mode of $l = 0$ that is vesicle expansion is 0. The mode of $l = 1$ which means vesicle diffusion is also 0 since the origin of polar coordinates is defined as the center of the vesicle. Also, $2(2\bar{\sigma} - \bar{p})$ is very small ($\bar{p} \approx 2\bar{\sigma}$) and can be approximated as 0. Therefore, we can estimate the bending modulus if we obtain the relation between $\langle |U_l^m|^2 \rangle$ and measurable values in experiments. If we assume that the equatorial cross-section of a vesicle is at the focal plane of the objective, the cross-section coincides with the XY plane of the coordinate system where $\theta = \pi/2$, as shown in Fig. 3.8. The radius of the equatorial cross-section is,

$$r(\phi, t) = R \left[1 + u \left(\frac{\pi}{2}, \phi, t \right) \right] \qquad (3.14)$$

In experiments, the following normalized angular autocorrelation is measurable.

$$\xi(\gamma) = \frac{1}{2\pi} \int_0^{2\pi} \frac{[r(\phi+\gamma,t)-R][r(\phi,t)-R]}{R^2} d\phi \qquad (3.15)$$

Following Eq. 3.10, the time average of $\xi(\gamma, t)$ is calculated as,

$$\xi(\gamma) = \langle \xi(\gamma, t) \rangle = \sum_{l=2}^{l_{max}} \sum_{m \neq 0} \langle |U_l^m(t)^2 \rangle Y_l^m \left(\frac{\pi}{2}, 0 \right) Y_l^m \left(\frac{\pi}{2}, \gamma \right) \qquad (3.16)$$

combining with Eq. 3.13,

$$\xi(\gamma) = \frac{k_B T}{4\pi\kappa} \sum_{l=2}^{N_{max}} \frac{2l+1}{(l-1)(l+2)[l(l+1)+\bar{\sigma}]} P_l(\cos\gamma) \qquad (3.17)$$

This equation means that the time average of the angular autocorrelation function is a series of Legendre polynomials, whose coefficients are determined by equipartition law. $(2l+1)$ reflects that there are $(2l+1)$ modes with different m for each l. 4π originates from the normalizations of Legendre polynomials and spherical harmonics. The amplitude B_l of Legendre polynomials is expressed as

$$B_l(\bar{\sigma}, \kappa) = \frac{2l+1}{4\pi} \langle |U_l^m(t)|^2 \rangle, \, l \geq 2 \qquad (3.18)$$

37

Using this relation, we can estimate the bending modulus κ from experiments. We fit the following equation to the autocorrelation functions obtained in experiments and estimated B_l.

$$\xi(\gamma) = \sum_{l=2}^{N_{max}} B_l P_l(\cos\gamma) + a P_1(\cos\gamma) + b P_2(\cos\gamma) \tag{3.19}$$

3.2.3 Materials & Methods

Commercial DPPC and tetradecane (C14) (Wako Pure Chemical Industries, Ltd. Osaka, Japan) were used. They have the purity $> 98\%$ and used in experiments without further purification. C14 and DPPC were dissolved separately in organic solvent of chloroform and methanol (2:1 v/v) to give concentrations of 10 mM.

For the preparation of DPPC/C14 (DPPC : C14 = 6 : 4 (mol:mol)) bilayers, 6 μL of the DPPC solution was pipetted into a glass tube, and the solvents were evaporated. The resulting dry films were placed under vacuum (-0.06 MPa) at least for 45 min, and 4 μL of the C14 solution was added to the dry films. The solvents were evaporated again, and then, the resulting dry films were left under vacuum (-0.04 MPa) for 30 min. This procedure was necessary since C14 more likely evaporates than DPPC. To obtain pure DPPC giant unilamellar vesicle (GUV), we took the following procedure.10 μL of DPPC solution is pipetted into a glass tube, and left in a vacuum (-0.06 MPa) until the solvents were evaporated. 200 μl of ultra-pure water (MilliQ, 18.2 MΩ cm) was added to the dry films yielding a concentration of 0.5 mM and then left at 65 $^\circ$C for 2 h.

Observation and registration of vesicle images were performed in the following steps. The sample solution was pipetted on a glass plate with a spacer and covered with another glass plate. The glass plates with the sample were put on the sample stage of an inverted microscope (OLYMPUS IX71) and observed in phase contrast through a 1.6 variable magnification lens and a 40x objective lens at 50 $^\circ$C where the membrane is in the liquid-crystalline phase. The digital camera connected to the microscope recorded video of GUV at 30 frames/s in 1080 x 1920 pixel format. The video was converted to grayscale stack, and images were collected every 30 images, which means every 1 s, using image processing software, imagej [83].

3.2.4 Results & Discussion

Figure 3.9 shows the typical phase-contrast images of GUV. The membrane of a vesicle is visible as a dark ring, and the background looks bright gray. There is no distinct difference between vesicles of the pure DPPC and DPPC/C14 (DPPC : C14 = 6 : 4 (mol:mol)) in Fig. 3.9. The image stack of
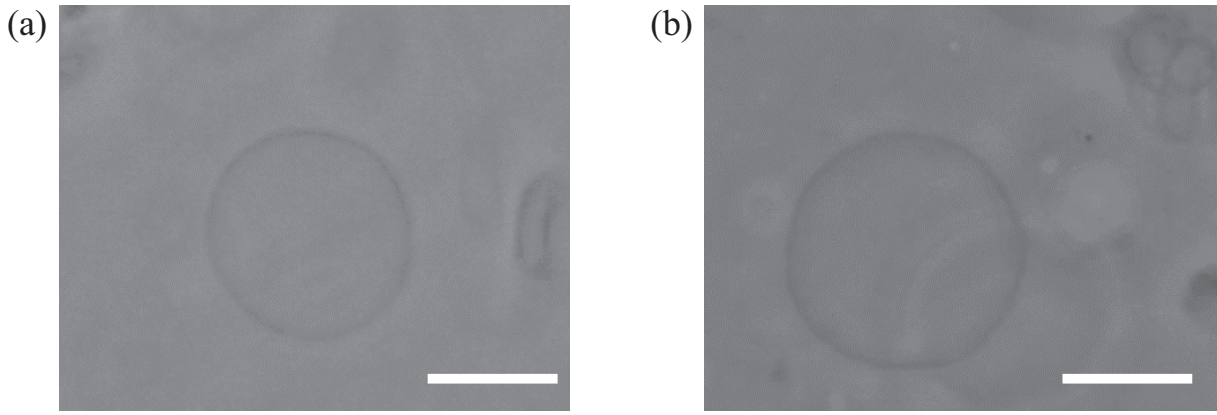
Fig. 3.9. Typical phase-contrast images of GUV contour in the cases for (a) the pure DPPC and (b) DPPC/C14 (DPPC : C14 = 6 : 4 (mol:mol)) at 50 °C. Scale bar, 20 μm.
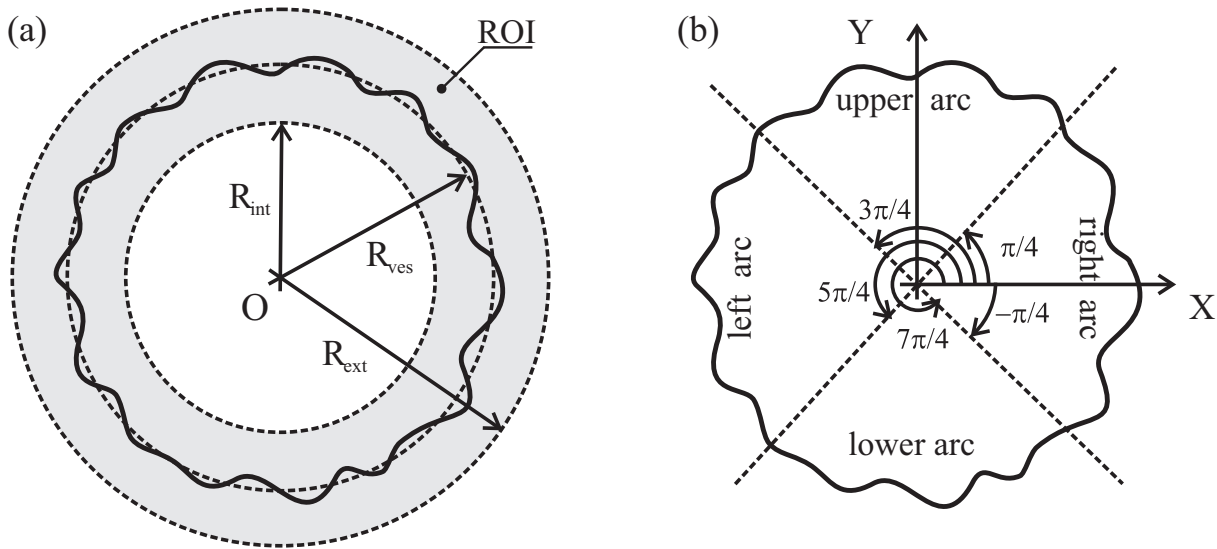
Fig. 3.10. (a) Region of interest (ROI) containing the contour of a vesicle. (b) Schematic diagram of the vesicular image cut for the analysis [84].

a spherical vesicle was used for analysis if it was isolated from other vesicles, and its diameter was around 20 μm. In analysis, the center O and the radius R_{ves} of the vesicle is roughly determined from the image, and region of interest (ROI) is delimited by two concentric circumferences with radii R_{ext} and R_{int}, where $R_{ext}, R_{int} = R_{ves} \pm 15 pixel$, as shown in Fig. 3.10a. The intensity of the pixels was set equal to the background outside of ROI. Then, the intensity was scanned along the rows or columns to extract the coordinate of a vesicle contour. The image is divided into four arcs, as shown in Fig. 3.10b. We scanned the image along the row for right and left arcs and along the column for the upper and lower arcs. A binary image was generated by setting value 0 at the pixel whose intensity was minimum in the row or column and setting value 200 to other pixels. The coordinate of the true vesicle center O' was determined as the average coordinate of the pixels with 0 value.
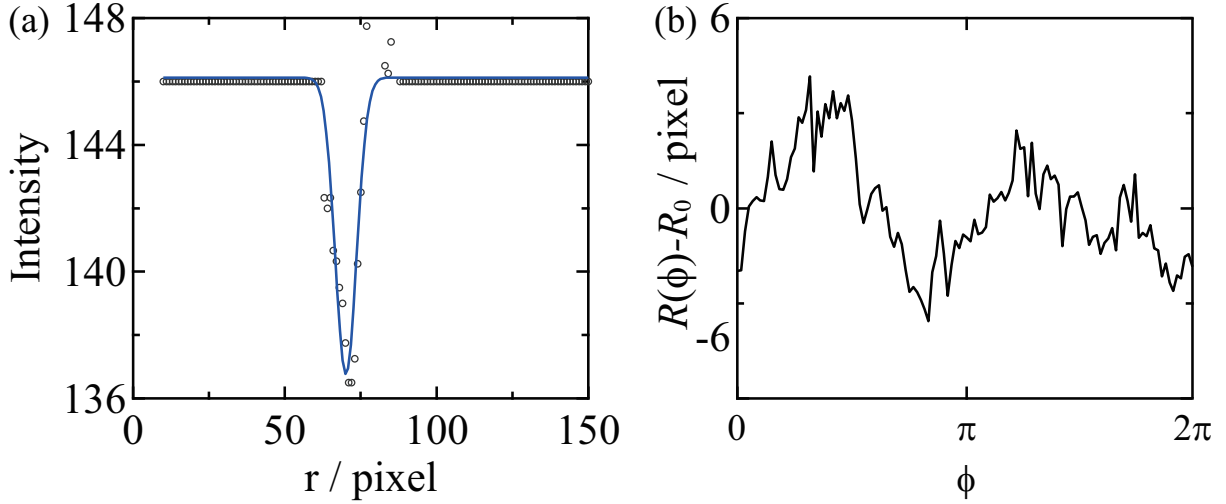
Fig. 3.11. (a) Intensity against the distance from the vesicle center. (b) The difference between radius and the mean radius against ϕ.

The image without binarization was divided into 120 sectors whose central angle and center are $3\,^\circ$ and O', respectively, and in each sector, the average intensity as a function of the distance to O' was calculated, as shown in Fig. 3.11a. The low intensity reflects the vesicle contour. Then, Gaussian fitting to the intensity locates the contour position $R(\phi)$ for each sector, and $R(\phi) - R_0$ is plotted against the angle ϕ as shown in Fig. 3.11b. The two maximum indicates that the contour is nearly elliptical. The angular autocorrelation functions $\xi(\gamma)$ of $R(\phi) - R_0$ were calculated according to Eq. 3.15 for each image of the vesicle and averaged. Figs. 3.12a and 3.13a shows the average ξ of DPPC and DPPC/C14 bilayers, respectively. $\xi(\gamma)$ is symmetric about $\phi = \pi$ since $\xi(\gamma) = \xi(2\pi - \gamma)$. The Legendre amplitude B_l was estimated up to $l = 20$ following previous research [13], by fitting Eq. 3.19 to $\xi(\gamma)$ and plotted against l in Figs. 3.12b and 3.13b. B_l is largest at $l = 2$ and becomes smaller as l increases. The dependence is reasonable since the mode $l = 2$ is a mode of variation between a circle and an ellipsoid. In the range $l \geq 15$, B_l slightly increases against l. This increase is probably due to that the pixel size is smaller than true B_l or that the correlation time is shorter than the integration time of the video.

κ was estimated by fitting Eq. 3.18 to B_l as shown in Figs. 3.12b, 3.13b. The results for the pure DPPC bilayer are $\kappa = (1.6 \pm 0.2) \times 10^{-19}$ J and $\sigma = (5.7 \pm 2.7)^{-6}$ mN m^{-1}. In the case for DPPC/C14 bilayer, the results are $\kappa = (1.4 \pm 0.2) \times 10^{-19}$ J and $\sigma = (5.2 \pm 1.8)^{-6}$ mN m^{-1}. The κ for the pure DPPC bilayer and σ for both vesicles are consistent with the reported values in the liquid-crystalline phase [4, 13]. The κ of both systems coincide with each other within the error, indicating that C14 does not affect largely the bending elasticity in the liquid-crystalline phase compared to that in the gel phase.
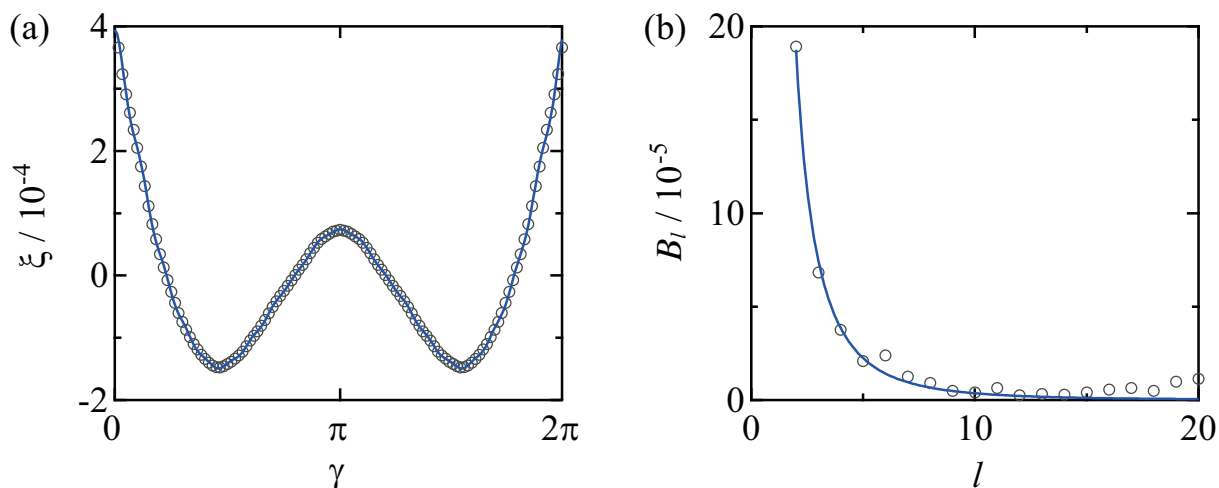
Fig. 3.12. (a) The angular autocorrelation function of the pure DPPC/tetradecane bilayer at 50 °C. Solid line is the fitting result to Eq. 3.19. (b) Amplitudes of Legendre polynomials obtained from (a). Solid line is the fitting result to Eq. 3.18.

As described in Sec. 3.1, the distance between the chains in the gel phase decreases with increasing C14 content because C14 aligns parallel to the lipid alkyl chains. In the liquid-crystalline phase, the short-range order of the alkyl chain is mostly lost, and the X-ray diffraction peak is only visible for that due to the stacking structure. The lipid membranes stack containing water in between the membranes both in the gel and liquid-crystalline phases. It has been reported that the stacking structure of DPPC bilayers remains almost unchanged upon the incorporation of n-alkanes in the liquid-crystalline phase [25]. The stacking period of membranes is widened by the Helfrich repulsion when the membranes are flexible, and their fluctuations are large [5]. If κ changes significantly, the Helfrich repulsion is affected and results in the change in the stacking period of membranes. Therefore, the observed effect of C14 on κ is consistent with that on the stacking structure.

It is widely known that, when the incorporation of C14 to DPPC or DMPC bilayers rises T_m with increasing C14 content [24, 25, 33]. Relative thermodynamic stabilities of two phases, that is, Gibbs energies, determine T_m of a membrane. The change in Gibbs energy caused by additive incorporation is, as described in Sec. 3.1, divided into two contributions; enthalpy change and entropy change. It has been revealed that enthalpy contributes 50 times larger than entropy to the T_m change caused by n-alkane incorporation by fitting a thermodynamic model to T_m of DMPC/n-alkane bilayers where n-alkanes are octane, decane, dodecane, and C14 [25]. Although the enthalpy change can occur in both phases, the small change in κ in the liquid-crystalline phase suggests that the enthalpy change mainly occurs in the gel phase due to closer packing of the alkyl chains.
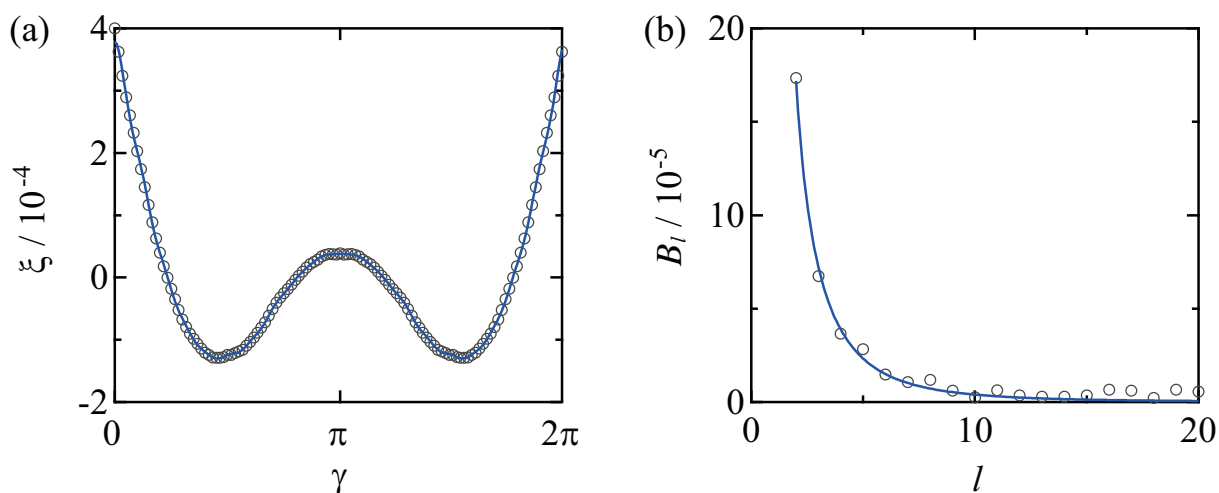
Fig. 3.13. (a) The angular autocorrelation function of the pure DPPC bilayer at 50 °C. Solid line is the fitting result to Eq. 3.19. (b) Amplitudes of Legendre polynomials obtained from (a). Solid line is the fitting result to Eq. 3.18.

3.2.5 Conclusion

In this section, the effects of C14 on the mechanical properties of DPPC bilayers were investigated using a phase-contrast microscope. κ did not exhibit a significant change upon the incorporation of C14 in the liquid-crystalline phase on the contrary to the gel phase, where κ becomes 10 times larger than that of the pure DPPC bilayer [24]. The result means that C14 gives a smaller influence in the liquid-crystalline phase than in the gel phase. This trend is the same as the effects of *n*-alkanes on other membrane properties of DPPC, such as the molecular packing, thermostability and stacking structure [24, 25], whereas opposed to the effects of a core-like molecule, cholesterol, which affects significantly in both phases and make the state in each phase closer. It has been clarified that C14, which is a representative of straight chainlike molecules, widen the gap in the mechanical property in the two phases in contrast to a core-like molecule.

3.3 Effects of *n*-Alkanes on the Dynamics of DPPC Bilayers

3.3.1 Introduction

Collective dynamics of lipid membranes in the mesoscopic scale is governed by the mechanical parameters and the microscopic structure of the bilayers [85–88]. These membrane properties are determined by the composition of lipids as well as the presence of other small molecules; however, the effects of additives on the dynamics are not well understood and not easily predicted. Typical collective dynamics in lipid bilayers are bending fluctuations and thickness fluctuations. Bending fluctuations have been observed using various methods such as microscopy and NSE. NSE results of bending fluctuations fit well to a model assuming fluctuation of a single membrane, proposed by Zilman and Granek [89]. However, in the measurement of headgroup-highlighted bilayers, Nagao *et al.* observed excess dynamics around the length scale of bilayer thickness, which is associated with thickness fluctuations [90]. Thickness fluctuations are related to mechanical properties such as κ, the area compressibility K_A of the bilayer, the coupling β of the two monolayers in the bilayer and the membrane viscosity η_m [91]. Although it is clarified that κ is not significantly changed by C14 incorporation in Sec. 3.2, new findings can be expected through a detailed investigation of membrane dynamics using NSE. Further, the effects of *n*-alkanes on the membrane dynamics may depend on the chain length as they did for other physicochemical properties of lipid bilayers.

In this section, we vary the *n*-alkane length to systematically investigate the effects of molecular additives on the dynamics of DPPC bilayers in the liquid-crystalline phase. The structural changes are also explored since internal dissipation affects membrane dynamics. We use SAXS and SANS techniques to characterize the bilayer structure with added *n*-alkane and explore the location of the *n*-alkane within the hydrophobic bilayer core. We characterize the membrane dynamics using NSE spectroscopy to measure both the collective bending and thickness fluctuations and determine κ and K_A [12].

3.3.2 Theory

NSE experiments directly measure the intermediate scattering function, $I(q,t)$ as a cosine Fourier transform of the scattering law, $S(q,\omega)$, where $q = 4\pi\sin\theta/\lambda$ is the magnitude of the scattering vector, 2θ and λ are the scattering angle and the wavelength of the incident neutron, ω is the exchanged energy and t is the Fourier time, that is a time associated with the exchanged energy ω. Zilman and Granek (ZG) [89] derived the expression for $I(q,t)$ to describe membrane fluctuations based on the

Helfrich model for bending energy [5],

$$\frac{I(q,t)}{I(q,0)} = \exp\left[-(\Gamma t)^{\frac{2}{3}}\right] \tag{3.20}$$

where Γ is the relaxation rate and follows a q^3 dependence, $\Gamma \propto q^3$. When protiated bilayers are subjected to measurements in D_2O by NSE, it is well documented that $I(q,t)$ follows the predicted scaling [92–94]. Watson and Brown [95] included the effects of the internal dissipation within the bilayer into the ZG formalism to better describe the dynamics observed on the nanoscale with NSE [10]. Nagao and colleagues proposed a relationship between Γ measured with NSE and the membrane bending modulus κ by incorporating these theoretical considerations as [12, 63],

$$\Gamma = 0.0069\sqrt{\frac{k_B T}{\kappa}}\frac{k_B T}{\eta}q^3 \tag{3.21}$$

where k_B is the thermal energy, T is thermodynamical temperature, and η is the viscosity of the solvent (D_2O). This expression allows us to determine the κ from the dynamics observed for the lipid bilayers with added n-alkanes.

When a bilayer bends, one monolayer experiences expansion while the other compressed. This mechanical relation is expressed in a thin elastic sheet model as,

$$\kappa = \frac{K_A}{\beta}d_c^2 \tag{3.22}$$

where K_A is the bilayer area compressibility modulus, β is a coupling constant between two mono-layers, and d_c is the hydrocarbon thickness of the bilayer. Experimentally, d_c can be obtained either from SAXS or SANS measurements, while K_A and β are not readily measurable for large unilamellar vesicles (LUVs).

Recently, K_A was estimated from NSE measurements of LUVs by taking advantage of contrast matching. These measurements require contrast matching the hydrophobic tails to the surrounding solvent and emphasizing the coherent dynamics of the lipid headgroups [8, 12, 96, 97]. At this contrast, $I(q,t)$ followed Eq. 3.20, while Γ shows a distinct deviation from the underlying q^3 dependence [90, 98, 99]. The "excess" dynamics was interpreted as the thickness fluctuations of the bilayers, and Γ was expressed by the superposition of the bending and thickness fluctuations [12] as,

$$\frac{\Gamma}{q^3} = 0.0069\sqrt{\frac{k_B T}{\kappa}}\frac{k_B T}{\eta} + \frac{(\tau_{TF}q_0^3)^{-1}}{1+(q-q_0)^2\xi^2}. \tag{3.23}$$

The first term is the same as Eq. 3.21, and originates from the membrane bending fluctuations, and the second term is a phenomenological expression for the thickness fluctuations, where q_0 is the peak position of the Lorentz function, τ_{TF} is the relaxation time of the thickness fluctuations, and ξ^{-1} is the half-width at the half maximum of the peak, respectively. The peak maximum of the excess dynamics, q_0, corresponds to the first minima in the bilayer form factor measured with SANS and is associated with the bilayer thickness.

Here, our focus is on the parameter ξ^{-1} which is related to the amplitude δd_c of the thickness fluctuations [12, 90, 97, 99–102]. The fractional change in the thickness can be defined as,

$$\sigma_d = \frac{\delta d_c}{d_c} = (q_0 \xi)^{-1}. \tag{3.24}$$

By statistical mechanics, K_A is related to the fractional change in area $\sigma_A = \Delta A / A$ as [103],

$$K_A = \frac{k_B T}{\sigma_A^2 A_0}, \tag{3.25}$$

where A and A_0 are the unit area of the membrane and the area per molecule, respectively. Assuming the volume compressibility is negligible, σ_A is equal to the fractional change in the thickness σ_d, i.e., $\sigma_A = \sigma_d = \delta d_c / d_c$ [103] . Therefore, the experimental $q_0 \xi$ relates to K_A as,

$$q_0 \xi = \sqrt{\frac{K_A A_0}{k_B T}} \propto \sqrt{K_A}. \tag{3.26}$$

Thus, the thickness fluctuation amplitude is related to K_A, allowing us to explore the effects of added n-alkanes on both κ and K_A as well as the coupling between the two moduli.

Another thickness fluctuation parameter τ_{TF} corresponds to the intrinsic membrane properties through a dispersion relation of the peristaltic mode (thickness fluctuations) proposed in the model by Bingham, Smye, and Olmsted [8]. The mode is damped by the viscosities of the solvent η and the bilayer η_m when its wavelength is shorter than the Saffman-Delbruck length $l_{SD} = \eta_m / \eta$ [104]. The damping is independent of the wavelength because the in-plane monolayer viscosity dominates. In general, τ_{TF} is expressed as [8]

$$\tau_{TF} \approx \frac{\eta_m}{K_A}. \tag{3.27}$$

3.3.3 Materials & Methods

Samples were prepared in the following steps. Protiated and tail-deuterated DPPC were purchased from Avanti Polar Lipids (Alabaster, AL). Protiated and deuterated n-alkanes (octane (C8), decane

(C10), dodecane (C12), tetradecane (C14)) were purchased from Sigma Aldrich (Darmstadt, Germany) and Cambridge Isotope Laboratories (Tewksbury, MA), respectively. D_2O was also purchased from Cambridge Isotope Laboratories. All the chemicals were used without further purification. Liquid n-alkane was added to DPPC powder at the molar ratio of DPPC : n-alkane = 6 : 4. The mixtures of DPPC and n-alkanes were dissolved in D_2O to give a lipid concentration of 100 mg/mL and sonicated for 3 h at 60 °C in an ultrasonic bath to ensure that the same n-alkanes ratio was incorporated in each system. Successful incorporation of n-alkanes was confirmed using differential scanning calorimetry (DSC) based on the absence of the thermal anomaly due to the melting of pure n-alkane and change in the phase transition temperature of DPPC, which depends on the incorporation ratio [24, 49]. After sonication, the samples were extruded through two stacked polycarbonate membranes with a nominal pore size of 100 nm using a heated Mini-Extruder and stored at 60 °C until the measurement.

Combinations of protiated and deuterated chemicals were chosen to get appropriate samples for each measurement. For SAXS experiments, fully protiated bilayers (protiated lipid and n-alkanes) were dispersed in H_2O. The contrast for X-ray scattering, which originates from the electron density (ED) profile, is shown in Fig. 3.14a. To more precisely locate the incorporated n-alkane in the bilayers, we used deuterated n-alkanes with protiated DPPC in D_2O. The scattering length density (SLD) profile for the neutron scattering at this contrast condition is shown in Fig. 3.14b. The bending fluctuations were observed using NSE by measuring fully protiated bilayers dispersed in D_2O with the corresponding SLD profile shown in Fig. 3.14c. The thickness fluctuations were captured by NSE using the headgroup-highlighted samples, where tail-deuterated DPPC and deuterated n-alkanes were used to contrast-match the hydrophobic region of the bilayer to the D_2O solvent. As shown in Fig. 3.14d, only the head groups are protiated and visible in the scattering experiment. Small amounts of protiated DPPC and n-alkanes were added to tail-deuterated DPPC and deuterated n-alkane to precisely match the SLD of the hydrophobic region with the carrier solvent, D_2O.

The samples with protiated DPPC (Fig. 3.14a,b,c) were subjected to measurements at 54 °C, while the samples with the tail-contrast-matched bilayers (Fig. 3.14d) were subjected to measurements at 50 °C. This is because mechanical properties of lipid membranes change as a function of the reduced temperature $T - T_m$ where T_m is the main transition temperature of the lipid bilayers [4], and T_m using tail-deuterated DPPC was found to be 4 °C lower than that using protiated DPPC [105].

DSC measurements were performed using a commercial apparatus (Q200, TA Instruments, New Castle, DE). To see thermal anomaly clearly, we used samples before extrusion, which contain multi-lamellar vesicles. Cooling and heating cycles were performed three times between 20 °C and 55 °C using a scan rate of 5 °C min^{-1} for the first ramp and 2 °C min^{-1} for the remaining ramps.
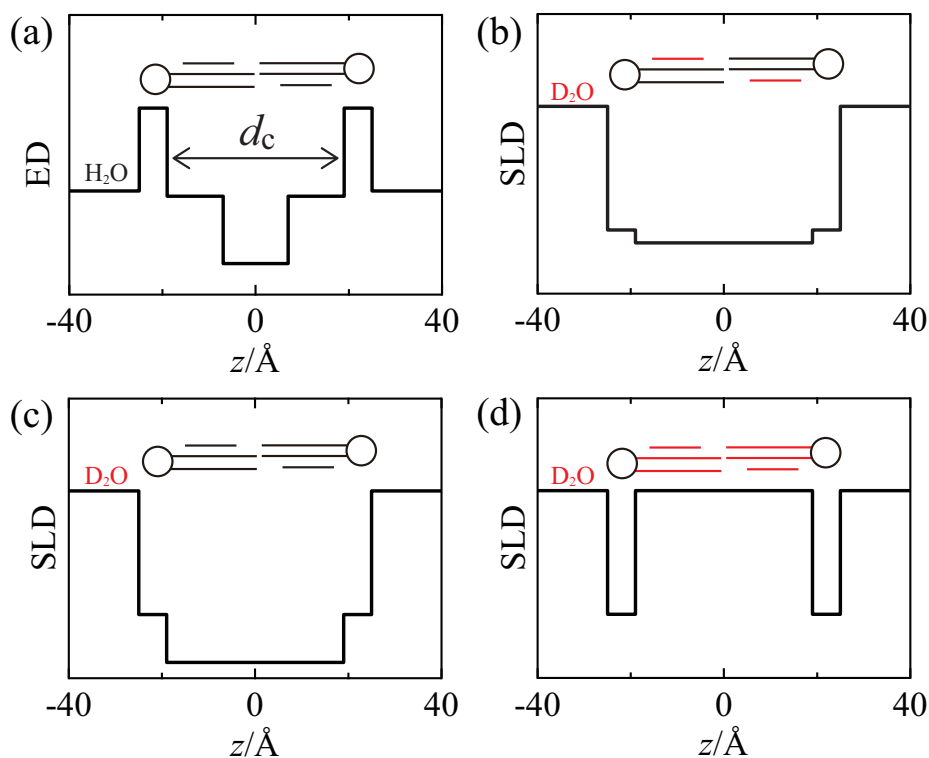
Fig. 3.14. Schematics of the scattering contrasts used to examine the structure and dynamics of the DPPC bilayers with added *n*-alkanes. Black portions of the molecule contain hydrogen atoms, while red parts are deuterated. (a) The electron density (ED) profile of fully protiated bilayers (protiated lipid and *n*-alkanes) in H$_2$O for SAXS measurements. (b) The scattering length density (SLD) profile of bilayers composed of protiated DPPC and deuterated *n*-alkanes in D$_2$O prepared for SANS. (c) The SLD profile of fully protiated bilayers in D$_2$O. (d) The SLD profile of the headgroup-highlighted bilayers (that is, the tail-contrast-matched samples) mainly composed of tail-deuterated lipid and deuterated *n*-alkanes in D$_2$O, which were used for NSE and SANS.

SAXS experiments were conducted on BL10C in the Photon Factory, KEK, Japan, where PILA-TUS 2M (DECTRIS Ltd., Baden, Switzerland) detector and an incident X-ray with a wavelength of 1.5 Å were used. The measured q range was 0.013 Å^{-1} to 0.83 Å^{-1} at a sample-to-detector distance of 1.1 m. The X-ray beam was monochromatized by the fixed-exit double crystal Si(111) monochro-mator (DCM, Kohzu Precision) [59]. All the samples were subjected to measurements at $T = 54\,°C$ in the liquid-crystalline phase.

SANS experiments were conducted on the NG7 30 mr SANS at the National Institute of Standards and Technology (NIST), USA [106, 107]. The incident neutron wavelength λ were 8.9 Å and 6.0 Å, and the covered q range was from 0.001 Å^{-1} to 0.5 Å^{-1}. The obtained two-dimensional SANS patterns were reduced to be on the absolute scale using a protocol developed at NIST [108].

NSE experiments were performed using the NGA-NSE spectrometer at NIST [109, 110]. The se-lected q range was from 0.03 Å^{-1} to 0.16 Å^{-1} with the use of 6 Å, 8 Å and 11 Å neutron wavelengths. Fourier times, t, spanned from 0.2 ns to 100 ns. The tail-contrasted-matched samples were subjected
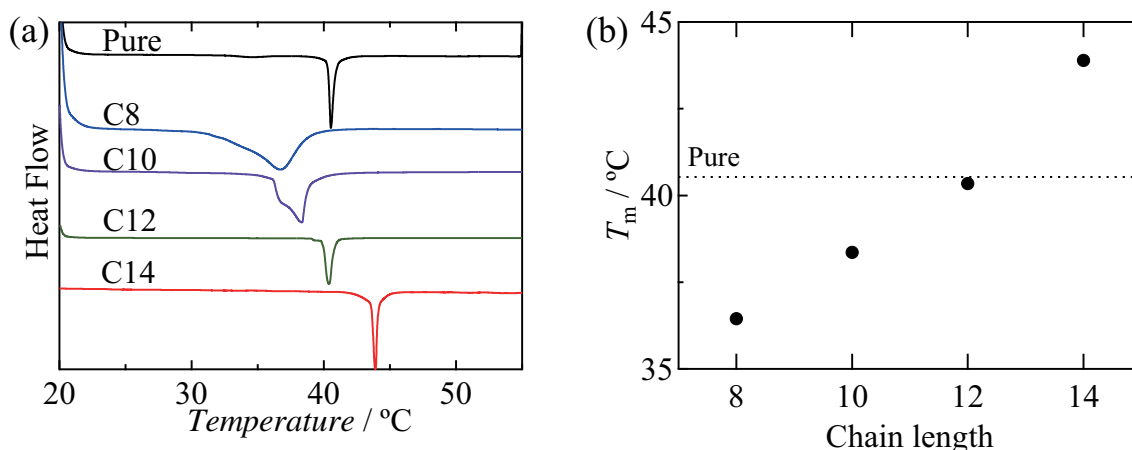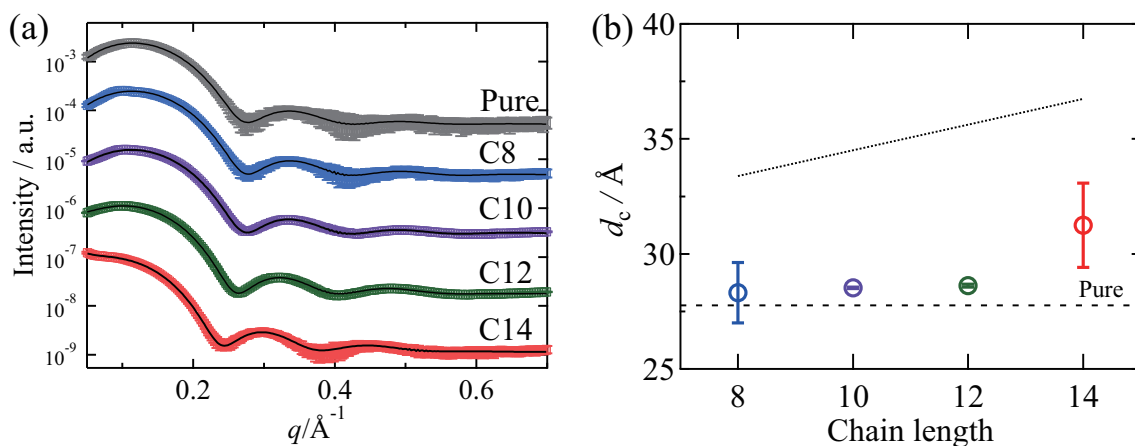
Fig. 3.15. (a) DSC traces of pure DPPC and DPPC/*n*-alkane (DPPC : *n*-alkane $= 6 : 4$ (mol : mol)) bilayers on the heating processes of the third cycle at a rate of $2\,°C\,min^{-1}$. (b) T_m determined from the peak temperatures of DSC traces in (a). Dotted line is T_m of the pure DPPC bilayer.

to measurements in a 4 mm thick cell at $50\,°C$ and the protiated samples in a 1 mm-thick cell at $54\,°C$. The obtained NSE signal was corrected for instrument resolution and solvent background to obtain the intermediate scattering function, $I(q,t)/I(q,0)$, using the software, DAVE [111].

3.3.4 Results & Discussion

As already discussed in literature, incorporating *n*-alkanes into lipid bilayers changes T_m. The enthalpic stabilization due to enhanced packing of alkyl chains in the gel phase causes the shifts in melting temperature [25]. In the present study, some of the thermal anomalies were broadened by the *n*-alkane incorporation, as shown in Fig. 3.7a, and it was difficult to determine the onset temperatures. Here we treat the peak temperatures as T_m. Figure 3.7b shows T_m of pure DPPC and DPPC/*n*-alkane (DPPC : *n*-alkane $= 6 : 4$ (mol : mol)) bilayers. For C8 and C10, the values of T_m are lower than that of pure DPPC, while T_m becomes higher than the pure for C14. For the present work, it is essential to understand the effects of *n*-alkanes on the phase transition temperature because the elastic properties are known to show anomalous at $T - T_m < 10\,°C$ [112, 113]. All the other measurements in this study were performed at temperatures in the range $T - T_m \geq 10\,°C$, as described in the section of the sample preparation. In the range of $T - T_m \geq 10\,°C$, the elastic properties still have gradual dependence on temperature [114]. It is necessary to consider the differences in reduced temperature when discussing the measured elastic moduli. However, the results for pure DPPC and C12 can be directly compared without competing for temperature effects since their T_m are almost the same.

The SAXS profiles of LUVs are shown in Fig. 3.16a. The bilayer form factor dominates the scattered intensity in the measured q range. The characteristic first hump at the lowest-q corresponds

Fig. 3.16. (a) SAXS profiles of pure DPPC and DPPC/n-alkane mixtures (DPPC : n-alkane $= 6 : 4$ (mol : mol)) bilayers obtained at 54 °C. Error bars represent ± 1 standard deviation, and the confidence intervals are 1.96 times of the error bars throughout the paper. Solid lines are fitting results. (b) d_c obtained by fitting to the SAXS profiles. Broken line, d_c of the pure DPPC bilayer; dotted lines, calculated d_c assuming that all the incorporated n-alkane locates in the central plane of the bilayers.

to the main peak originated from the bilayer form factor followed by oscillatory scattering as q gets large. The dip location in the scattering profile relates to the bilayer thickness. The dip in the range of $0.2 \, \text{Å}^{-1} < q < 0.3 \, \text{Å}^{-1}$ shifts to lower q as the chain length of n-alkane increases, which indicates an increase in the bilayer thickness.

To quantify the changes in bilayer thickness with n-alkane length, we used a model of a core and five-shells [115], as schematically shown in Fig. 3.14a, to fit the SAXS profiles. In the model, the lipid bilayer is represented by five shells that are each characterized by a thickness and electron density, and the total thickness of the three central shells is taken as d_c, the bilayer hydrocarbon thickness. The polydispersity was included in the core radius (radius of a vesicle) and the thickness of the central shell. The obtained d_c increased with increasing the n-alkane length, as shown in Fig. 3.16b, which is consistent with the shift in peak position to lower q.

The increase of the bilayer thickness, though, seems not significant. The incorporated n-alkanes can align parallel to the lipid alkyl chain or locate in the center of the bilayer. The parallel alignment is observed in many cases for the addition of small organic molecules such as cholesterol, n-alkanes, and n-alkane derivatives [21, 25, 27, 116]. Assuming the incorporated all of the n-alkanes are condensed at the central part of the bilayer, and neither the area per lipid nor the specific volume of ingredients is affected, the dotted line shows the expected change in bilayer thickness in Fig. 3.16b. All of the experimentally measured d_c are smaller than these calculated values. The smaller experimental d_c compared to the calculated values suggests that most n-alkanes align parallel to the acyl chains of the lipids. Further, it is possible that either the area per molecule or the specific volume of the ingredients changes by the n-alkane incorporation. Unfortunately, we could not determine the specific volume

in the present study, though literature suggests that the area per lipid does not change significantly when the *n*-alkanes are absorbed into the center of the bilayer [117, 118]. Compared to the other *n*-alkanes studied, the addition of C14 leads to the greatest increase in d_c, and the measured value is closest to the calculated value. The significant increase in thickness for C14 suggests that around 30 % the *n*-alkane is expected to distribute within the center plane of the membrane. The changes in bilayer structures with the other *n*-alkanes are much smaller, and additional experiments were needed to determine where they locate within the bilayer.

To clarify the *n*-alkane location in the cases for C8, C10, and C12, we performed SANS experiments with the pure protiated DPPC bilayer and deuterated *n*-alkanes in D_2O. The SLD profile for this mixture is expected, as shown in Fig. 3.17b. Depending on the location of *n*-alkane, the scattering pattern should change significantly, and we may qualitatively discuss the location of the molecules. Figure 3.17a shows SANS profiles for pure, C8, C10, and C12 incorporated bilayers. In the cases of the pure DPPC bilayer and the DPPC/C8 bilayer, the SANS profiles are flat around 0.2 $Å^{-1}$, but there is a hump in the cases of DPPC with C12 and C10. As schematically depicted in Fig. 3.17b, localization of *n*-alkanes at the central part of the bilayer can significantly change the SLD profile. Therefore, the hump for C10 and C12 arises from the localization of the incorporated *n*-alkanes at the center of bilayers. Figure 3.17a also shows results of fit with solid and broken lines for the different SLD conditions. The dashed line shows the profile for the parallel configurations for the incorporated *n*-alkanes, while the solid lines represent the case a part of *n*-alkane locates in the central plane of the bilayer. In these fitting, we fixed the parameters other than the scattering length densities of the leaflets. In the pure DPPC and DPPC/C8 bilayer, the broken lines fit the SANS profile better than the solid lines, indicating the structureless scattering density in the hydrophobic region. It is reasonable for the pure DPPC bilayer since the hydrophobic region consists of only protiated chains. The fitting result indicates that the deuterated C8 molecules are located parallel to the lipid alkyl tails in the bilayer. The expected location is consistent with the small increase in thickness measured with SAXS. On the other hand, the SANS data for added C10 and C12 were approximated better by the solid lines, suggesting that a part of *n*-alkane distributes in the central plane of bilayers. Figure 3.17c shows results of fit when the *n*-decane aligns parallel to the lipid molecules and locate at the center as shown in Fig. 3.17d. The model does not fit well to the SANS profile implying that there are little *n*-decanes aligning parallel to the lipids in the bilayer center. C14 molecules are expected to locate in the lipid molecules in the central plane considering the significant increase in d_c in DPPC/C14 bilayers and the chain length dependence that other physicochemical parameters exhibit [24, 25, 33, 119].

This trend with the *n*-alkane length is opposite to the previous report, in which shorter chain *n*-
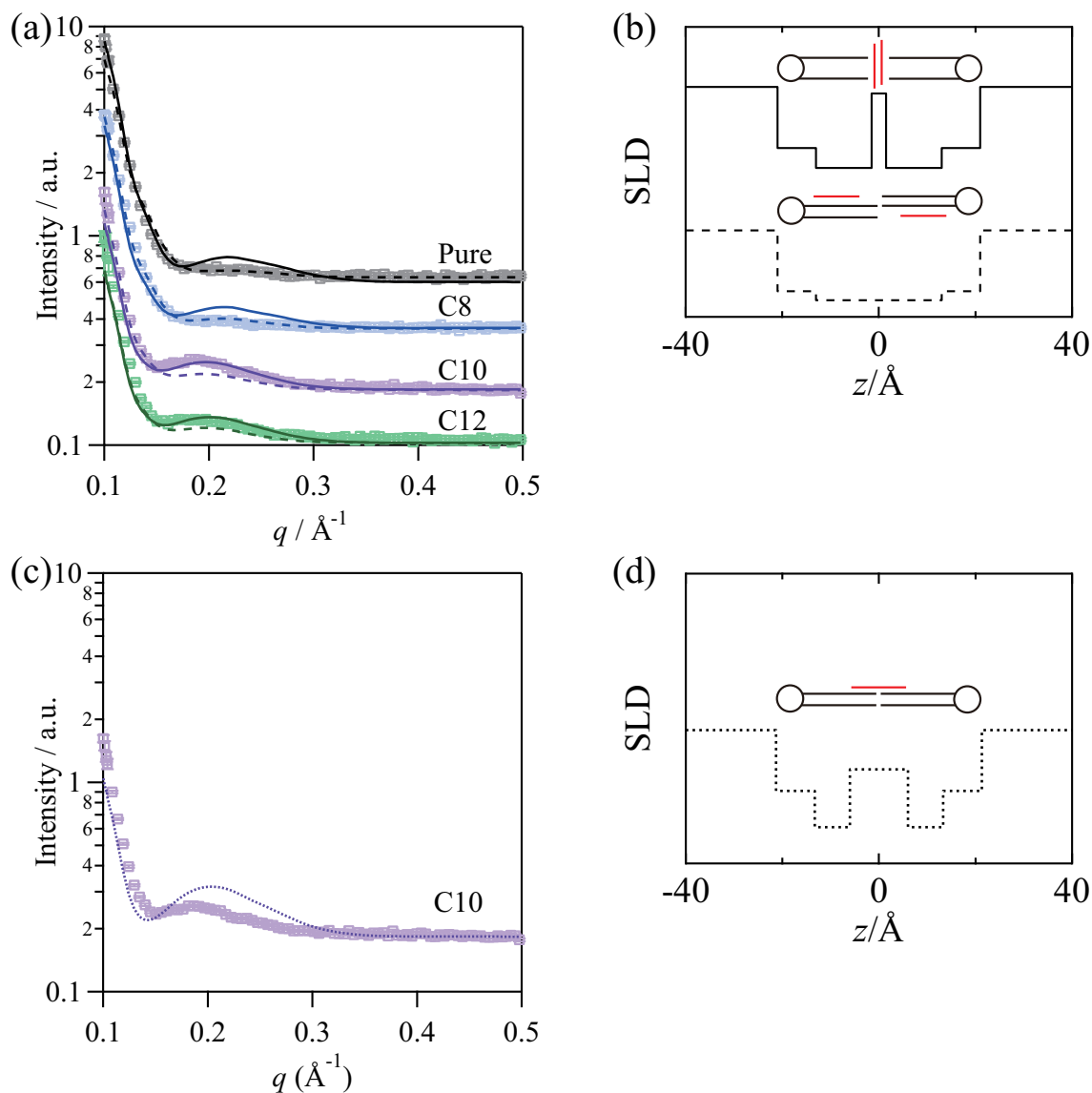
Fig. 3.17. (a) SANS profiles of DPPC and (protiated DPPC) : (deuterated *n*-alkane) = 6 : 4 (mol) bilayers obtained at 54 °C. Error bars represent ±1 standard deviation and are smaller than the plots. Solid and broken lines show the models at the top and bottom in (b), respectively. (b) Schematics of the contrast of bilayers consisting of protiated DPPC and deuterated *n*-alkanes (red) in D_2O prepared for SANS. Top, the contrast when deuterated *n*-alkanes locate in the midsurface; bottom, the contrast in the case for parallel alignment of deuterated *n*-alkanes. (c) SANS profiles of (protiated DPPC) : (deuterated *n*-decane) = 6 : 4 (mol) bilayers obtained at 54 °C. Dotted line shows the model in (d). (d) Schematics of the contrast of bilayers consisting of protiated DPPC and deuterated *n*-decane in D_2O when deuterated *n*-decanes align parallel to the lipid in the middle surface of bilayers.

alkanes caused a more significant increase in the bilayer thickness. One potential difference between the results by McIntosh and the present systems is the amount of incorporated n-alkane. Since McIntosh *et al.* saturated the lipid bilayer with n-alkane, the incorporated amount would differ depending on the n-alkane length. Work by Gruen and Haydon [120] suggested that the location of the n-alkane within the bilayer also depends on the volume fraction: n-alkane molecules distribute throughout the bilayer at low concentrations, and the distribution at the center of the bilayer plane also increases as the volume fraction increases. This behavior agrees with our experimental results, where we kept the mole fraction of n-alkane constant, leading to the volume fraction of 0.19, 0.22, 0.25 and 0.28 for C8, C10, C12, and C14, respectively. Thus, one possibility is that McIntosh realized a larger volume fraction for shorter n-alkanes than longer n-alkanes.

Note that the present results are for bilayers of the liquid-crystalline phase. On the other hand, the results in Sec. 3.1 is focused on the gel phase DPPC, where the n-alkane aligned parallel to the lipid alkyl chains due to the enthalpic gain [25]. The parallel alignment in the gel phase appears as the decrease in the lattice constant of the lipid alkyl chain with increasing the incorporation of n-alkanes and also shows a chain length dependence [24, 25, 27]. The present results suggest that the location of the n-alkane within a membrane differs depending on the lipid phase state and whether the lipid is in the gel or liquid-crystalline phases.

The SAXS and SANS results have revealed the structural change induced by the incorporation of straight chain molecules with different lengths. It has been clarified that, with increasing the alkane length, d_c increases due to an increased amount of n-alkanes that locate in the central plane of bilayers. Previous researches reported the structural changes upon n-alkane incorporation in the gel phase. On the other hand, this study clarified that in the liquid-crystalline phase. The structural changes should influence the membrane dynamics since the bending and thickness fluctuations are controlled by the internal dissipation that is affected by the internal structure of a membrane. We expect that the membrane dynamics also depends on the n-alkane length as the structural changes do upon the n-alkane incorporation.

Figure 3.18a shows the measured $I(q,t)/I(q,0)$ for the fully protiated DPPC/C8 bilayers. The C8 data in the figure and all other samples studied here are well fit by the ZG theory (Eq. 3.20). These fits suggest that the dynamics captured for the n-alkane incorporated bilayers follow the same single membrane undulation model used to describe pure lipid bilayers. This result is evident in the q-dependence of Γ estimated from the $I(q,t)$. Figure 3.18b shows the decay constant Γ extracted from the $I(q,t)/I(q,0)$, which show a q^3 dependence for all of the lipid : n-alkane mixtures. We used Eq. 3.21 to estimate the value of κ, and the fit results are depicted in Fig. 3.18b by solid lines.
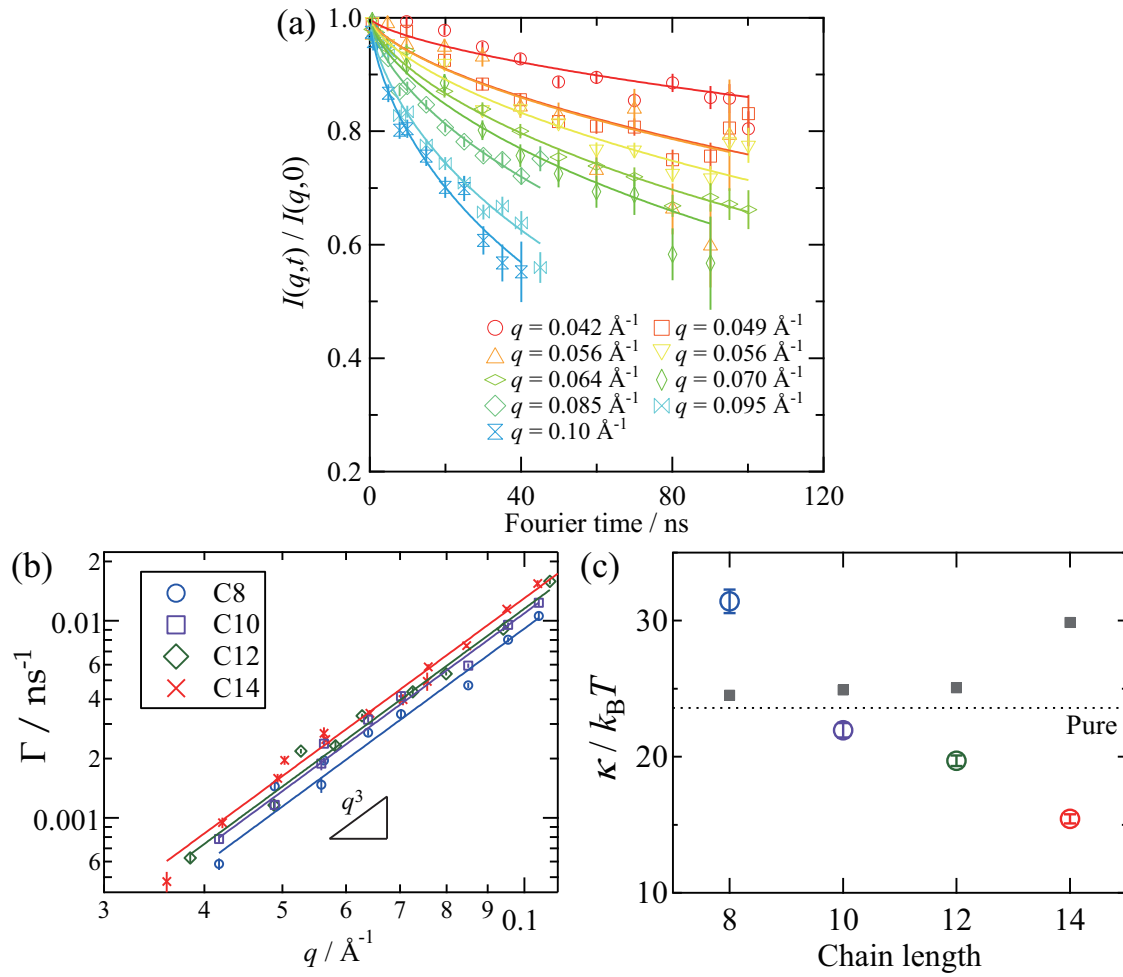
Fig. 3.18. (a) Intermediate scattering function $I(q,t)/I(q,0)$ of the fully protiated DPPC: C8 (6 : 4 mol) bilayers measured by NSE at 54 °C. The solid lines are the fits by Eq. 3.20. (b) The q dependence of Γ for the fully protiated samples (DPPC : n-alkane = 6 : 4 (mol : mol)) measured at 54 °C. The solid lines are the fitting results to Eq. 3.21. (c) Circles, experimentally determined κ from fits to the NSE data at 54 °C; squares, calculated κ from Eq. 3.22 based on the measured change in bilayer thickness and assuming that K_A and β are constant and equal to the values for pure DPPC.

The extracted bending modulus κ values are plotted in Fig. 3.18c. The bending modulus for C8 incorporated bilayers is larger than that of the pure DPPC, while κ decreases with increasing n-alkane length such that C12 and C14 bilayers are softer than pure DPPC although κ was reported to be almost the same as that of pure DPPC bilayer in Sec. 3.2. The softening of the bilayer with added n-alkane is unexpected based on the measured increase in bilayer thickness. As we showed in the structure section, the bilayer thickness is larger when n-alkane is incorporated, and it gets larger as we increase the chain length of n-alkanes. Eq. 3.22 predicts a quadratic increase of κ with increasing d_c. When we calculate the values of κ using the experimentally measured d_c values and assume the constant K_A and β in Eq. 3.22, we expect the values of κ follows the gray squares in Fig. 3.18c. In other words, if the changes in κ were due solely to the changes in a bilayer structure, then κ for the C12 and C14 bilayers would increase compared to pure DPPC. Consequently, our results suggest the following that either K_A or β (or both) are changing and leading to a decrease in κ upon n-alkane incorporation.

As suggested in the phase behavior section, another potential source of the change in κ is the differences in relative temperature. It is known that the values of κ in the gel phase are about an order of magnitude larger than the values in the fluid phase [3, 97, 98], and that κ decreases further with increasing T above T_m. However, our measurements of T_m indicate that T_m increases as the chain length of n-alkane increases. Therefore, the longer n-alkanes are closer to T_m and should have a larger value of κ. As this is not the case for our experimental results, the change of T_m with the chain length of n-alkane cannot explain the changes in κ.

As we described in the Theory section, K_A determines the thickness fluctuation amplitude. Thus by measuring the thickness fluctuations with NSE, we can estimate the effects of adding n-alkanes on K_A. Besides, we can obtain information about the effects of straight chainlike molecules on the thickness fluctuations. Figure 3.19a shows the $I(q,t)/I(q,0)$ measured for tail-deuterated-DPPC/deuterated-C10 bilayer, with which the scattering length density of the hydrophobic region matched to D_2O. The decay was well fit to Eq. 3.20. Fitting of the $I(q,t)/I(q,0)$ for the other tail-deuterated-DPPC/deuterated-n-alkane systems were successful in the same way. The resultant Γ are shown in Fig. 3.19b. If the dynamics are solely coming from the membrane height (bending) undulations, Γ/q^3 should be a constant with q. A deviation from the q^3 scaling is evident for pure DPPC and DPPC/n-alkane systems except for C8. The excess peak is around $q_0 = 0.07$ Å^{-1} and moves to lower q as the n-alkane length increases. The peak shift reflects the increase in the bilayer thickness with n-alkane elongation observed with SAXS and SANS. In the case of C8, however, possible reasons for missing "excess" signal are the broadening of the peak (increase in ξ^{-1}) and/or the weakening of the peak intensity (increase in τ_{TF}). The average value of Γ/q^3 for the tail-contrast-matched DPPC/C8 bilayers is 13
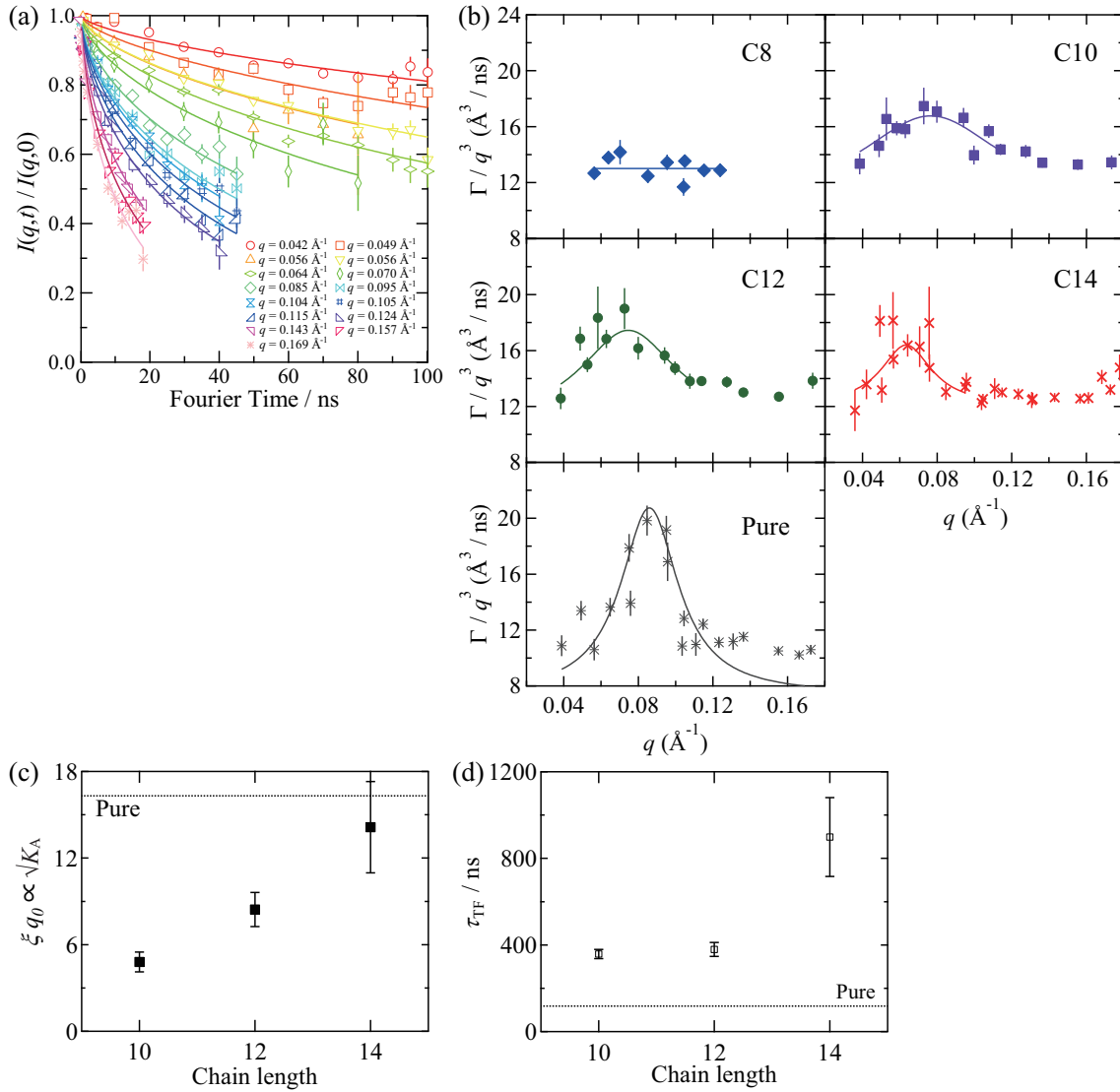
Fig. 3.19. (a) Intermediate scattering function $I(q,t)/I(q,0)$ of the tail-contrast-matched DPPC/C10 (6/4 mol) bilayers measured by NSE at 50 °C. The solid lines are the fits to Eq.3.20. (b) The q dependence of Γ/q^3 for the headgroup-highlighted samples (DPPC : n-alkane = 6 : 4 (mol : mol)) measured at 50 °C. The solid lines are fitting results of Eq. 3.23. The broken line shows Γ/q^3 value assuming that the data for C8 is constant. Black, the case of the pure DPPC bilayers [12]. (c) ξq_0 and (d) tau_{TF} of the n-alkane incorporated DPPC bilayers at 50 °C. The dotted lines shows the values in the case of the pure DPPC bilayer.

$\text{Å}^3/\text{ns}^{-1}$, while it is $9 \text{ Å}^3/\text{ns}^{-1}$ for the fully protiated bilayers. This difference indicates that the width (ξ^{-1}) of the peak was broadened upon the incorporation of C8. However, we could not quantify how broad the peak would be from the present data.

Eq.3.23 was employed to fit Γ/q^3 in Fig. 3.19b for the present data except for C8 where q_0 and κ are fixed based on the measured SANS of the tail-contrast-matched samples (data not shown) and NSE from the fully protiated samples (See Fig. 3.18c), respectively. Also, we applied the instrumental q resolution estimated using the pure DPPC data to the other data sets by following the method applied before [12]. Thus, the only fit parameters are τ_{TF} and ξ.

Figure 3.19c shows the fit results for ξq_0, which is proportional to the inverse of the thickness fluctuation amplitude. As the value of ξq_0 is smaller for the DPPC/n-alkane mixtures than pure DPPC, the n-alkane incorporated bilayers have a larger amplitude of thickness fluctuation. This trend indicates that the n-alkane incorporated bilayers are, in general, more compressible than the pure DPPC bilayers.

The ξq_0 increases with increasing n-alkane length from C10 to C14, suggesting K_{A} increases per Eq. 3.26. Fluctuation data shows that the trend in K_{A} is opposite to the trend in κ, i.e., the membrane is less compressible, yet more flexible with increasing d_{c}. These trends in moduli are only possible if β also increases (Eq. 3.22), and the leaflets are less coupled with added n-alkane. Namely, the data suggest that DPPC/n-alkane membranes behave more like two uncoupled leaflets than the pure DPPC bilayer.

The structural data provide additional insights into the n-alkane effects on the membrane dynamics. The structural data shows that a part of C12 and C14 n-alkanes also locates in the center of the bilayer, physically separating the two DPPC leaflets. The structure may suggest that decreasing interactions between leaflets will also affect the dynamics. The data presented here for n-alkanes show similar behavior to a previous work [121], where the addition of HIV-fusion peptide also increased β. Together these results suggest that decreasing the interactions between the bilayer leaflets will impact the membrane dynamics and point to an additional mechanism through which additives can influence the membrane properties.

The relaxation time, τ_{TF}, becomes larger than that of the pure DPPC bilayer, indicating the slowing down of the thickness fluctuations by alkanes, as shown in Fig. 3.19d. In the case of C14, the enhancement of τ_{TF} is significant. The increases in τ_{TF} and K_A in 3.27 indicate an increase in η_{m}. The increase means that the membrane becomes more viscous. Strangely, the bilayer becomes more viscous despite interleaflet decoupling shown by the increase in β. Viscosities of incorporated alkanes also do not account for the change in τ_{TF} since alkane viscosity linearly increases with its length [122].

A possible explanation for this is a change in the Saffman-Delbruck (SD) length $l_{SD} = \eta_m/\eta$ [104]. The mode with a long wavelength, $q_x l_{SD} \ll 1$ where q_x is wavenumber, is dissipated by the solvent viscosity, whereas the short-wavelength mode, $q_x l_{SD} \gg 1$, by the membrane viscosity. Another possibility is that incorporation of n-alkanes to the membrane can increase the wavelength of the thickness fluctuation beyond the SD length, which means that the simple assumption of Eq. 3.27 does not hold. In this case, τ_{TF} is expressed as;

$$\tau_{TF} = \frac{\eta_m}{K_A} + \frac{2\eta}{q_x K_A} \tag{3.28}$$

When q_x gets smaller, the second term of the equation is not negligible. A drastic change in τ_{TF} compared to C10 and C12 implies a huge change in the wavelength in the case of C14. Membrane viscosity is estimated from dissipated energy, and the molecular origin of the viscosity is difficult to determine. Lipid bilayers are highly anisotropic, and the viscosity should be different from that in the three-dimensional fluid. However, the membrane viscosity is expected to originate in friction between molecules in the bilayers. With this premise, the increase in η_m cannot be explained while considering the decoupling of the two monolayers caused by the incorporation of longer n-alkanes. The simulational study also showed that the surface shear viscosity hardly varies with the interleaflet coupling [123]. Apart from the molecular friction, the increase in η_m cannot be explained by an assumption that thickness easily relaxes with alkanes in the central plane of the bilayer.

3.3.5 Conclusion

In this section, we examined the effects of C8, C10, C12, and C14 on the dynamics of DPPC bilayers in the liquid-crystalline phase. The present results for n-alkanes suggest that the effects depend on where the additive locates in the membrane. SAXS and SANS results indicated that, with increasing n-alkane length, increases were observed in d_c and in the population of n-alkanes that distribute in the central plane of the bilayer. Through the analysis of bending fluctuation data, it is clarified that κ becomes lower on the elongation of the added n-alkanes. The thickness fluctuation data shows that the amplitude and τ_{TF} increase upon the n-alkane incorporation. Combining measurements of the bending and thickness fluctuations suggests that the coupling between the leaflets in a bilayer is weakened with added n-alkanes. Due to this decoupling, the bilayer becomes easier to bend despite being thicker. The decrease in coupling seems to be correlated to the n-alkane location in the membrane, suggesting that decreasing the physical interactions between the leaflets decreases the coupling. This relation is the correlation between the microscopic changes and the mesoscale dynamical changes induced by the n-alkane incorporation.

The present results emphasize that adding straight chainlike molecules brings the length-dependent effects on the membrane dynamics and the structure in the liquid-crystalline phase as well as on the structure in the gel phase, and the phase behavior. It has been revealed that the additives that are similar to the major component have significant effects on the physicochemical and mechanical properties in lipid bilayer systems. Further, the incorporation effects of straight chainlike molecules depend on their lengths, which is one of the structural features of additives.

Chapter 4

# Effects of Molecules Having a Core and a Straight Chain on DPPC Membrane Properties

In this chapter, the incorporated additives have a core part and a straight alkyl chain. A homologous series of liquid crystals is chosen, and the shape of the additive was varied from similar to different one compared to straight alkyl chains by reducing the length of an alkyl chain attached to the biphenyl core.

4.0.1   Introduction

When straight chainlike molecules are added to DPPC bilayers, significant influences are observed on the structure, phase behavior and dynamics in the gel and liquid-crystalline phases. In this section, we explore the effects of additives which have a core and an alkyl chain. A representative biomolecule with a different shape is cholesterol, which is a core-like molecule and has been a subject of intensive study concerning the effects on lipid bilayer properties thus far. It has been known that cholesterol and straight chainlike molecules have opposing effects, as described in Chapter 1. Consequently, we can imagine that a core and a chain have competing effects even when they coexist in a single molecule while assuming that the incorporation effect is merely additive. To clarify this issue, we need to choose a series of suitable molecules other than sterols or steroids because the precise control of their molecular structure is hard.

Thus, we herein investigate the effects of 4-n-alkyl-4$'$-cyanobiphenyl (nCB, n being the number of carbon atoms in the alkyl chain, Fig. 4.1) on the phase behavior of the phospholipid bilayer.

*n*CB molecules are composed of a cyanobiphenyl core and an alkyl chain of different length *n*. This molecular structure enables us to discuss the effects of both the core and the alkyl chain within a single molecule. Indeed, the *n*CBs are a typical mesogenic (liquid-crystalline) series of compounds [124,125], in which the core and the flexible chain play intrinsic and different roles upon the formation of various liquid-crystalline phases. [42, 126–129]
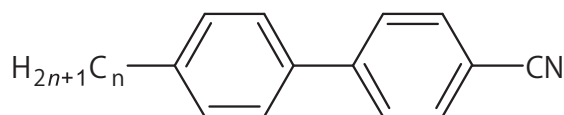
Fig. 4.1. Chemical structures of *n*CB.

4.0.2   Materials & Methods

DPPC was purchased from Wako Pure Chemical Industries, Ltd. (Osaka, Japan). *n*CBs where $n = 0, 2, 3, 4, 7, 8$ were also purchased from Wako Pure Chemical Industries, Ltd., while the *n*CBs where $n = 1, 5$ were obtained from Tokyo Chemical Industry Co., Ltd. (Tokyo, Japan), and that where $n = 6$ was purchased from Frinton Laboratories Inc. (Hainesport, NJ, USA). Finally, tetradecane (C14) was obtained from Wako Pure Chemical Industries, Ltd. (Osaka, Japan). All compounds were used as received without further purification.

DPPC and the desired *n*CB were dissolved separately in solutions of chloroform and methanol (2:1 v/v) to give concentrations of 100 mM and 12 mM, respectively. The resulting two solutions were then mixed at the desired DPPC to *n*CB molar ratio (denoted in mol% in the DPPC/*n*CB mixture), and the solvents were evaporated in an oven at 110 °C over 20 min. The various DPPC/*n*CB mixtures were placed under vacuum for a minimum of 12 h, and the resulting dry films were hydrated using ultra-pure water (MilliQ, 18.2 MΩ cm). For small-angle X-ray scattering (SAXS) and differential scanning calorimetry (DSC), the combined concentrations of DPPC/*n*CB in water were 50 and 100 mM, respectively. These dispersions were then sonicated for 3 h at 50 °C in an ultrasonic bath (US-101 from SND Co., Ltd (Nagano, Japan)), during which time, the dispersions were stirred occasionally using a vortex mixer (SI-0286, Scientific Industries Inc. New York, USA). The samples required for X-ray experiments were further sonicated using an ultrasonic homogenizer (UH-50, SMT Co., Ltd (Tokyo, Japan)) until the solutions became mostly transparent. The resulting DPPC/*n*CB vesicles were expected to form a unilamellar structure through this procedure. All measurements were carried out within a couple of days of sample preparation. For comparison, a dispersion of DPPC containing

12 mol% C14 was also prepared. In this case, tetradecane was added to the DPPC powder, and the resulting powder was hydrated using ultrapure water.

Experiments of SAXS and WAXS were carried out at BL10C, Photon Factory, KEK, Japan [59]. PILATUS3 2M and PILATUS3 200K (DECTRIS Ltd., Baden, Switzerland) detectors were employed for SAXS and WAXS measurements, respectively. X-ray wavelength was monochromatized to 1.488 Å by the fixed-exit double crystal Si(111) monochromator (DCM, Kohzu Precision). All measurements were performed at 25 °C in the gel phase and 55 °C in the liquid-crystalline phase.

DSC measurements were performed using a commercial apparatus (Q200, TA Instruments, New Castle, DE). Each sample pan was heated at 65 °C for 3 min using a hot stage (CB-100A, As One Co., Osaka, Japan) and subsequently placed at room temperature (about 20 °C) for 3 min. This heating/cooling cycle was repeated five times to yield a thermally stable sample before recording the DSC traces. In the DSC measurements, cooling/heating cycles were performed three times between 20 and 55 °C at a scan rate of 2 °C min^{-1}. The transition temperatures were determined from the thermal anomaly in the third heating process after confirming that the second and the third cycles gave comparable traces. Determination of the true transition temperatures was problematic due to the broadening of the thermal anomaly through phase separation of the binary mixture during the transition. The middle point between the onset and the peak of the anomaly was adopted as the "transition temperature," where the Gibbs energies of the two phases are considered being equal without phase separation.

4.0.3   Results & Discussion

The all nCB must be similarly incorporated in DPPC bilayers to discuss the effect of the balance between the core part and the alkyl chain of the nCBs. The knowledge of the incorporation manner is also valuable for the comparison of the effects of nCB with other molecules such as cholesterol or alkanes, which mostly lie parallel to the lipid alkyl chains in the bilayers [52, 130]. Structural changes of the bilayer caused by the addition of nCB were studied using X-ray scattering experiments with a nCB content of 12 mol% (88 mol% of DPPC), as the complete incorporation of 12 mol% nCB was confirmed by DSC for all n, as discussed later. The SAXS profiles of the DPPC/nCB unilamellar vesicles (Fig. 4.2) were obtained by subtracting the SAXS profile of the background (pure water). The subtraction successfully removed the diffraction peak at approximately $q = 0.4$ Å^{-1}, corresponding to the polyimide window [131] of the sample cell. The resultant SAXS profiles of pure DPPC and DPPC/nCB at 55 °C are comparable, and these fringe patterns appear to support the form factor of a bilayer [132].
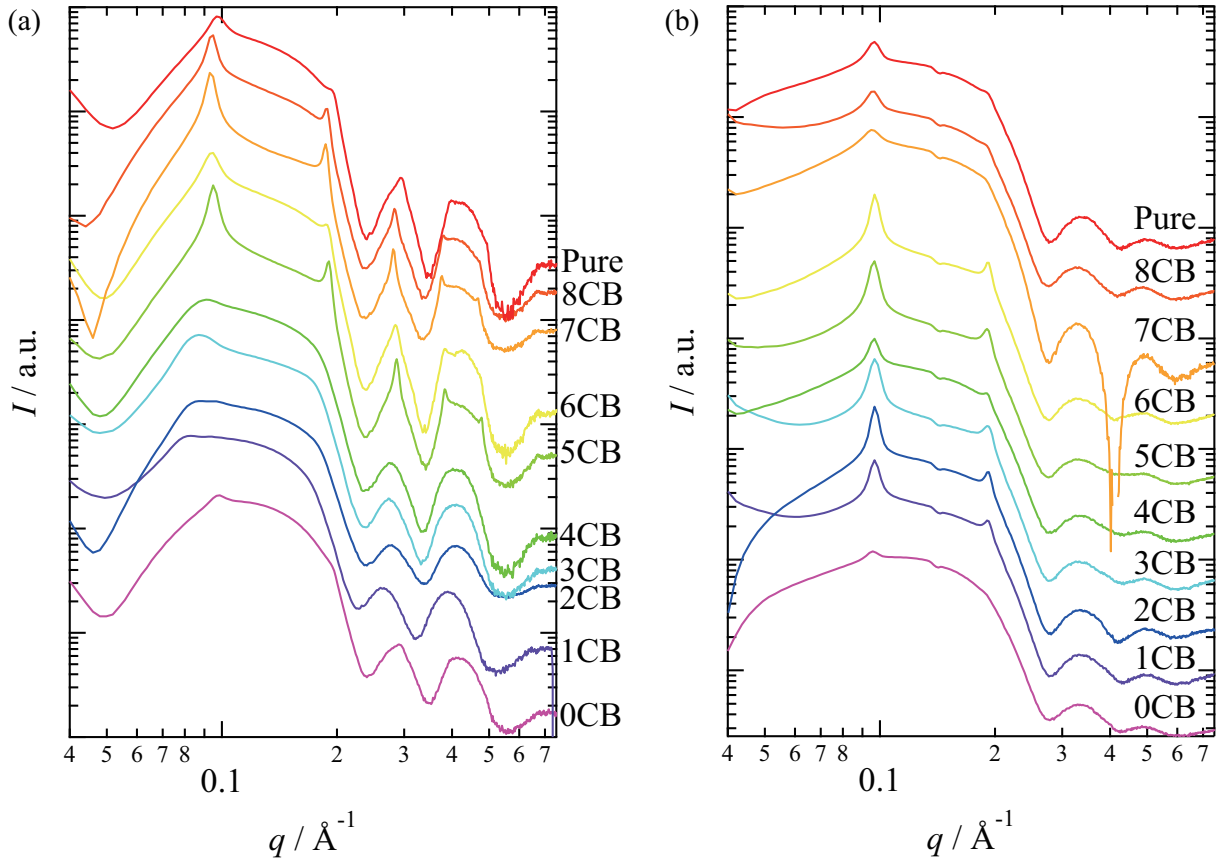
Fig. 4.2. SAXS profiles of unilamellar vesicles of pure DPPC and DPPC containing 12mol% of nCB at (a) 25 °C and (b) 55 °C. Background (water) subtracted.

The fringe patterns were analyzed to determine the incorporation manner of nCB molecules in the bilayer. The measured scattering intensity $I(q)$ is dependent on the structure factor $S(q)$ as outlined in the following equation:

$$I(q) = S(q)F(q)^2, \tag{4.1}$$

where q is the scattering vector ($q = 4\pi \sin\theta/\lambda$), and $F(q)$ is the form factor. Although Bragg reflections from multilamellar vesicles were discernible in some samples, these reflections were rather weak compared to the form factor. We assumed the Bragg reflections were accordingly negligible and so $S(q) \approx 1$. Then, the electron density profiles of the lipid bilayer were estimated by the functional fitting for the form factor obtained from SAXS [132] while assuming that the electron density was approximated by three Gaussians, which represent two headgroups and a hydrophobic region, as

determined from the equation below [132]:

$$\rho(z) = \bar{\rho}_H \left[\exp\left(-\frac{(z-z_H)^2}{2\sigma_H^2} \right) + \exp\left(-\frac{(z-z_C)^2}{2\sigma_H^2} \right) \right]$$
$$+ \bar{\rho}_C \exp\left(-\frac{z^2}{2\sigma_C^2} \right) + \rho_{H_2O} \tag{4.2}$$

where z is the distance along the normal to the bilayer from its center. The amplitude and width of each Gaussian are denoted as ρ and σ, respectively. Subscripts H and C indicate the headgroups and the hydrophobic chain, respectively. $I(q)$ can then be calculated using the Fourier transform of Eq. 4.2 as follows [132]:

$$I(q) \approx F(q)^2 + I_{bg}$$
$$\propto \frac{1}{q^2} \left[\sigma_H \bar{\rho}_H \exp\left(-\frac{\sigma_H^2 q^2}{2} \right) \cos(qz_H) \right.$$
$$\left. + \sigma_C \bar{\rho}_C \exp\left(-\frac{\sigma_C^2 q^2}{2} \right) \right]^2 + I_{bg}, \tag{4.3}$$

where I_{bg} is the background intensity. By fitting the SAXS profiles using Eq. 4.3 (Figs. 4.3, 4.4), the electron density profile of the bilayers could be estimated. The profiles for the pure DPPC and the DPPC/nCB bilayers at 25 °C are given in Fig. 4.5, where the peak areas of the headgroup regions were normalized to that of the pure DPPC bilayer for comparison. Note that only the relative variation in ρ is meaningful. Since the negative peak areas of the hydrophobic regions are smaller than that of the pure DPPC bilayer in all cases, it is concluded that the electron densities of the alkyl groups increased upon the addition of nCB. Note that the normalization considering the reduced headgroup contents further weakens the negative peak of the hydrophobic region. In addition, Fig. 4.6 shows the thicknesses of the bilayers $2z_H$ with respect to n. The thicknesses were nearly constant in both the gel and in the liquid-crystalline phases and favorably compared with the reported values for the pure DPPC bilayer [133].
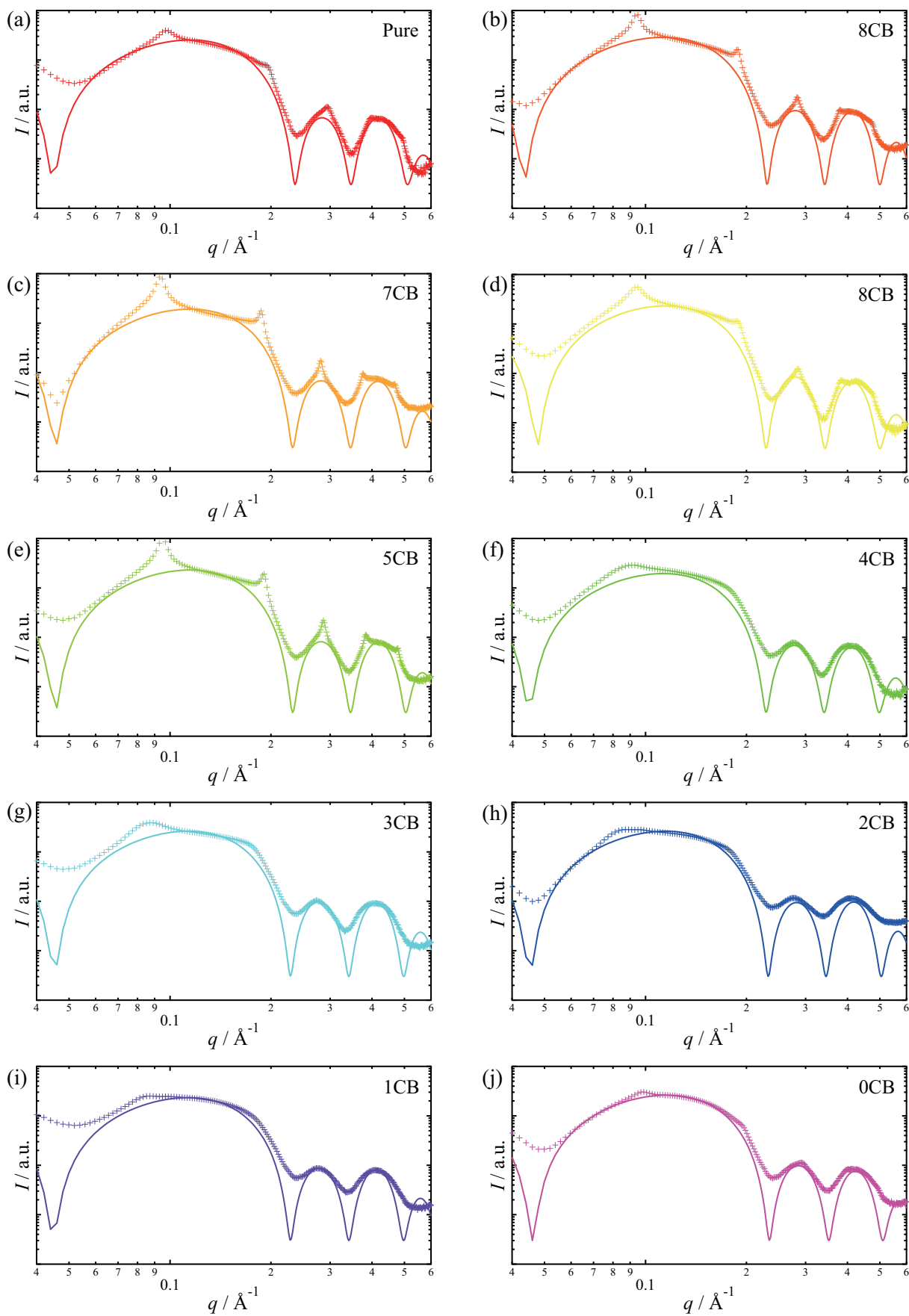
Fig. 4.3. Fitting results of the SAXS profiles of unilamellar vesicles of pure DPPC and DPPC containing 12mol% of nCB at 25 °C.
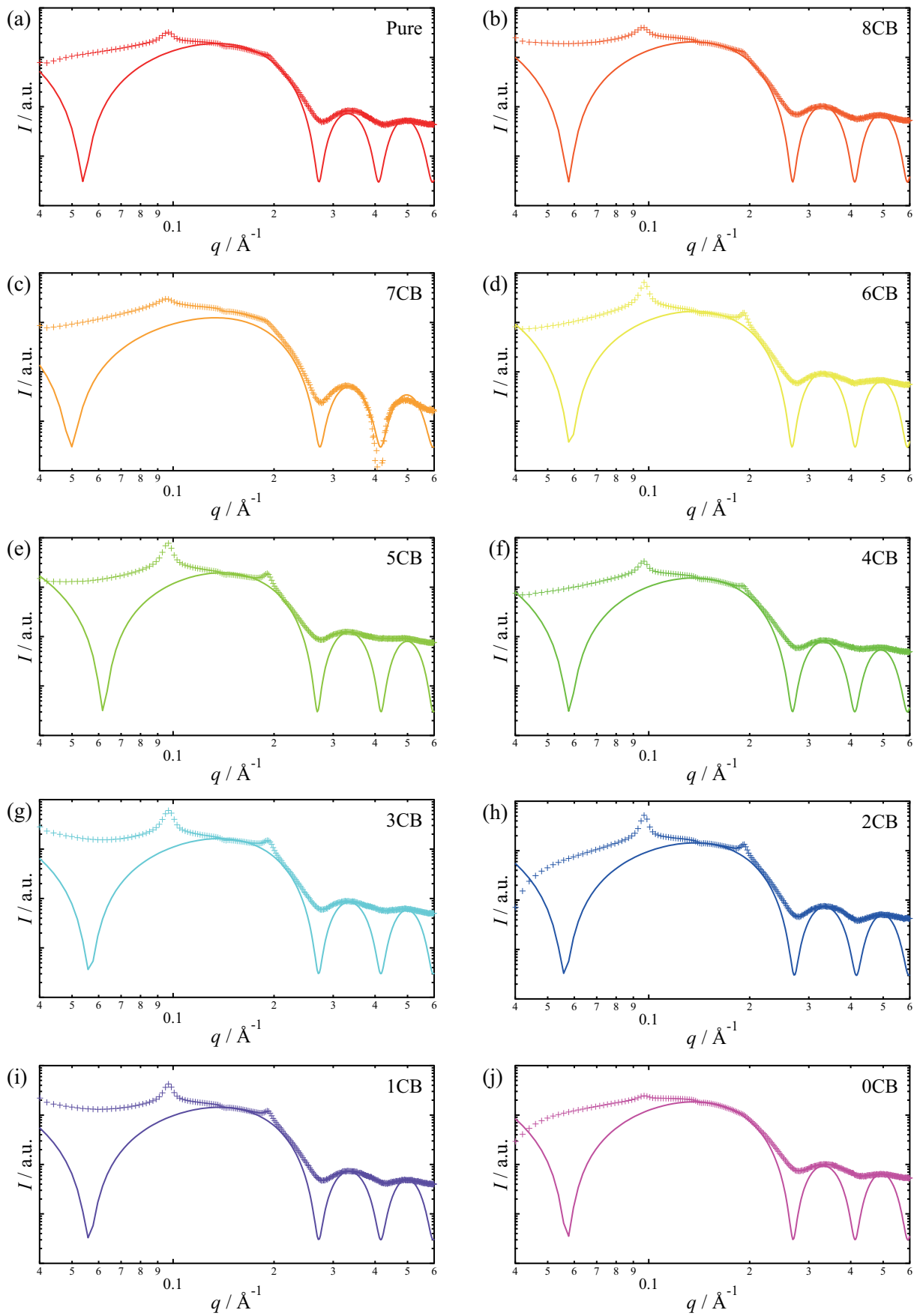
Fig. 4.4. Fitting results of the SAXS profiles of unilamellar vesicles of pure DPPC and DPPC containing 12mol% of nCB at 55 °C.

65
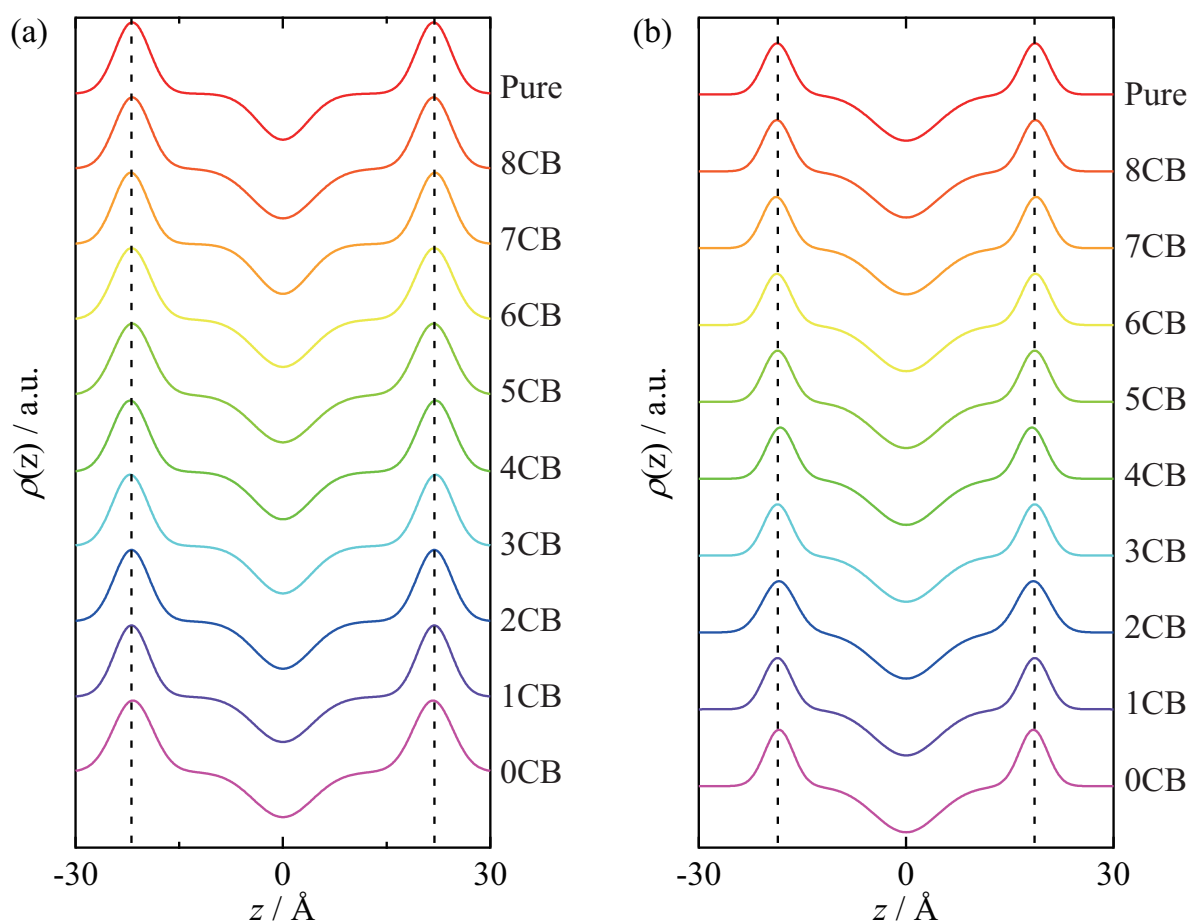
Fig. 4.5. Electron density profiles of bilayers of pure DPPC and DPPC containing 12mol% of nCB at (a) 25 °C and (b) 55 °C estimated from the fitting shown in Figs. 4.3 and 4.4. The dotted lines are guides at the peaks for the headgroups.
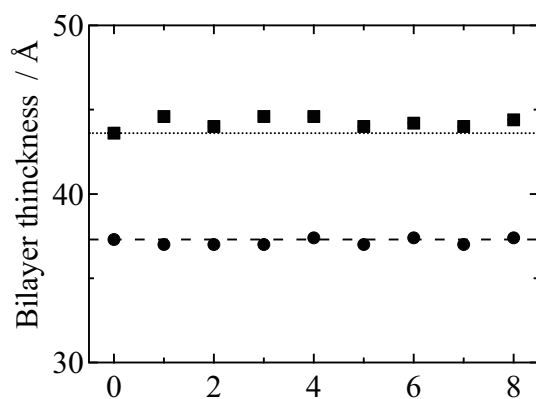

Fig. 4.6. Plots of bilayer thickness $2z_H$ at 25 °C (squares) and at 55 °C (circles) against nCB (12 mol%) alkyl chain length n. Dotted and dashed lines represent the thickness of the pure DPPC bilayer at each temperature.

In the gel and ripple phases, a diffraction peak was observed by WAXS due to the in-plane "nearly" hexagonal packing of the lipid molecule alkyl chains. The averaged lattice constants $s = s_{11} = s_{20}$ defined by Marsh *et al.* [65] were calculated from the peak positions $q = 2\pi/s$. Besides, the mean distance between the alkyl chains is given approximately by $2s/\sqrt{3}$. Figure 4.7 shows s obtained for DPPC bilayers both with and without nCB in the gel phase and indicates that the s obtained for pure DPPC is in good agreement with the reported value [65, 66]. Furthermore, s varies continuously with increasing chain length n, although the variations in s from that of pure DPPC are less significant than that caused by cholesterol [22]. The variation in s with chain length differs from that with n-alkanes, where s decreases. In the liquid-crystalline phase, the alkyl chains are disordered, and Bragg reflections vanish accordingly.

Both the small variation in the bilayer thickness and the monotonic change in the in-plain lattice constant indicate that there is no definite change in the manner of incorporation with different n. SAXS results indicate that nCB molecules are incorporated into the alkyl chain region, as indicated by the increase in electron density. Indeed, the SAXS and WAXS results indicated that nCBs do not alter the thickness of the bilayer in either the gel and liquid-crystalline phases, but does the lateral distance between the alkyl chains in the gel phase. When nCB molecules are located parallel to a bilayer at its central plane as illustrated in Fig. 4.8a, the thicknesses of the bilayer should increase by approximately 2-5 Å (i.e., the molecular width of nCB). Although analysis based on the scattering from lamellar structures yielded slightly different results from our estimate, this difference is in the range of 1 Å [132]. Thus, the minimal variation in bilayer thickness upon nCB addition implies that all nCB molecules lie approximately normal to the bilayer (i.e., parallel to the lipid alkyl chains, Fig. 4.8b) in both the gel and liquid-crystalline phases. The monotonic change in s in the gel phase is also consistent with this conclusion. Besides, the hydrogen bonding ability of the cyano group (–CN) to the phosphatidylcholine head group of DPPC [134] suggests that the cyano group oriented toward the lipid head group. Furthermore, the relatively constant bilayer thickness also indicates that nCB does not induce interdigitation, in contrast to the behavior of small amphiphilic molecules such as short-chain alcohols [135].

Having established comparable manner of incorporation for all nCBs, cholesterol, and n-alkanes, we can move on to discuss the effect of the molecular structures of the incorporated molecules on the phase behavior of the lipid bilayer. The phase behaviors of the DPPC/nCB bilayers were then investigated using DSC. Figure 4.9 shows the DSC traces of DPPC/nCB bilayers with even n on heating in the third cycle at a rate of 2 °C min^{-1}. The larger thermal anomaly is due to the main transition between the ripple phase and the liquid-crystalline phase. The anomaly is broadened, and shifts to
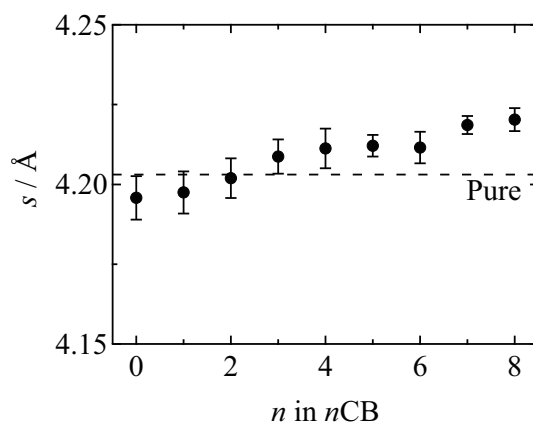
Fig. 4.7. Hexagonal lattice constant s of the alkyl chains in DPPC bilayers with nCB (12 mol%) obtained from WAXS. The dashed line is s of the pure DPPC bilayer. Error bars were estimated from the half-width at half maximum of the Bragg peaks obtained by the fitting with Lorentzian.
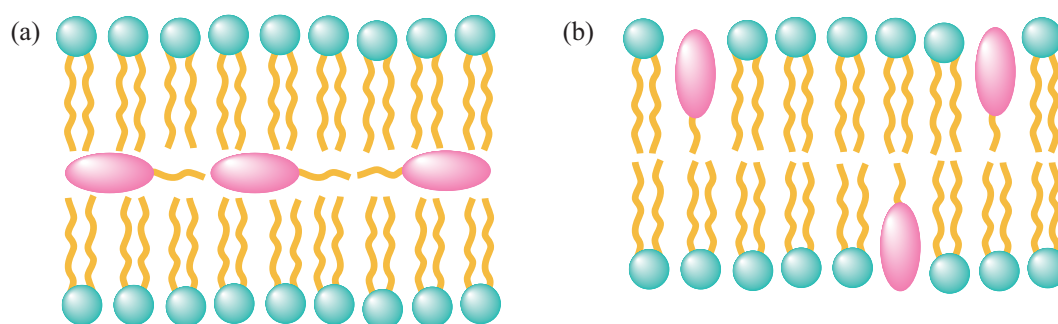

Fig. 4.8. (a) A bilayer containing nCB in the central plane. (b) A bilayer containing nCB parallel to the lipid alkyl chains.

lower temperatures as the nCB content increases. Similar trends are evident for the larger thermal anomaly (main transition) for all the DPPC/nCB systems. The smaller thermal anomaly is due to the pretransition between the gel phase and the ripple phase and exhibits significant n dependence compared to the main transition. When $n = 8, 6$, the pretransition peak once shifts to higher temperatures with becoming sharper and then shifts back to lower temperatures with becoming smaller. Upon the addition of 4CB, the pretransition peak is broadened and shifts to lower temperatures as the content increases. In the cases for 0CB and 2CB, the smaller peak shifts to lower temperatures becoming smaller, and eventually results in undetectable.

The change in transition temperatures in the presence of nCB of even values of n (0CB, 2CB, 4CB, 6CB and 8CB) are outlined in Fig. 4.10 against nCB contents. The broken lines represent the boundaries between the gel phase and the ripple phase (T_p), while the solid lines represent the boundaries between the liquid-crystalline phase (T_m). As shown, the decreases in T_m depend on the quantity of nCB added. Below 12.5 mol%, T_m decreased smoothly for all samples, indicating that the

limit of nCB incorporation into the DPPC bilayer is larger than 12.5 mol%. For 12.5 mol% and 15 mol% 0CB, T_m is comparable, indicating that the incorporation limit of 0CB is approximately 12.5 mol% and that any excess 0CB was excluded from the bilayer at an 0CB concentration of 15 mol%.

Indeed, this n-dependence can be seen more clearly for T_p than for T_m. When 0CB and 2CB are employed, T_p decreases gradually with increasing nCB content, and became undetectable at higher nCB content. In the case of 4CB, T_p also decreases with increasing nCB content. In contrast, for 6CB and 8CB, T_p initially increases, and then decreases at higher nCB contents above 10 mol%.
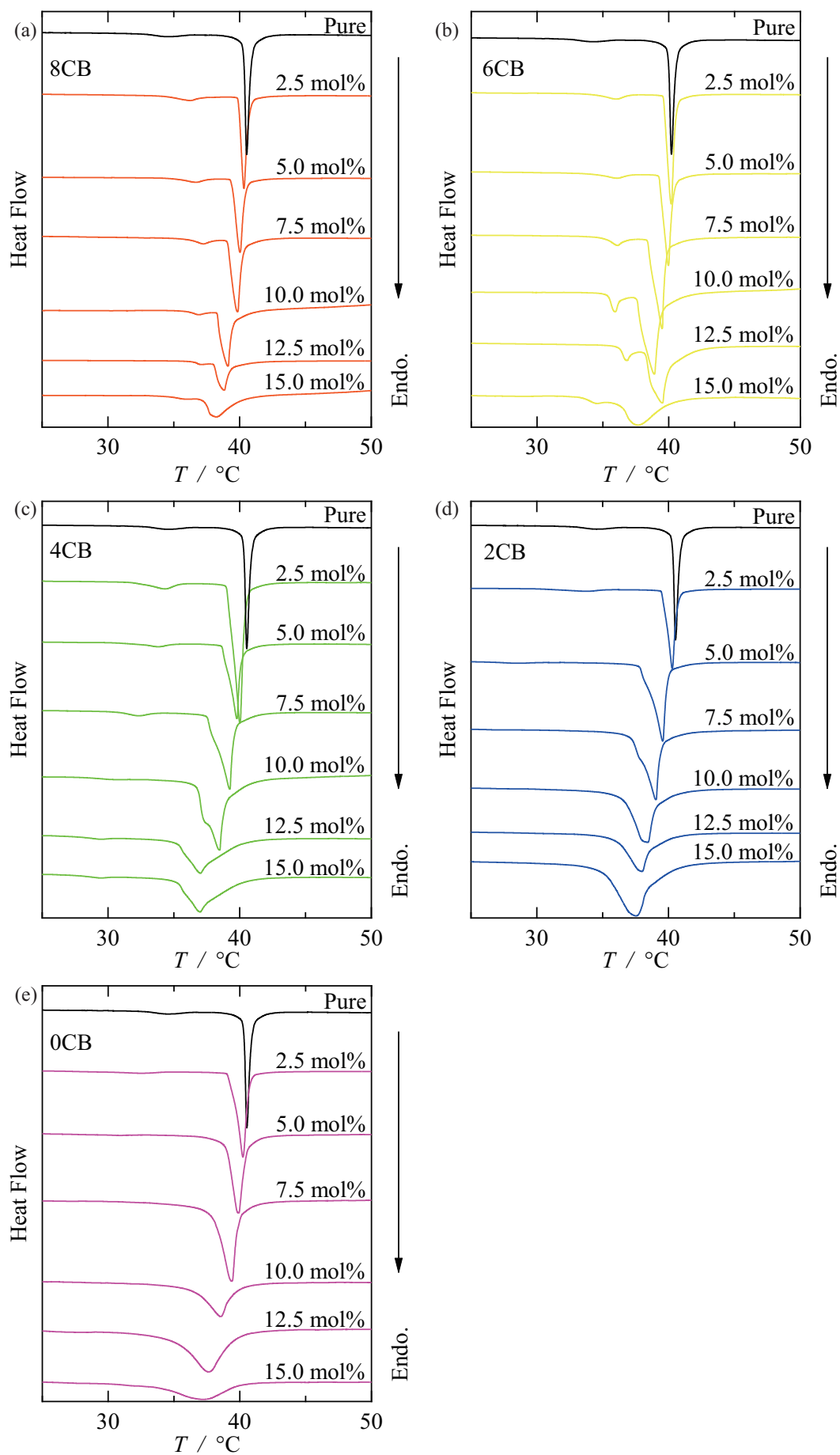
Fig. 4.9. DSC traces of pure DPPC and DPPC with various *n*CB. *n* in *n*CB and the *n*CB contents are as indicated.
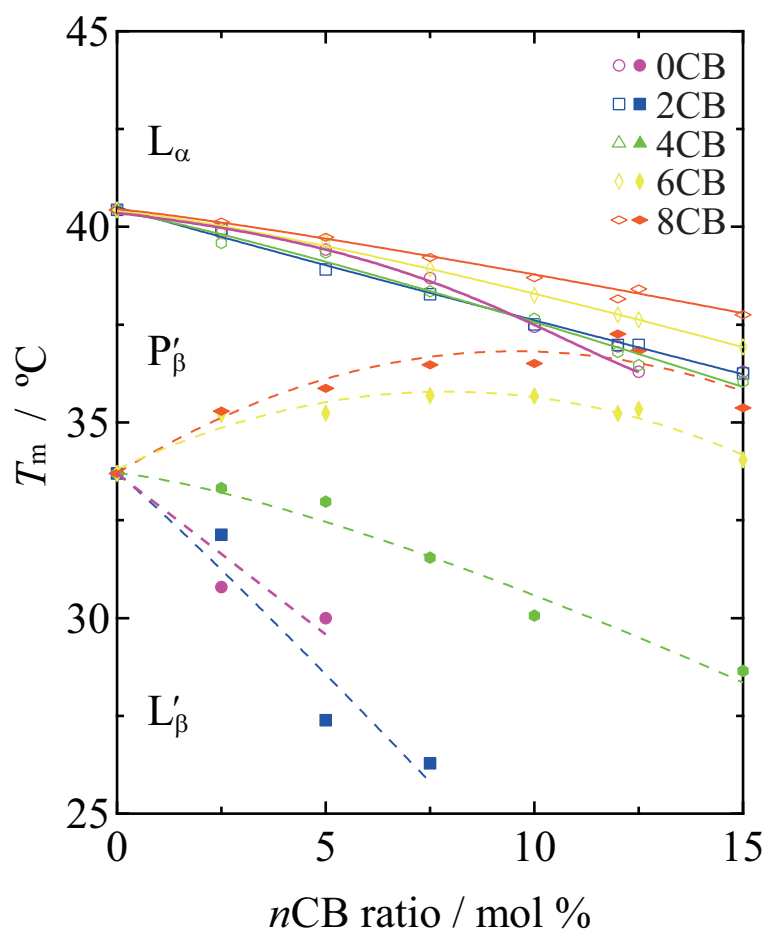
**Fig. 4.10.** Phase diagrams of DPPC with nCB with even n.

Finally, the n-dependence of T_m at 12 mol% nCB is summarized in Fig. 4.11. Although T_m remains relatively constant in the range $0 \leq n \leq 3$, at $n = 3$, T_m begins to increase with increasing n. Furthermore, the so-called odd-even effect is clearly observed, i.e., nCBs with even values of n lower T_m to a greater extent than those with odd n values.
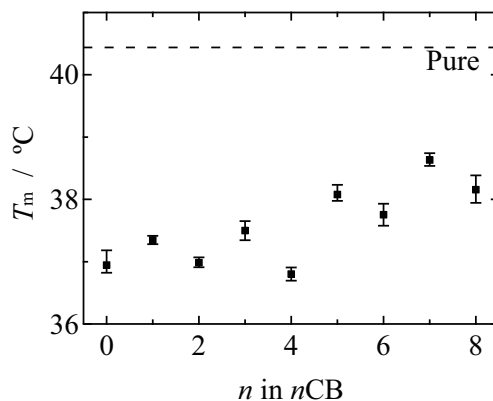

Fig. 4.11. n-dependence of T_m of DPPC with 12 mol% of nCB. Dashed line indicates T_m of the pure DPPC bilayer. Error bars show the maximum and the minimum values in three or more measurements.

Examination of the phase diagram (Figs. 4.10 and 4.11) indicates that the short- and long-chain nCBs exhibit different effects on the phase behavior. The phase diagrams of DPPC containing short-chain nCBs (0CB and 2CB) are similar to that of DPPC/cholesterol, in which T_m and T_p decrease with increasing nCB content, while T_p disappears [18, 23]. In contrast, with the incorporation of long-chain nCBs, T_p increases, with the pretransition step surviving even upon increasing the nCB content, as shown in Fig. 4.10. We confirmed that the observed trend for the pretransition with long-chain nCBs is comparable to that with n-alkanes, i.e., the T_p of DPPC containing 12 mol% C14 (36.8 °C) is higher than that of pure DPPC. Different effects on T_m were also observed in the presence of long- and short-chain nCBs, with a relatively constant T_m being recorded for $n = 0 - 3$, in contrast to the increase observed with nCB chains longer than $n = 3 - 8$.

These differences between the effects of long and short chains can reasonably be interpreted by considering the mobility of the nCB alkyl chains. nTCB (4-alkyl-4′-isothiocyanatobiphenyls) is a mesogenic series of compounds with a similar molecular structure to the nCB (the cyano group (–CN) of nCB is replaced by an isothiocyano group (–NCS)). The entropy changes of the transition of nTCB indicate that conformational disordering of the alkyl chain is suppressed for a few numbers of methylene groups close to the biphenyl core, as shown in Figs. 4.12 and 4.13 [42]. Since nCB possesses a similar core, a comparable effect on the methylene groups close to the core is expected for nCB. As short chains behave as part of the core because of the suppressed dynamics of the methylene groups [42], short-chain nCBs ($n = 0 - 3$) behave as core-like molecules. Accordingly, their influ-
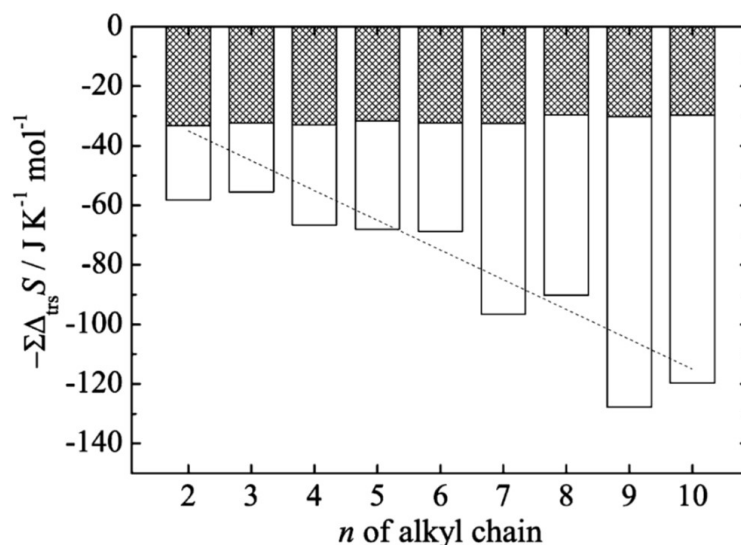
Fig. 4.12. The chain length dependence of transition entropy ($\sum \Delta_{\mathrm{trs}}S = \Delta_{\mathrm{CrE}}S + \Delta_{\mathrm{fus}}S$) of nTCB [42]. White and shaded bars represent $\Delta_{\mathrm{CrE}}S$, from a adjacent crystal to a CrE phase, and $\Delta_{\mathrm{fus}}S$, from the CrE phase to an isotropic liquid phase. The dotted line is a guide for the eyes with a slope of $10 \ \mathrm{J \ K^{-1}}$ (mol of $-\mathrm{CH_2}-)^{-1}$.
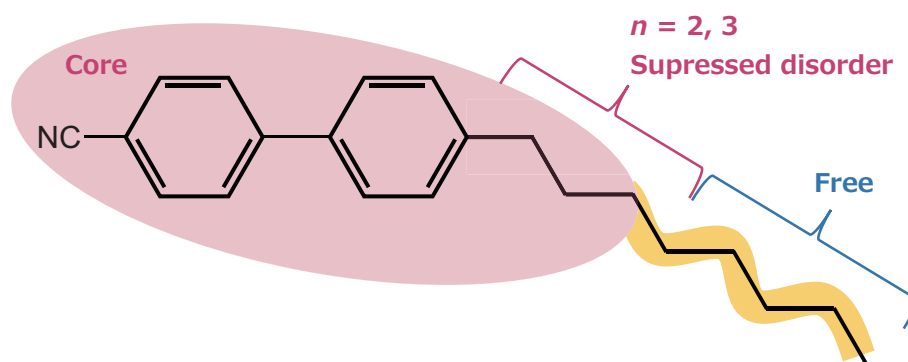
Fig. 4.13. A core and a chain of nCB.

ence on DPPC phase behavior is similar to that of cholesterol, which is a typical core-like molecule. Indeed, core-like molecules appear to disturb the order of lipid alkyl chains in the gel phase due to steric effects, thus resulting in the destabilization of the gel phase and a lower T_{m}. With nCB chains longer than $n = 3$, the chains furthest from the core exhibit greater flexibility. This flexible chain is considered similar to an alkane, enhancing the order of the lipid alkyl chains in the gel phase [24, 25]. In the case of alkanes, due to the enhanced structural order, T_{m} increases to a greater extent with longer alkanes [25, 33, 135]. The changes in the T_{m} variation at $n = 3$ imply that the effective core comprises a cyano group (–CN), a biphenyl group, and three methylene groups close to the biphenyl core. The methylene groups further from the biphenyl core (i.e., beyond the 3rd carbon) behave as part of a flexible chain. This flexible chain likely causes the increase in T_{p} with nCB content for larger n.
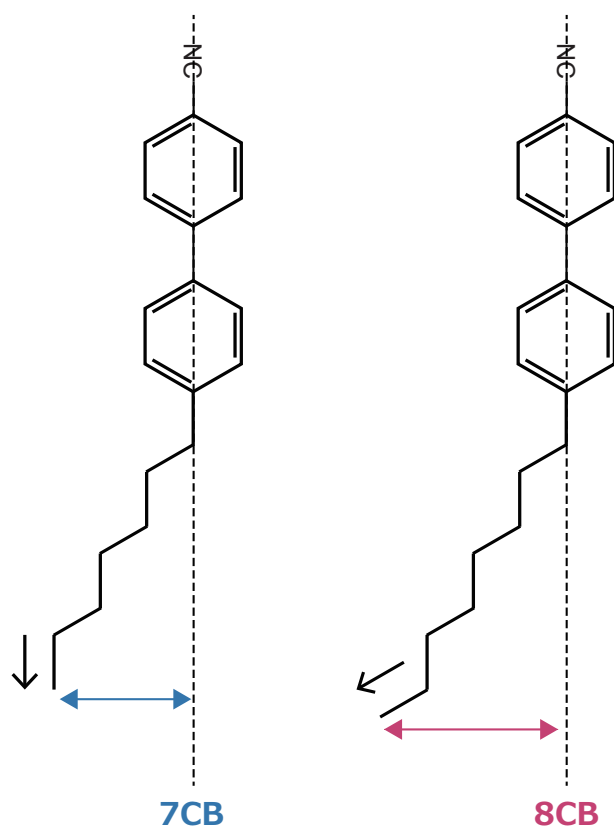
Fig. 4.14. The direction of terminal methyl groups in against the long axis of the molecules in the cases of 7CB and 8CB.

Furthermore, as shown in Fig. 4.11, an odd-even effect is observed for T_m upon the addition of nCB. Although such odd-even effects are widely observed in compounds containing alkyl groups (e.g., n-alkanes and mesogens such as nCB) [136–138], the present one is distinct from such observations because the effect is caused by additives. Interestingly, an odd-even effect caused by minor component length has recently been reported in the nCB binary system [46]. The origin of the effect reported herein may be the higher anisotropy of nCB molecules with odd values of n as shown in Fig. 4.14 [139].

The effects of additives on T_p have not yet been studied in as much detail, as the pretransition tends to become undetectable even with small quantities of additives [18, 23]. However, in the present nCB-added system, the pretransition survives at high additive contents, thus allowing the content dependence of T_p to be clearly observed (see Fig. 4.10). Interestingly, in nCB molecules with small values of n ($n \leq 4$), T_p lowers with increasing additive content in the bilayer, while with large values of n ($n > 4$), T_p increases. The former effect is similar to that observed for cholesterol [23] while the latter is similar to that observed for C14. Furthermore, these varying trends for T_p with n can be interpreted as a result of competing effects between the core and the chain, as observed for T_m.

Finally, the partition coefficients [70] of nCB during the pretransition and the main transition cannot be discussed at present due to lack of information regarding the enthalpy change during the transitions. These factors appear informative for understanding the observed phase behaviors in greater detail, and so will be examined in a future study.

4.0.4 Conclusion

In this study, the effects of nCB on the phase behavior of DPPC bilayers are investigated to clarify the roles of a core and an alkyl chain in a single incorporated molecule. After confirming that nCB molecules lie parallel to lipid molecules in the bilayers irrespective of the alkyl chain length n, we compared the phase diagrams of DPPC/nCB with different n. At approximately $n = 3$, changes in the phase behavior appear. For short-chain nCBs, T_p decreased, and the transition vanishes with increasing nCB content, while T_m remains relatively constant upon chain elongation. In contrast, for long-chain nCBs, T_p increased with increasing nCB content, while T_m increased with chain elongation. These observations are interpreted based on what bulky and rigid molecules (e.g., cholesterol) have distinct and different effects on the phase behavior of bilayers compared to straight chainlike molecules (e.g., n-alkanes). The varying effects of short- and long-chain nCBs arises from the contrasting effects of the core and the flexible chain within a nCB molecule. In addition, nCB molecules where $n \leq 3$ are overall regarded as core-like molecules. This behavior is consistent with the mobility of the methylene groups in the nCB alkyl chains. Namely, the core disturbs the bilayer structural order in the gel phase and lowers the main transition temperature, while the part of the alkyl chain far from the core enhances the order and raises the main transition temperature. The present results suggest that the core and the flexible chain incorporated into a single molecule play different roles in lipid membranes.

Chapter 5

General Conclusion

The microscopic shape of a constituting molecule influences macroscopic properties such as assembly structure, phase behavior, and dynamics. The effects of molecular shape have been reported to exist in a binary system, and sometimes the minor component changes the entire physicochemical properties of the system. In bilayer membrane systems, especially, significant effects of additives have been enormously reported thus far, and the effects seem to differ depending on the structural feature of the additives. Although incorporation effects have been understood rather well for some specific molecules such as cholesterol, systematic understanding has not been achieved yet. In this work, we aimed at a systematic understanding of incorporation effects in the lipid bilayer system for the varying shape of added molecules. We characterized the molecular shape, the length, bulkiness, and the balance between a bulky core and a straight alkyl chain in a single molecule. DPPC was used as a lipid throughout the present study. The effects of chainlike additives were discussed in Chapter 3 for straight chainlike molecules with different terminal groups or chain lengths. Molecules with both a core and a chain were subject to discussion in Chapter 4 using a homologous series of a liquid crystalline compound.

We firstly investigated the effects of strait chainlike molecules, as described in Chapter 3. Straight chainlike molecules are classified as similarly shaped molecules since the two alkyl chains of DPPC are saturated and not branched. We examined the effects of straight chainlike molecules from the viewpoint of molecular shape in three sections:

In Sec. 3.1, we employed nine kinds of n-tetradecane derivatives (C14-X, X = H, Br, Cl, COOCH$_3$, SH, OH, COOH, PO$_3$H$_2$, NH$_2$) as straight chainlike molecules to explore the molecular shape dependence in the incorporation effects. The incorporation effects should be similar when the molecular shape of the additives are similar if the additives affect membrane properties depending on their molecular shapes. C14-X were added to DPPC bilayers separately at a various ratio up to 30 mol%,

and WAXS and DSC measurements were conducted. WAXS results revealed that the lattice constants of the alkyl chains decrease in the gel phase with increasing the C14-X content in the DPPC bilayer. The decreasing manners are similar in all the cases of C14-X, indicating the C14-X affects membrane structure similarly in the gel phase. In DSC measurements, the thermal anomaly was observed due to the gel to liquid-crystalline transition (the main transition) in all cases and shifted to higher temperatures with increasing the C14-X content. The shift means that the T_m elevates upon the incorporation of C14-X. The trend of T_m changes are similar for all C14-X, though the extent is different for T_m elevation and broadening of the thermal anomalies depending on the chemical species of the terminal group, X. The common trends in the lattice constants and the phase behavior suggest that straight chainlike molecules affect the membrane properties in a similar way irrespective of their terminal groups. These results support that the incorporation effects in lipid membranes depend on the molecular shape of the additives. Further, the finding implies that a *n*-alkane can serve as a representative of chainlike molecules.

In Sec. 3.2, the effect of a straight chainlike molecule was investigated on the mechanical property of DPPC membranes in the liquid-crystalline phase using C14 as a representative of straight chainlike molecules, as indicated in Sec. 3.1. We estimated the bending modulus, κ, by analyzing vesicle fluctuations using a phase-contrast microscope. κ of the pure DPPC bilayer and DPPC/C14 (DPPC : C14 = 6 : 4 (mol : mol)) bilayer are $(1.6 \pm 0.2) \times 10^{-19}$ J and $(1.4 \pm 0.2) \times 10^{-19}$ J, respectively, indicating that there is no significant change in κ upon the C14 incorporation. The result indicates that straight chainlike molecules do not affect κ of the liquid-crystalline phase. This result is opposed to the C14 effect in the gel phase, where κ becomes ten times larger than that of the pure DPPC bilayer, which means that C14 widens the gap of membrane properties. The trend is also observed in molecular packing and thermostability, whereas opposed to that of cholesterol, which significantly affects membrane properties in both phases and makes the state similar. The results emphasized the opposing effects of cholesterol and straight chainlike molecules.

In Sec. 3.3, we further investigated the effects of straight chainlike molecules on membrane dynamics in the liquid-crystalline phase. We employed C8, C10, C12, and C14 as chainlike molecules to investigate chain length dependence of the effect of chainlike molecules and added them 40 mol% to the DPPC bilayer. SAXS and SANS results revealed that, with increasing the *n*-alkane length, the thickness of the hydrophobic region d_c increases, and the population of *n*-alkanes increases in the center of the bilayer. NSE data of bending fluctuations clarified that κ becomes lower for longer *n*-alkane incorporation. NSE data also indicate increases in the amplitude and the relaxation time τ_{TF} of the thickness fluctuations upon the *n*-alkane incorporation. Combining the results of d_c, κ,

and the amplitude of the thickness fluctuations, we concluded that the coupling between the leaflets in a bilayer is weakened on the elongation of added n-alkanes. The bilayer softening (decrease in κ) despite being thicker can be explained due to the decoupling of the leaflets. The decoupling seems to be consistent with the increased amount of n-alkanes in the bilayer center with increasing the chain length, suggesting that the decreased physical interactions between the leaflets weakened the interleaflet coupling. This relation can be explained as the correlation between the microscopic structural changes and the mesoscale dynamical changes. The findings emphasize that adding straight chainlike molecules brings the length-dependent effects on the membrane dynamics and the structure in the liquid-crystalline phase as well, although the effect is weak compared to that in the gel phase. Further, the incorporation effects of straight chainlike molecules depend on their lengths, which is also a structural feature of additives.

As summarized above, Chapter 3 has revealed that straight chainlike molecules have significant effects on the physicochemical and mechanical properties in lipid bilayer systems. The effects of straight chainlike molecules are opposed to the known effects of cholesterol, which has a shape different from that of the major component lipid. The incorporation effects of straight chainlike molecules depend on their lengths, which is also a structural feature of additives. These results support the idea that the membrane properties strongly depend on the molecular shape of the additives.

In Chapter 4, we explored the effects of additives which have a core and a chain while imagining that a core and a chain have competing effects even when they coexist in a single molecule, assuming that the incorporation effect is merely additive. To clarify this issue, we chosen a series of 4-n-alkyl-4′-cyanobiphenyl (nCB, n being the number of carbon atoms in the alkyl chain) as a suitable series of molecules that realize systematic control of the molecular shape by changing the length of a chain attached to a core. The effects of nCB on the phase behavior of DPPC bilayers were investigated to clarify the roles of a core and an alkyl chain in a single incorporated molecule. SAXS and WAXS results indicated that the incorporated nCB lie parallel to lipid molecules in the bilayers irrespective of n. DSC data revealed that T_m decreases upon the incorporation of nCB, indicating that the effects of core appeared dominantly. Further, the trend in the effects on the phase behavior changed at approximately $n = 3$. For short-chain nCBs, T_p decreased, and the transition vanished with increasing nCB content, while T_m remains relatively constant upon chain elongation. In contrast, for long-chain nCBs, T_p increased with increasing nCB content, while T_m increased with chain elongation. The varying effects of short- and long-chain nCBs arises from the opposing effects of the core and the straight chainlike within a nCB molecule. In addition, nCB molecules where $n \leq 3$ are overall regarded as core-like molecules. The results can be interpreted as that the core disturbs the bilayer

structural order in the gel phase and lowers T_m, while the part of the alkyl chain far from the core enhances the order and raises T_m. The results suggest that the core and the chain in a single molecule play different roles in lipid membranes.

In conclusion, we investigated the effects of additives on lipid membrane properties from the viewpoint of the molecular shape and found significant dependence on the structural features of the additives. Several organic molecules were added to the DPPC bilayer, and their effects are compared while paying attention to whether the molecule is similar to the host component or not. The results revealed that the incorporation effects strongly depend on the similarity between additives and the major component. Further, the effects of additives depend on the molecular shape when the shape is systematically changed. It is a correlation between the microscopic structures and mesoscopic or macroscopic properties. The present investigation should contribute to the systematic understanding of the incorporation effects in lipid bilayers, and the knowledge can be used to predict the effects of other organic molecules whose effects are not known yet. A lipid bilayer has only two molecules in the direction normal to the surface, but, on the membrane surface, there are a large number of molecules aligned. These characteristics cause macroscopic behaviors such as phase transitions within the surface and the high deformability and fluctuations to the normal direction. Although the lipid bilayer is such a unique material, it is a general component of biological membranes and chemical products such as cosmetics. The systematic understanding of the relationship between the shape of constituents and membrane properties will be useful for development not only in material science but also in the fields of biology and engineering.

Bibliography

[1] K. Akabori, J. F. Nagle, *Soft Matter*, 2015, **11**, 918–926.

[2] R. Koynova, M. Caffrey, *Biochim. Biophys. Acta*, 1998, **1376**, 91 – 145.

[3] H. Seto, N. L. Yamada, M. Nagao, M. Hishida, T. Takeda, *Euro. Phys. J. E*, 2008, **26**, 217 – 223.

[4] C.-H. Lee, W.-C. Lin, J. Wang, *Phys. Rev. E*, 2001, **64**, 020901.

[5] W. Helfrich, *Z. Naturforsch. C*, 1973, **28**, 693–703.

[6] Y. Suezaki, H. Ichinose, *J. Phys. I France*, 1995, **5**, 1469–1480.

[7] S. A. SAFRAN, *Adv. Phys.*, 1999, **48**, 395–448.

[8] R. J. Bingham, S. W. Smye, P. D. Olmsted, *Europhys. Lett.*, 2015, **111**, 18004.

[9] E. YEUNG, A; EVANS, *J. Phys. II, France*, 1995.

[10] U. Seifert, S. A. Langer, *Europhys. Lett.*, 1993, **23**, 71–76.

[11] U. Seifert, S. A. Langer, *Biophys. Chem.*, 1994, **49**, 13 – 22.

[12] M. Nagao, E. G. Kelley, R. Ashkar, R. Bradbury, P. D. Butler, *J. Phys. Chem. Lett.*, 2017, **8**, 4679–4684.

[13] J. Faucon, M. D. Mitov, P. Méléard, I. Bivas, P. Bothorel, *J. Physique*, 1989, **50**, 2389–2414.

[14] L. Movileanu, D. Popescu, S. Ion, A. I. Popescu, *Bull. Math. Biol.*, 2006, **68**, 1231–1255.

[15] S. Hladky, D. W. R. Gruen, *Biophys. J.*, 1984, **45**, 645–646.

[16] I. Miller, *Biophys. J.*, 1984, **45**, 643 – 644.

[17] S. Hladky, D. Gruen, *Biophys. J.*, 1982, **38**, 251 – 258.

[18] T. P. W. McMullen, R. N. McElhaney, *Biochim. Biophys. Acta*, 1995, **1234**, 90 – 98.

[19] B. D. Ladbrooke, R. M. Williams, D. Chapman, *Biochim. Biophys. Acta*, 1968, **150**, 333 – 340.

[20] R. A. Demel, B. D. Kruyff, *Biochim. Biophys. Acta*, 1976, **457**, 109 – 132.

[21] H. Ohvo-Rekilä, B. Ramstedt, P. Leppimäki, J. P. Slotte, *Prog. Lipid Res.*, 2002, **41**, 66 – 97.

[22] T. T. Mills, J. Huang, G. W. Feigenson, J. F. Nagle, *Gen. Physiol. Biophys.*, 2009, **28**, 126–39.

[23] N. Tamai, T. Izumikawa, S. Fukui, M. Uemura, M. Goto, H. Matsuki, S. Kaneshina, *Biochim. Biophys. Acta*, 2013, **1828**, 2513 – 2523.

[24] M. Hishida, R. Yanagisawa, H. Usuda, Y. Yamamura, K. Saito, *J. Chem. Phys.*, 2016, **144**, 041103.

[25] M. Hishida, A. Endo, K. Nakazawa, Y. Yamamura, K. Saito, *Chem. Phys. Lipids*, 2015, **188**, 61 – 67.

[26] H. Usuda, M. Hishida, Y. Yamamura, K. Saito, *Langmuir*, 2016, **32**, 5966–5972.

[27] H. Usuda, M. Hishida, Y. Yamamura, K. Saito, *Chem. Lett.*, 2018, **47**, 1512–1514.

[28] K. Simons, E. Ikonen, *Nature*, 1997, **387**, 569–72.

[29] R. A. Haberkorn, R. G. Griffin, M. D. Meadows, E. Oldfield, *J. Am. Chem. Soc.*, 1977, **99**, 7353–7355.

[30] G. W. Stockton, I. C. Smith, *Chem. Phys. Lipids*, 1976, **17**, 251 – 263.

[31] E. Oldfield, M. Meadows, D. Rice, R. Jacobs, *Biochem.*, 1978, **17**, 2727–2740.

[32] J. H. Ipsen, G. Karlström, O. G. Mourtisen, H. Wennerström, M. J. Zuckermann, *Biochim. Biophys. Acta*, 1987, **905**, 162 – 172.

[33] T. J. McIntosh, S. A. Simon, R. C. MacDonald, *Biochim. Biophys. Acta*, 1980, **597**, 445 – 463.

[34] D. A. Haydon, B. M. Hendry, S. R. Levinson, J. Requena, *Biochim. Biophys. Acta*, 1977, **470**, 17 – 34.

[35] S. H. White, *Biophys. J.*, 1978, **23**, 337 – 347.

[36] J. M. Pope, L. W. Walker, D. Dubro, *Chem. Phys. Lipids*, 1984, **35**, 259 – 277.

[37] D. A. Haydon, B. M. Hendry, S. R. Levinson, J. Requena, *Nature*, 1977, **268**, 356–358.

[38] J. Israelachvili, *Coll. Surf. A*, 1994, **91**, 1 – 8, A selection of papers presented at the First World Congress on Emulsions.

[39] L. Onsager, *Ann. NY Acad. Sci.*, 1949, **51**, 627–659.

[40] T. Niori, T. Sekine, J. Watanabe, T. Furukawa, H. Takezoe, *J. Mater. Chem.*, 1996, **6**, 1231–1233.

[41] K. Saito, M. Sorai, *Chem. Phys. Lett.*, 2002, **366**, 56 – 61.

[42] K. Horiuchi, Y. Yamamura, R. Pełka, M. Sumita, S. Yasuzuka, M. Massalska-Arodz, K. Saito, *J. Phys. Chem. B*, 2010, **114**, 4870–4875.

[43] Y. Yamamura, T. Adachi, T. Miyazawa, K. Horiuchi, M. Sumita, M. Massalska-Arodź, S. Urban, K. Saito, *J. Phys. Chem. B*, 2012, **116**, 9255–9260.

[44] R. J. Cox, J. F. Johnson, *IBM J. Res. Dev.*, 1978, **22**, 51–59.

[45] M. Lafouresse, M. Sied, H. Allouchi, D. López, J. Salud, J. Tamarit, *Chem. Phys. Lett.*, 2003, **376**, 188 – 193.

[46] S. Fujimura, Y. Yamamura, M. Hishida, S. Nagatomo, K. Saito, *Liq. Cryst.*, 2014, **41**, 927–932.

[47] S. Kutsumizu, K. Morita, S. Yano, S. Nojima, *Liq. Cryst.*, 2002, **29**, 1459–1468.

[48] K. Saito, A. Sato, M. Sorai, *Liq. Cryst.*, 1998, **25**, 525–530.

[49] K. Nakazawa, M. Hishida, S. Nagatomo, Y. Yamamura, K. Saito, *Chem. Lett.*, 2014, **43**, 1352–1354.

[50] M. G. K. Benesch, D. A. Mannock, R. N. A. H. Lewis, R. N. McElhaney, *Biochemistry*, 2011, **50**, 9982–9997.

[51] R. Abboud, H. Greige-Gerges, C. Charcosset, *J. Membr. Biol.*, 2015, **248**, 811–824.

[52] T. McIntosh, *Biophys. J.*, 1980, **29**, 237 – 245.

[53] K. Lohner, *Chem. Phys. Lipids*, 1991, **57**, 341 – 362.

[54] J. M. Pope, D. Dubro, *Biochim. Biophys. Acta*, 1986, **858**, 243–253.

[55] S. C. Mraw, *Rev. Sci. Ins.*, 1982, **53**, 228–231.

[56] P. Le Parlouër, *Thermal Analysis and Calorimetry Techniques for Catalytic Investigations*, 2013, pp. 51–101.

[57] F. Zernike, *Physica*, 1942, **9**, 686 – 698.

[58] F. Zernike, *Science*, 1955, **121**, 345–349.

[59] N. Shimizu, T. Mori, Y. Nagatani, H. Ohta, S. Saijo, H. Takagi, M. Takahashi, K. Yatabe, T. Kosuge, N. Igarashi, *AIP Conf. Proc.*, 2019, **2054**, 060041.

[60] N. Shimizu, T. Mori, N. Igarashi, H. Ohta, Y. Nagatani, T. Kosuge, K. Ito, *J. Phys.: Conf. Ser.*, 2013, **425**, 202008.

[61] J. Ilavsky, *J. Appl. Crystallogra.*, 2012, **45**, 324–328.

[62] F. Mezei, *Z. Phys.*, 1972, **255**, 146–160.

[63] E. G. Kelley, P. D. Butler, M. Nagao, *Collective Dynamics in Model Biological Membranes Measured By Neutron Spin Echo Spectroscopy*, De Gruyter, Berlin, Boston, 2019, chapter 4, pp. 131–176.

[64] T. Harayama, H. Riezman, *Nat. Rev. Mol. Cell Biol.*, 2018, **19**, 281 EP –, Review Article.

[65] D. Marsh, *Chem. Phys. Lipids*, 2012, **165**, 59 – 76.

[66] W. J. Sun, S. Tristram-Nagle, R. M. Suter, J. F. Nagle, *Biochim. Biophys. Acta*, 1996, **1279**, 17 – 24.

[67] T. Inoue, S. ichi Yanagihara, Y. Misono, M. Suzuki, *Chem. Phys. Lipids*, 2001, **109**, 117 – 133.

[68] P. Høyrup, J. Davidsen, K. Jørgensen, *J. Phys. Chem. B*, 2001, **105**, 2649–2657.

[69] H. Matsuki, K. Kato, H. Okamoto, S. Yoshida, M. Goto, N. Tamai, S. Kaneshina, *Chem. Phys. Lipids*, 2017, **209**, 9 – 18.

[70] M. Nishimoto, T. Hata, M. Goto, N. Tamai, S. Kaneshina, H. Matsuki, I. Ueda, *Chem. Phys. Lipids*, 2009, **158**, 71 – 80.

[71] S. E. Schullery, T. A. Seder, D. A. Weinstein, D. A. Bryant, *Biochem.*, 1981, **20**, 6818–6824.

[72] J. M. Boggs, G. Rangaraj, K. M. Koshy, *Chem. Phys. Lipids*, 1986, **40**, 23 – 34.

[73] J.-S. Chiou, P. R. Krishna, H. Kamaya, I. Ueda, *Biochim. Biophys. Acta*, 1992, **1110**, 225 – 233.

[74] J. M. Boggs, *Biochim. Biophys. Acta*, 1987, **906**, 353 – 404.

[75] B. T. R. Koynova, *OA Biochem.*, 2013, **1**, 1–9.

[76] E. B. Sirota, G. S. Smith, C. R. Safinya, R. J. Plano, N. A. Clark, *Science*, 1988, **242**, 1406–1409.

[77] M. Luckey, *Membrane Structural Biology: With Biochemical and Biophysical Foundations*, Cambridge University Press, 1998.

[78] G. D. Bothun, B. L. Knutson, H. J. Strobel, S. E. Nokes, *Coll. Surf. A*, 2006, **279**, 50 – 57.

[79] J. Pan, T. T. Mills, S. Tristram-Nagle, J. F. Nagle, *Phys. Rev. Lett.*, 2008, **100**, 198103.

[80] J. Pan, S. Tristram-Nagle, J. Nagle, *Phys. Rev. E*, 2009, **80**, 021931.

[81] Y. Wang, P. Gkeka, J. E. Fuchs, K. R. Liedl, Z. Cournia, *Biochim. Biophys. Acta*, 2016, **1858**, 2846 – 2857.

[82] G. Arfken, *Mathematical Methods for Physicists*, Akademic Press, 1970.

[83] C. A. Schneider, W. S. Rasband, K. W. Eliceiri, *Nature Methods*, 2012, **9**, 671–675.

[84] J. Genova, V. Vitkova, I. Bivas, *Phys. Rev. E*, 2013, **88**, 022707.

[85] R. Phillips, T. Ursell, P. Wiggins, P. Sens, *Nature*, 2009, **459**, 379–385.

[86] O. S. Andersen, R. E. Koeppe, *Annu. Rev. Biophys. Biomol. Struct.*, 2007, **36**, 107–130.

[87] M. F. Brown, *Annu. Rev. Biophys.*, 2017, **46**, 379–410.

[88] J. A. Lundbaek, S. A. Collingwood, H. I. Ingólfsson, R. Kapoor, O. S. Andersen, *J. Royal Soc. Interface*, 2010, **7**, 373–395.

[89] A. G. Zilman, R. Granek, *Phys. Rev. Lett.*, 1996, **77**, 4788–4791.

[90] M. Nagao, *Phys. Rev. E*, 2009, **80**, 031606.

[91] M. Rahimi, M. Arroyo, *Phys. Rev. E*, 2012, **86**, 011932.

[92] J.-H. Lee, S.-M. Choi, C. Doe, A. Faraone, P. A. Pincus, S. R. Kline, *Phys. Rev. Lett.*, 2010, **105**, 038101.

[93] Z. Yi, M. Nagao, D. P. Bossev, *J. Phys., Condens. Matter*, 2009, **21**, 155104.

[94] T. Takeda, Y. Kawabata, H. Seto, S. Komura, S. K. Ghosh, M. Nagao, D. Okuhara, *J. Phys. Chem. Solids*, 1999, **60**, 1375 – 1377.

[95] M. C. Watson, F. L. H. Brown, *Biophys. J.*, 2010, **98**, L9 – L11.

[96] R. Bradbury, M. Nagao, *Soft Matter*, 2016, **12**, 9383–9390.

[97] E. G. Kelley, P. D. Butler, M. Nagao, *Soft Matter*, 2019, **15**, 2762–2767.

[98] A. C. Woodka, P. D. Butler, L. Porcar, B. Farago, M. Nagao, *Phys. Rev. Lett.*, 2012, **109**, 058102.

[99] M. Nagao, S. Chawang, T. Hawa, *Soft Matter*, 2011, **7**, 6598–6605.

[100] V. Lee, T. Hawa, *J. Chem. Phys.*, 2013, **139**, 124905.

[101] R. Ashkar, M. Nagao, P. D. Butler, A. C. Woodka, M. K. Sen, T. Koga, *Biophys. J.*, 2015, **109**, 106 – 112.

[102] J.-M. Y. Carrillo, J. Katsaras, B. G. Sumpter, R. Ashkar, *J. Chem. Theory Comput.*, 2017, **13**, 916–925.

[103] E. Lindahl, O. Edholm, *Biophys. J.*, 2000, **79**, 426 – 433.

[104] P. G. Saffman, M. Delbrück, *Proc. Natl. Acad. Sci. U. S. A.*, 1975, **72**, 3111–3113.

[105] G. Bryant, M. B. Taylor, T. A. Darwish, A. M. Krause-Heuer, B. Kent, C. J. Garvey, *Coll. Surf. B*, 2019, **177**, 196 – 203.

[106] C. J. Glinka, J. G. Barker, B. Hammouda, S. Krueger, J. J. Moyer, W. J. Orts, *J. Appl. Crystallogra.*, 1998, **31**, 430–445.

[107] S.-M. Choi, J. G. Barker, C. J. Glinka, Y. T. Cheng, P. L. Gammel, *J. Appl. Crystallogra.*, 2000, **33**, 793–796.

[108] S. R. Kline, *J. Appl. Crystallogra.*, 2006, **39**, 895–900.

[109] N. Rosov, S. Rathgeber, M. Monkenbusch, *Neutron Spin Echo Spectroscopy at the NIST Center for Neutron Research*, American Chemical Society, 1999, chapter 7, pp. 103–116.

[110] M. Monkenbusch, R. Schätzler, D. Richter, *Nucl. Instrum. Meth. Phys. Res. A*, 1997, **399**, 301 – 323.

[111] R. T. Azuah, L. R. Kneller, Y. Qiu, P. L. W. Tregenna-Piggott, C. M. Brown, J. R. D. Copley, *J. Res. NIST*, 2009, **114**, 341.

[112] N. Chu, N. Kučerka, Y. Liu, S. Tristram-Nagle, J. F. Nagle, *Phys. Rev. E*, 2005, **71**, 041904.

[113] R. Dimova, *Adv. Colloid Interface Sci.*, 2014, **208**, 225 – 234, Special issue in honour of Wolfgang Helfrich.

[114] J. Pan, S. Tristram-Nagle, N. Kučerka, J. F. Nagle, *Biophys. J.*, 2008, **94**, 117 – 124.

[115] M. Hirai, H. Iwase, T. Hayakawa, M. Koizumi, H. Takahashi, *Biophys. J.*, 2003, **85**, 1600–1610.

[116] E. Drolle, N. Kučerka, M. I. Hoopes, Y. Choi, J. Katsaras, M. Karttunen, Z. Leonenko, *Biochim. Biophys. Acta*, 2013, **1828**, 2247 – 2254.

[117] D. W. R. Gruen, D. A. Haydon, *Biophys. J.*, 1980, **30**, 129 – 136.

[118] S. H. White, G. I. King, J. E. Cain, *Nature*, 1981, **290**, 161–163.

[119] H. Kamaya, N. Matubayasi, I. Ueda, *J. Phys. Chem.*, 1984, **88**, 797–800.

[120] D. W. R. Gruen, D. A. Haydon, *Biophys. J.*, 1981, **33**, 167 – 187.

[121] P. Shchelokovskyy, S. Tristram-Nagle, R. Dimova, *New J. Phys.*, 2011, **13**, 25004.

[122] J. H. Dymond, H. A. O/ye, *J. Phys. Chem. Ref. Data*, 1994, **23**, 41–53.

[123] W. den Otter, S. Shkulipa, *Biophys. J.*, 2007, **93**, 423 – 433.

[124] D. Demus, J. Goodby, G. W. Gray, H. W. Spiess, *Handbook of Liquid Crystals: Fundamentals*, WILEY-VCH, 2008.

[125] G. R. Luckhurst, G. W. Gray, *The Molecular physics of liquid crystals*, Academic Press, 1979.

[126] K. Saito, T. Miyazawa, A. Fujiwara, M. Hishida, H. Saitoh, M. Massalska-Arodź, Y. Yamamura, *J. Chem. Phys.*, 2013, **139**, 114902.

[127] T. Adachi, Y. Yamamura, M. Hishida, M. Ueda, S. Ito, K. Saito, *Liq. Cryst.*, 2012, **39**, 1340–1344.

[128] T. Adachi, H. Saitoh, Y. Yamamura, M. Hishida, M. Ueda, S. Ito, K. Saito, *Bull. Chem. Soc. Japan*, 2013, **86**, 1022–1027.

[129] T. Miyazawa, Y. Yamamura, M. Hishida, S. Nagatomo, M. Massalska-Arodź, K. Saito, *J. Phys. Chem. B*, 2013, **117**, 8293–8299.

[130] K. Aburai, T. Ogura, R. Hyodo, H. Sakai, M. Abe, O. Glatter, *J. Oleo Sci.*, 2013, **62**, 913–918.

[131] R. Janarthanan, J. L. Horan, B. R. Caire, Z. C. Ziegler, Y. Yang, X. Zuo, M. W. Liberatore, M. R. Hibbs, A. M. Herring, *J. Polym. Sci. B Polym. Phys.*, 2013, **51**, 1743–1750.

[132] G. Pabst, M. Rappolt, H. Amenitsch, P. Laggner, *Phys. Rev. E*, 2000, **62**, 4000–4009.

[133] J. F. Nagle, S. Tristram-Nagle, *Biochim. Biophys. Acta*, 2000, **1469**, 159–195.

[134] E. Kim, N. Lockwood, M. Chopra, O. Guzmán, N. Abbott, J. de Pablo, *Biophys. J.*, 2005, **89**, 3141–58.

[135] T. J. McIntosh, R. V. McDaniel, S. A. Simon, *Biochim. Biophys. Acta*, 1983, **731**, 109 – 114.

[136] R. Boese, H.-C. Weiss, D. Bläser, *Angew. Chem. Int. Ed.*, 1999, **38**, 988–992.

[137] J. Czub, U. Gubernat, B. Gestblom, R. Dabrowski, S. Urban, *Z. Naturforsch. A*, 2004, **59**, 316–324.

[138] G. Oweimreen, M. Morsy, *Thermochim. Acta*, 2000, **346**, 37 – 47.

[139] S. Marčelja, *J. Chem. Phys.*, 1974, **60**, 3599–3604.

List of publications

- Chapter 3.

  H. Usuda, M. Hishida, Y. Yamamura, K. Saito, "Common Effects of Incorporated *n*-Alkane Derivatives on Molecular Packing and Phase Behavior of DPPC Bilayers", *Chem. Lett.* **2018**, *47*, 1512–1514.

  H. Usuda, M. Hishida, E. G. Kelly, Y. Yamamura, M. Nagao, K. Saito, 'Interleaflet Coupling of *n*-Alkane Incorporated Bilayers'", *Chem. Phys. Phys. Chem.* accepted.

- Chapter 4.

  H. Usuda, M. Hishida, Y. Yamamura, K. Saito, "Contrasting Effects of a Rigid Core and an Alkyl Chain in *n*CB on the Phase Behavior of Lipid Bilayers.", *Langmuir* **2016**, *32*, 5966–5972.

- Related paper

  M. Hishida, R. Yanagisawa, **H. Usuda**, Y. Yamamura, K. Saito, "Rigidification of a Lipid Bilayer by an Incorporated *n*-Alkane.", *J. Chem. Phys.* **2016**, *144*, 041103.

Acknowledgment